Andreev tunneling and quasiparticle excitations in mesoscopic normal metal - superconductor structures

Andreev tunneling and quasiparticle excitations in mesoscopic normal metal - superconductor structures

Ville F. Maisi

Aalto University
School of Science
Olli V. Lounasmaa Laboratory
PICO group

Centre for Metrology and
Accreditation (MIKES)
Electricity group

Supervising professor
Jukka Pekola

Thesis advisor
Antti Manninen

Preliminary examiners
Alexey Ustinov, Karlsruhe Institute of Technology, Germany
Alexander Melnikov, Russian Academy of Sciences, Russia

Opponent
Hugues Pothier, CEA Saclay, France

Abstract

Author
Ville F. Maisi

Name of the doctoral dissertation
Andreev tunneling and quasiparticle excitations in mesoscopic normal metal - superconductor structures

Publisher Centre for Metrology and Accreditation

Unit Olli V. Lounasmaa Laboratory, School of Science

Series J1/2014, Centre for Metrology and Accreditation

Field of research Low Temperature Physics

Manuscript submitted 15.1.2014	**Date of the defense** 30.4.2014
Permission to publish granted 11.3.2014	**Language** English

Article dissertation (summary + original articles)

Abstract

Mesoscopic physics deals with systems whose size is between everyday macroscopic scale and the microscopic scale of individual atoms. With mesoscopic structures the flow of single electrons can be controlled. This thesis focuses on the control of single electrons with normal metal - superconductor structures. The emphasis is put on understanding the limitations of the control in the so-called SINIS turnstile, which is a device transporting one electron at a time. By repeating the drive with frequency f, the resulting electrical current in ideal operation $I = ef$ could be utilized as the new definition in the SI unit system. Here e is the elementary charge.

In the first part of the thesis, we review the physics of tunnel-coupled normal metals and superconductors and present the operation principle of the SINIS turnstile. We then show parallel operation of ten such devices. This allows one to reach larger currents required for high accuracy measurements. In addition we show that the experimental setup needs to be carefully designed in order to avoid spurious effects due to environmentally assisted tunneling.

The second part of the thesis focuses on Andreev tunneling. In this process two electrons tunnel at once in form of a Cooper pair. Andreev tunneling leads to transfer errors, when the tunneling of a single electron is preferred. We discuss the experimental detection techniques of Andreev tunneling based on direct current measurements as well as on electron counting. Furthermore, we show experimentally that by having large enough energy cost for charging the structures, achieved by decreasing the size of the system, Andreev tunneling is suppressed and the accuracy of the turnstile improves. The electron counting techniques allows us to study nontrivial statistics of Andreev tunneling.

In the last part of the thesis, excitations in a superconductor are considered. At low temperatures, the number of excitations of a superconductor should diminish exponentially. However, excess excitations in form of broken Cooper pairs are typically present limiting the performance of superconducting circuits. We discuss ways of probing the excitations in the normal metal - superconductor based structures. We investigate the diffusion of the quasiparticles and their relaxation to normal metallic traps or due to recombination into Cooper pairs via electron-phonon interaction.

Keywords Single-electron transport, Quantum metrology, Andreev tunneling, Quasiparticle excitations in superconductor

Tiivistelmä

Mesoskooppinen fysiikka käsittelee rakenteita, joiden koko on jokapäiväisen makroskooppisen mittakaavan ja mikroskooppisen atomimittakaavan välillä. Mesoskooppisissa rakenteissa pystytään siirtämään elektroneja hallitusti yksitellen. Tämä väitöskirja keskittyy yksittäisten elektronien siirtoon normaalimetalleissa ja suprajohteissa. Eräs työn tärkeimmistä painopisteistä on ymmärtää niinkutsutun SINIS-kääntöportin toiminnan rajoitukset. SINIS-kääntöportti on laite, jolla pystytään siirtämään elektroneja yksitellen suprajohteelta toiselle. Toistotaajuudella f saadaan näin aikaiseksi sähkövirta I = ef, jossa e on alkeisvaraus.

Väitöskirjan ensimmäisessä osassa käsitellään elektronien tunneloitumista normaalimetallin ja suprajohteen välillä ja esitetään SINIS-kääntöportin toimintaperiaate. Käyttämällä kymmentä kääntöporttia rinnakkain saavutetaan riittävä virtataso tarkkuusmittauksiin. Lisäksi näytämme, että näyte pitää suojata hyvin, jotta korkeammista lämpötiloista tuleva säteily ei heikennä laitteen toimintaa.

Työn toisessa osassa keskitymme niinkutsuttuun Andreev-tunnelointiin. Kyseisessä prosessissa kaksi elektronia tunneloituu samanaikaisesti muodostaen Cooperin parin suprajohteelle. Andreev-prosessi aiheuttaa virheitä laitteisiin, joiden toiminta perustuu yhden elektronin tunnelointiin. Käsittelemme kokeellisia tekniikoita, joilla Andreev-tunnelointi havaitaan ja lisäksi osoitamme, että tämä prosessi voidaan välttää SINIS-kääntöportissa. Lisäksi tutkimme elektronilaskentaa käyttäen Andreev-tunneloinnin statistisia ominaisuuksia.

Väitöskirjan viimeisessä osassa käsitellään suprajohteiden eksitaatioita. Matalassa lämpötilassa eksitaatioiden pitäisi hävitä eksponentiaalisesti. Tyypillisesti näin ei kuitenkaan käy, vaan ylimääräisiä eksitaatioita jää suprajohteeseen hajonneiden Cooperin parien muodossa. Nämä eksitaatiot heikentävät suprajohteiden ominaisuuksia. Esitämme tässä osassa tapoja, joilla eksitaatioita voidaan havaita käyttäen normaalimetallin ja suprajohteen välisiä tunneliliitoksia. Tutkimme eksitaatioden diffuusiota ja relaksaatiota näillä menetelmillä. Tutkituissa rakenteissa relaksaatio aiheutuu tunneloitumisesta normaalimetallisiin osiin tai rekombinoitumisesta Cooperin pareiksi.

Preface

This thesis was initiated by a common interest shared by the Low Temperature Laboratory (OVVL) at Aalto University and the Centre for Metrology and Accreditation (MIKES). Both of the institutes were curious to know about the accuracy obtainable with the so-called SINIS turnstile. At the time I begun the thesis, the SINIS turnstile was a promising new device for generating a well known electrical current. MIKES was interested to know whether the SINIS turnstile could be utilized to redefine the SI unit of electrical current whereas Low Temperature Laboratory was more interested in understanding the physics of the device. For achieving both of these goals, the accuracy of the device needed to be increased by several orders of magnitude and this became the goal for my thesis. First of all, I want to express my gratitude to both of the institutes for allowing me to work jointly in them. In addition to administrative staff, I especially thank my instructor Prof. Jukka Pekola from OVVL and Dr. Antti Manninen from MIKES for taking care of the required arrangements.

The role of my thesis instructor Prof. Jukka Pekola was not at all limited to the administrative duties. In fact, he deserves the greatest acknowledgment of this thesis. Without his inspiring ideas, effective solutions to problems, professional instruction ranging from sample fabrication and English grammar to detailed theoretical calculations, and devotion and enthusiasm towards research, this thesis would not exist in the form you have it now. A good example about depth at which Jukka is involved to the everyday work in the laboratory, is the case when we repaired together one of the dilution refrigerators during the days between Christmas and new year. Having such a talented instructor on a day-to-day basis is a tremendous privilege for a young student striving to become a physicist. Thank you for that!

In addition to Jukka, Dr. Matthias Meschke has contributed remarkably

for the thesis. He is the one who does the silent but very important work for keeping all equipment running and in good condition. I also thank for his patience and helpfulness for teaching me hands-on how to build, operate and repair various gadgets and master the device fabrication. Working with the talented group members of PICO group of OVVL and electricity group of MIKES has been also a great asset. Especially working more closely with Olli-Pentti Saira, Antti Kemppinen, Sergey Kafanov, Helena Knowles, Jonne Koski, Thomas Aref, Emma Mykkänen and Elsa Mannila has been very fruitful. Jukka also initiated many valuable contacts to other reseach groups. Collaborating with Yuri Pashkin, Dmitri Averin, Frank Hekking, Mikko Möttönen, Andreas Heimes, Dimitri Golubev, Christian Flindt, Dania Kambly, Sergey Lotkhov, Martin Gustafsson, Per Delsing and Angelo Di Marco has been essential for the thesis and has given new ways to approach the same problems. I want to thank especially Prof. Frank Hekking for teaching the calculation techniques used in this thesis.

The experimental results of the thesis have benefited from the expertise of the OVVL mechanical workshop staff. They have been able to materialize many desing in short notice, for example the shielded sample holders used in Publication VI as well as a missing collar for helium transfer dewar which I by accident shipped away. I also acknowledge the access to clean room facilities of Micronova and financial support of The National Doctoral Programme in Nanoscience (NGS-NANO).

Last but not least, I want to thank my gorgeous family and especially my beloved wife Hanna who has taken care of many things during all these years. She has been there for me and the whole family whenever needed. She has also (nearly) always remembered to remind me about important things.

Helsinki, March 15, 2014,

Ville Maisi

Contents

List of Publications

This thesis consists of an overview and of the following publications which are referred to in the text by their Roman numerals.

I V. F. Maisi, Yu. A. Pashkin, S. Kafanov, J. S. Tsai and J. P. Pekola. Parallel pumping of electrons. *New J. Phys.* **11**, 113057 (2009).

II J. P. Pekola, V. F. Maisi, S. Kafanov, N. Chekurov, A. Kemppinen, Yu. A. Pashkin, O.-P. Saira, M. Möttönen and J. S. Tsai. Environment-Assisted Tunneling as an Origin of the Dynes Density of States. *Phys. Rev. Lett.* **105**, 026803 (2010).

III O.-P. Saira, M. Möttönen, V. F. Maisi and J. P. Pekola. Environmentally activated tunneling events in a hybrid single-electron box. *Phys. Rev. B* **82**, 155443 (2010).

IV V. F. Maisi, O.-P. Saira, Yu. A. Pashkin, J. S. Tsai, D. V. Averin and J. P. Pekola. Real-Time Observation of Discrete Andreev Tunneling Events. *Phys. Rev. Lett.* **106**, 217003 (2011).

V T. Aref, V. F. Maisi, M. Gustafsson, P. Delsing and J. P. Pekola. Andreev tunneling in charge pumping with SINIS turnstiles. *Europhys. Lett.* **96**, 37008 (2011).

VI O.-P. Saira, A. Kemppinen, V. F. Maisi and J. P. Pekola. Vanishing quasiparticle density in a hybrid Al/Cu/Al single-electron transistor. *Phys. Rev. B* **85**, 012504 (2012).

VII H. S. Knowles, V. F. Maisi and J. P. Pekola. Probing quasiparticle excitations in a hybrid single electron transistor. *Appl. Phys. Lett.* **100**, 262601 (2012).

VIII J. P. Pekola, O.-P. Saira, V. F. Maisi, A. Kemppinen, M. Möttönen, Yu. A. Pashkin and D. V. Averin. Single-electron current sources: towards a refined definition of ampere. *Rev. Mod. Phys.* **85**, 1421 (2013).

IX V. F. Maisi, S. V. Lotkhov, A. Kemppinen, A. Heimes, J. T. Muhonen and J. P. Pekola. Excitation of Single Quasiparticles in a Small Superconducting Al Island Connected to Normal-Metal Leads by Tunnel Junctions. *Phys. Rev. Lett.* **111**, 147001 (2013).

X A. Di Marco, V. F. Maisi, J. P. Pekola and F. W. J. Hekking. Leakage current of a superconductor–normal metal tunnel junction connected to a high-temperature environment. *Phys. Rev. B* **88**, 174507 (2013).

XI V. F. Maisi, D. Kambly, C. Flindt and J. P. Pekola. Full counting statistics of Andreev tunneling. *Phys. Rev. Lett.* **112**, 036801 (2014).

Author's Contribution

Publication I: "Parallel pumping of electrons"

The author took part in designing the devices, performed the measurements and wrote the manuscript.

Publication II: "Environment-Assisted Tunneling as an Origin of the Dynes Density of States"

The author fabricated the single NIS junctions, had significant role in the measurements and did most of the numerical analysis of the results and prepared part of the manuscript.

Publication III: "Environmentally activated tunneling events in a hybrid single-electron box"

The author assisted in device fabrication and measurements and took part in manuscript preparation.

Publication IV: "Real-Time Observation of Discrete Andreev Tunneling Events"

The author had main responsibility in sample design, measurements, and result analysis and wrote majority of the manuscript.

Publication V: "Andreev tunneling in charge pumping with SINIS turnstiles"

The author advised in the measurements, did the master equation based analysis and took part in manuscript preparation.

Publication VI: "Vanishing quasiparticle density in a hybrid Al/Cu/Al single-electron transistor"

The author fabricated the reference sample, designed and built shielded sample holders used in cryostat PT and took part in analysis and manuscript preparation.

Publication VII: "Probing quasiparticle excitations in a hybrid single electron transistor"

The author had main responsibility in sample design, did most of the calculations and took part in manuscript preparation.

Publication VIII: "Single-electron current sources: towards a refined definition of ampere"

The author wrote sections III.B.2-3 and G.6 and took part in preparation of the other sections.

Publication IX: "Excitation of Single Quasiparticles in a Small Superconducting Al Island Connected to Normal-Metal Leads by Tunnel Junctions"

The author fabricated some of the samples, performed most of the experiments, did major part of the calculations and wrote most of the manuscript.

Publication X: "Leakage current of a superconductor–normal metal tunnel junction connected to a high-temperature environment"

The author took part in calculations and manuscript preparation.

Publication XI: "Full counting statistics of Andreev tunneling"

The author prepared the sample, did the measurements and took part in manuscript preparation.

1. Introduction

Using low temperatures freezes out unwanted degrees of freedom. This allows one to study fundamental properties of matter in high detail and make predictions on what happens at higher temperatures where the excitations are present. In addition, fully new phenomena take place at low temperatures. For example the discreteness of electron charge results in single-electron effects where the electrons are transported sequentially. On the other hand, superconductivity with dissipation-free electrical current and other peculiar properties arises at low temperatures and provides opportunities for a vast range of possible applications.

This thesis deals with small metallic systems at low temperatures where single-electron effects and superconductivity play an important role. These essential concepts in view of the present thesis are reviewed in Chapter 2. We focus on structures where superconducting and normal metallic structures are coupled weakly by an insulating tunnel barrier. The electrons may pass through such a barrier by tunneling. The weak coupling favors that the electrons tunnel one by one. On the other hand, in superconductors the electrons are paired as Cooper pairs. Breaking such a pair and having a single-electron process requires minimally an energy Δ per particle, known as the energy gap [1]. Because of the pair breaking energy cost, the single-electron tunneling process is suppressed if energies exceeding Δ are not available. In this case the transport must involve simultaneously two electrons in form of a Cooper pair. A process where a complete Cooper pair moves from a superconductor to a normal metal or vice versa is known as Andreev reflection. It was first used to describe thermal conductance between two metals [2], one superconducting the other one normal. In the case of a tunnel barrier, the process is known as Andreev tunneling, which is the topic of Chapter 5. We will learn that at low bias, Andreev tunneling is the dominant process [3–9]. However, if

small metallic structures are considered, the charging of a metallic island by an additional electron is associated with an energy cost characterized by charging energy $E_c = e^2/(2C_\Sigma)$, where e is the elementary charge and C_Σ the sum of all capacitances contacted to the island. We observe that if E_c is made larger than the pair breaking energy Δ, Andreev tunneling becomes suppressed. This is observed in this thesis, e.g., in direct current measurements. In addition, Andreev tunneling is studied by detecting discrete tunneling events in real-time. The observation of the individual events allows one to study the statistics of them. In Sect. 5.5 we find out that the interplay of single-electron and two-electron tunneling leads to non-trivial super-Poissonian statistics. The findings of this chapter are important for understanding the limitations of hybrid normal metal - superconductor systems, especially for single-electron applications.

The peculiar properties of the superconductors are based on the fact that a single electron excitation requires an energy exceeding Δ. If this energy is not available, all the electrons are paired, there are no excitations, and hence dissipation is also absent. However, when the number of excitations becomes low, their relaxation also becomes weak and typically excess excitations remain. These residual quasiparticles influence adversely the performance of superconducting circuits [10–19], as discussed in Chapter 6. We first discuss how the excitations can be experimentally probed with tunnel junctions between a normal metal and a superconductor. We observe that the number of them is suppressed when the structures are well protected from the high temperature environment, and when efficient relaxation is provided.

In Sect. 6.2 we consider the electrical heat conduction and relaxation in superconducting leads. Heat transport along a superconductor is governed by diffusion of the excitations. With tunnel junction based structures we show that the injection and probing of quasiparticles can be done simultaneously. In this way, we see that the diffusion equation approach is adequate for describing the relaxation in superconducting lines with relaxation being dominated by diffusive transport of excitations to normal metallic parts and further relaxation there. In this case, the inherent quasiparticle relaxation of the superconductor by recombination is not taken into account since it is weak as compared to relaxation in normal metallic traps. In Sect. 6.4 we consider a small superconducting island where the electrons cannot diffuse to normal metallic parts. Then the electron-phonon interaction leading to energy loss and recombination

into Cooper pairs, which is the inherent relaxation mechanism, becomes important. By injecting and detecting the excitations, as in Sect. 6.2, we are now able to probe the electron-phonon interaction. The probing is done down to a level where there is only one broken Cooper pair present, hence allowing to determine its recombination rate. In the absence of injection, there are essentially no excitations present.

One of the main motivations for studying the physical phenomena of this thesis has been the possibility to obtain quantized electrical current in such structures. Here quantization does not refer to quantum mechanics. The quantization is based in this case on the fact that all electrons carry the same elementary electronic charge e, which was first observed in micrometer-sized oil droplets [20, 21]. The quantized current $I = nef$ results when n electrons are transported in a cycle which is repeated at a frequency f [22–30]. In Fig. 1.1 the principles of the very first devices achieving the current quantization experimentally as well as the most prominent candidates for reaching high accuracy and large enough output current are shown. Figure 1.1 (a) represents a normal metallic turnstile where only one radio frequency (RF) signal is needed to obtain the quantization [31]. A voltage bias is applied to the device to set the preferred direction for tunneling. The offset charge of the central island is driven periodically to plunge an electron to the middle island and then to push it out to the other lead and hence one electron is transported per cycle through the device. The two islands next to the middle one are required to block the static current flow when degeneracy point of the middle island is passed.

In panel (b) a device similar to the one in panel (a) but one island less is shown. By using two RF drives, one for each island, the electrons can be pumped without an external bias voltage, or even against a small bias [25]. First the left gate offset charge is changed to pull an electron into the left island from the left lead. Then the gate offset is moved back and simultaneously the right gate offset charge is changed to move an electron from the left island to the right one. Finally, the offset charge of the right island is brought back to the starting value and an electron tunnels out from it to the right lead and a single electron is transported through the device. The accuracy of these two normal metallic devices is limited by co-tunneling of electrons. The co-tunneling can however be reduced by adding more islands in series [28]. The highest accuracy reached so far with single-electron sources was obtained with the approach shown
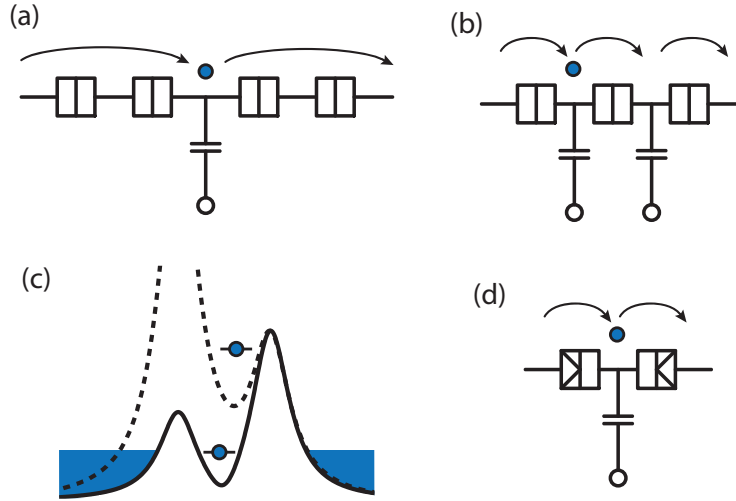
Figure 1.1. Various single-electron sources. (a) The normal metallic turnstile. Three normal metallic islands are connected with tunnel junctions. A gate drive is applied to the central island to obtain quantized current. (b) Normal metallic single-electron pump. The gate offset charge of two islands are driven periodically. A quantized current is obtained without applying a bias voltage since electrons are moved from one island to another by changing the electron numbers of the two island controllably. (c) Potential landscape of a semiconductor pump. The height of the left barrier is changed cyclically to form a quantum dot, trap one electron to it from the left reservoir and plunge it to the right reservoir. The solid and dashed lines show schematically the potential for two different barrier gate values. (d) The SINIS turnstile. The hysteresis needed for the turnstile operation is achieved with superconducting leads instead of the two extra islands as in panel (a). The superconducting electrodes provide in addition protection against co-tunneling.

in panel (b) with seven junctions in series with an error per pumped electron of 15 parts in 10^9 [32]. However, the complexity of the device operation was significantly increased and the overall magnitude of output current reduced.

Almost at the same time as the operation principle of the metallic devices was demonstrated, semiconductor electron pumps were also developed [33]. Their operation is based on not only tuning the number of electrons on a conducting island with a gate offset charge but on the possibility to open and close tunnel barriers with gate electrodes. In Fig. 1.1 (c) we show a potential energy along a device which has recently been used to obtain the highest quantization accuracy with an error smaller than 1.2 parts in 10^6 in a semiconductor devices [30]. It is operated by raising and lowering a tunnel barrier. Together with another static tunnel barrier, a quantum dot is formed dynamically, a single-electron captured to it and plunged over the static barrier. Hence a single-electron is transported in each cycle and quantized current results.

In this thesis, we focus on the so-called SINIS turnstile [34], which is

presented schematically in Fig.1.1 (d). It is operated like the normal metallic turnstile of panel (a). The difference is that the turnstile operation is achieved by using superconducting leads instead of the two extra islands. The superconductors suppress effectively the co-tunneling errors [34] and hence the SINIS turnstile is considered as a potential candidate to reach high accuracy. Its operation principle is simple enough to operate many of them in parallel as described in Sect. 3.3. The Andreev tunneling, the excitations in superconductors as well as photon assisted tunneling discussed in Sect. 4 all contribute to the errors of the current quantization of the SINIS turnstile. These error sources are addressed in this thesis. By optimizing the operation, the best quantization accuracy so far with such a device was obtained with a relative uncertainty as low as 10^{-4}. However, we believe that after the error sources identified in this thesis have been suppressed by further optimization, the relative accuracy of the device can be improved to the level of 10^{-7} or below.

In addition to the single-electron sources presented in this chaper, there is a vast range of many other approaches studied as well. A more comprehensive discussion of the alternative possibilities is presented in Publication VIII.

2. Electron tunneling between a superconductor and a normal metal

Electrons in a superconductor form Cooper pairs. The pairing is due to an attractive interaction which is incorporated into the microscopic description of free electrons in a metal to formulate the so-called Bardeen-Cooper-Schieffer (BCS) theory [35]. This theory is typically the starting point for considering superconductors. Here we first outline the basic results of the BCS theory in Sect. 2.1 relevant for this thesis. Then in Sect. 2.2 we consider single-electron processes between a normal metal and a superconductor separated by a thin insulating barrier. We see that the energy exceeding Δ, for tunneling to take place, can be provided either thermally or by a voltage bias.

2.1 Superconductivity

The electrons in a superconductor are described in BCS theory by a pairing Hamiltonian, see, eg., Ref. [1],

$$\hat{H}_S = \sum_{k\sigma} \varepsilon_k c_{k\sigma}^\dagger c_{k\sigma} + \sum_{kl} V_{kl} c_{k\uparrow}^\dagger c_{-k\downarrow}^\dagger c_{-l\downarrow} c_{l\uparrow}. \tag{2.1}$$

Here the first part describes electron states with energy ε_k, momentum k and spin σ, and $c_{k\sigma}^\dagger$ is the corresponding creation operator. The second part is the coupling leading to superconductivity. It pairs electrons with momenta and spin being $k \uparrow$ and $-k \downarrow$. Next we assume $c_{-k\downarrow} c_{k\uparrow}$ to have an expectation value $b_k = \langle c_{-k\downarrow} c_{k\uparrow} \rangle$, and that the fluctuations $(c_{-k\downarrow} c_{k\uparrow} - b_k)$ away from this value are small. By keeping only the leading order terms, we obtain from Eq. (2.1)

$$\hat{H}_S = \sum_{k\sigma} \varepsilon_k c_{k\sigma}^\dagger c_{k\sigma} - \sum_k \left(\Delta_k c_{k\uparrow}^\dagger c_{-k\downarrow}^\dagger + \Delta_k^* c_{-k\downarrow} c_{k\uparrow} - \Delta_k b_k^* \right), \tag{2.2}$$

where $\Delta_k = -\sum_l V_{kl} b_l$. Equation (2.2) can be diagonalized with the so-called Bogoliubov transformation [36, 37] by introducing new fermionic

creation operators $\gamma_{k\sigma}^\dagger$ relating to the electron operators by

$$\begin{cases} c_{k\uparrow}^\dagger &= v_k^* \gamma_{-k\downarrow} &+ u_k \gamma_{k\uparrow}^\dagger \\ c_{-k\downarrow}^\dagger &= -v_k^* \gamma_{k\uparrow} &+ u_k \gamma_{-k\downarrow}^\dagger. \end{cases} \tag{2.3}$$

The commutation relations yield $|u_k|^2 + |v_k|^2 = 1$. By choosing u_k and v_k in such a way that $2\varepsilon_k u_k v_k + \Delta_k^* v_k^2 - \Delta_k u_k^2 = 0$, the off-diagonal elements of $\hat{H}_S$ vanish when expressed in terms of $\gamma_{k\sigma}$. The Hamiltonian is then

$$\hat{H}_S = \sum_{k\sigma} E_k \gamma_{k\sigma}^\dagger \gamma_{k\sigma}, \tag{2.4}$$

where we have energy

$$E_k = \sqrt{\varepsilon_k^2 + |\Delta_k|^2}, \tag{2.5}$$

for the excitations with creation operator $\gamma_{k\sigma}^\dagger$. The constant condensation energy is neglected because it does not contribute to the calculations presented in this thesis. Only the energy differences are relevant. The coefficients of the transformation in the diagonalized form are given by

$$|v_k|^2 = 1 - |u_k|^2 = \frac{1}{2}\left(1 - \frac{\varepsilon_k}{E_k}\right). \tag{2.6}$$

Equation (2.3) can be written as $c_{k\sigma}^\dagger = v_{k\sigma}^* \gamma_{-(k\sigma)} + u_{k\sigma}\gamma_{k\sigma}^\dagger$, where $v_{k\uparrow} \equiv v_k$, $v_{k\downarrow} \equiv -v_{-k}$, $u_{k\uparrow} \equiv u_k$ and $u_{k\downarrow} \equiv u_{-k}$. This notation is convenient for the forthcoming calculations. The Hamiltonian of Eq. (2.4) allows to obtain the temperature depencence of Δ_k as well as the critical temperature T_C, where the material becomes superconducting [1]. In the following we assume that $\Delta_k = \Delta$, i.e., that the energy gap is independent of the wavevector k. This assumption is well valid and justified for our considerations since only states with $|k|$ close to the Fermi wavevector k_F are relevant and the materials we consider are isotropic, i.e. there are no strong directional dependencies. Also, we take Δ to be temperature independent since we consider superconductor temperatures $T_S < T_C/3$, where the temperature depencency of Δ is exponentially weak [1].

Having Eq. (2.5), we can readily obtain the density of states (DoS) of a superconductor which is in a very essential role for understanding the properties of a metal in superconducting state. The DoS yields the number per unit volume and energy of electronic states at a given energy E, which we measure with respect to the Fermi level. Equation (2.5) links the energy of an unpaired electron ε_k to the excitation energy E_k with the energy gap Δ_k. Since we assume a wavevector independent energy gap Δ, the wavevector k is irrelevant and we may drop it off and obtain $E = \sqrt{\varepsilon^2 + |\Delta|^2}$. Throughout this thesis, we consider small energies, up
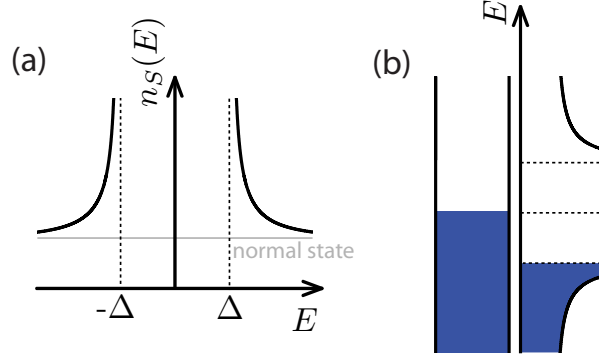
Figure 2.1. Density of states of a superconductor. (a), The density of states (DoS) $n_S(E)$ for quasiparticle excitations with energy E. The curve is normalized with respect to the constant normal state DoS shown as a grey line. (b), DoS with the occupations in the low temperature limit. Left side shows the normal state case and the right hand side shows the superconducting case. For normal metal, DoS is constant and levels below Fermi level $E < 0$ are all filled shown by the blue area and levels above, $E > 0$ are all vacant. Similarly, for superconductor, all states at $E < -\Delta$ are all filled and all with $E > \Delta$ are vacant. The region $-\Delta < E < \Delta$ is known as the energy gap as there are no electronic states at all.

to a few meV, around the Fermi energy, which, in turn, is on the eV range. Therefore we assume that the unpaired energies ε have a constant density of states around the Fermi level. We obtain the superconducting DoS, normalized with respect to the normal state value, as

$$n_S(E) = \frac{d\epsilon}{dE} = \frac{|E|}{\sqrt{E^2 - \Delta^2}}, \tag{2.7}$$

for $|E| > \Delta$ and $n_S(E) = 0$ for $|E| < \Delta$. This result is plotted in Fig. 2.1 (a). We observe that an excitation, see Eq. (2.5), carries an energy $|E| > \Delta$, reflecting the fact that the minimum energy cost for an unpaired electron is Δ. In the DoS this is seen as the energy gap: there are no states available for $|E| < \Delta$. Note that in Fig. 2.1 (a) we have reflected the DoS for negative energies such that it reduces correctly to the normal state result when $\Delta \to 0$. We find out in Sect. 2.2 that the reflection to negative energies is illustrative for considering the electron tunneling. This approach is known as the semiconductor model [1] since the energy gap of a superconductor reminds greatly the bandgap of a semiconductor and the coherent effects of a superconductor are not relevant in this picture. In Fig. 2.1 (b) we present the occupations of the energy levels for a superconductor and a normal metal in the zero temperature limit. The states with $E < 0$ are occupied by electrons and states with $E > 0$ are vacant.

2.2 Electron tunneling

A tunnel contact or a tunnel junction is a structure where two metals are not in a direct contact but they are separated by a thin insulating layer. The insulating layer can be vacuum or made of an electrically insulating material such as aluminum oxide, as in this thesis. In Fig. 2.2 (a) such a junction is presented. The junction is formed here between the overlapping region of a normal metallic (N) copper and superconducting (S) aluminum. Together with the insulating layer (I) they form an NIS junction which is the basic building block used in this thesis. In panel (b) the current I through the junction is measured against bias voltage V_b. Next we discuss the origin and characteristics of this current.

Classically, electrical current cannot flow from one of the metals to the other because electrons cannot cross the insulating barrier. However, with thin barriers, we must consider the situation quantum mechanically. Quantum mechanics predicts that the electronic states are not fully confined inside the conducting regions but they extend to the insulating material. This effect decays exponentially with respect to the distance from the conductor and hence is not relevant at large distances. At short distances, i.e. in the case of tunnel contacts, this gives rise to electron transport between neighboring metals. Next, we derive the tunneling rates for such contacts.

2.2.1 Hamiltonian and current operator

A normal metal and a superconductor contacted by a tunnel junction has a Hamiltonian

$$\hat{H} = \hat{H}_S + \hat{H}_N + \hat{H}_T + \hat{H}_B, \tag{2.8}$$

where $\hat{H}_S$ is the Hamiltonian of a superconductor given by Eq. (2.4). $\hat{H}_N$ is similarly the Hamiltonian for the normal metal with $V_{kl} = 0$. It reads

$$\hat{H}_N = \sum_{k\sigma}(\epsilon_k + e\delta\hat{V}(t))a_{k\sigma}^\dagger a_{k\sigma}, \tag{2.9}$$

where $a_{k\sigma}^\dagger$ is the creation operator of an electron with wavevector k and spin σ. We allow here for generality voltage fluctuations $\delta\hat{V}(t)$ to add or remove energy from the electrons. The fluctuations are caused by photons coupling to the system and they are described by

$$\hat{H}_B = \sum_\lambda \hbar\omega_\lambda b_\lambda^\dagger b_\lambda, \tag{2.10}$$
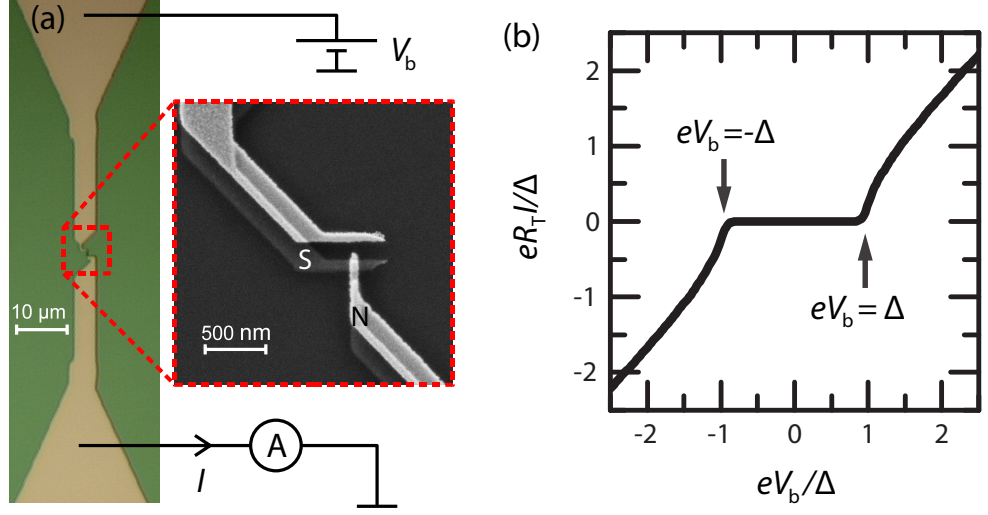
Figure 2.2. A typical NIS junction. (a), Optical microscope picture (left) and a scanning electron micrograph (right) of a typical NIS junction used in this thesis. In the optical microscope image, the topmost normal metallic copper film is visible. This can be seen in the scanning electron micrograph as the bright parts whereas the lower superconducting aluminum layer gives weaker contrast. The structures of this thesis are fabricated with so-called shadow evaporation technique [38] allowing single-electron device fabrication [39]. The junction is biased with a voltage bias V_b and current I through it is measured. The experimental current - voltage curve is presented in panel (b). The axes are normalized with respect to the tunnel resistance $R_T = 600$ kΩ and superconductor gap $\Delta = 200$ μeV.

with eigenenergies $\hbar\omega_\lambda$. Here $b_\lambda^\dagger$ and b_λ are the corresponding bosonic creation and annihilation operators. In this section we consider the case $\delta\hat{V}(t) = 0$, when $\hat{H}_B$ does not play a role, but we return to the photon environment in Sect. 4. The last part of Eq. (2.8) is the tunnel coupling of the two metals

$$\hat{H}_T = \sum_{kq\sigma} t_{kq} c_{q\sigma}^\dagger a_{k\sigma} + \text{h.c.}, \tag{2.11}$$

where h.c. stands for hermitian conjugate and we assumed spin independent and spin conserving coupling t_{kq}. In order to calculate the tunnel current $I = \langle \hat{I} \rangle$, or the corresponding tunneling rate $\Gamma = I/e$, we need the current operator $\hat{I}$. The most straightforward way to obtain it is to consider it in Heisenberg picture:

$$\hat{I}_H = e\frac{d}{dt}\hat{N}_{N,H} = \frac{ie}{\hbar}[\hat{H}, \hat{N}_{N,H}] \Rightarrow \hat{I} = \frac{ie}{\hbar}[\hat{H}, \hat{N}_N] = \frac{ie}{\hbar}[\hat{H}_T, \hat{N}_N], \tag{2.12}$$

where subindex H denotes Heisenberg picture and $\hat{N}_N = \sum_{k\sigma} a_{k\sigma}^\dagger a_{k\sigma}$, is the electron number operator of the normal metal. By using Eq. (2.11) we obtain

$$\hat{I} = \frac{ie}{\hbar} \sum_{kq\sigma} \left(t_{kq} c_{q\sigma}^\dagger a_{k\sigma} - \text{h.c.} \right). \tag{2.13}$$

2.2.2 Determination of tunneling rates

To calculate the average current I, we use density matrix formalism in the interaction picture. The average value of the current is expressed as $I =< \hat{I} >= \text{Tr}(\rho \hat{I})$, where Tr stands for a trace over the Fock space spanned by the electronic creation and annihilation operators and the density matrix ρ follows the Liouville equation of motion [40]

$$\frac{\partial}{\partial t}\rho = -\frac{i}{\hbar}[\hat{H}, \rho]. \tag{2.14}$$

Now we move to the interaction picture. We make an unitary transformation $\hat{A}_I = S\hat{A}S^\dagger$ for operator A, where the transformation S satisfies

$$\frac{\partial}{\partial t}\hat{S} = \frac{i}{\hbar}\hat{H}_0\hat{S}, \tag{2.15}$$

with $\hat{H}_0 = \hat{H}_N + \hat{H}_S + \hat{H}_B$, being the (time-dependent) reservoir part of the Hamiltonian of Eq. (2.8). By inspection we see that the transformation

$$\hat{S} = e^{\frac{i}{\hbar}\left(\hat{K}_0 t + \hat{\varphi}(t)\hat{N}_N\right)}. \tag{2.16}$$

satisfies the requirement of Eq. (2.15) with $\hat{K}_0 = \sum_{k\sigma} \epsilon_k^N a_{k\sigma}^\dagger a_{k\sigma} + \hat{H}_S + \hat{H}_B$ being the time indepenent part of $\hat{H}_0$ and $\hat{\varphi}(t) \equiv \frac{e}{\hbar}\int_{t_0}^t dt' \delta\hat{V}(t')$. With Equation (2.15) we obtain from Eq. (2.14)

$$\frac{\partial}{\partial t}\rho_I = -\frac{i}{\hbar}[\hat{H}_{T,I}, \rho_I]. \tag{2.17}$$

This can be solved formally by integration to yield

$$\rho(t) = \rho_0 - \frac{i}{\hbar}\int_{t_0}^t dt'[\hat{H}_T(t'), \rho(t')], \tag{2.18}$$

where $\rho_0 = Z^{-1}e^{\beta(-\hat{K}_0 + \mu_N \hat{N}_N)}$ is the intial solution taken to be at equilibrium (grand canonical) with respect to the leads at temperature T. Here Z is the partition function and $\beta = (k_B T)^{-1}$. The operators in Eq. (2.18) with explicit time dependence, are taken to be in the interaction picture $\hat{A}(t) \equiv \hat{A}_I$. We allow for a chemical potential shift between the normal metal and the superconductor. It is caused by the voltage bias across the junction and the charging effects discussed in Sect. 3. The chemical potential of the superconductor is set to zero without losing generality and hence the shift equals the chemical potential μ_N of the normal metal.

Now the current can be calculated as $I = \left\langle \hat{I} \right\rangle = \text{Tr}(\rho_I \hat{I}_I)$. Using Eq. (2.18) leads to a series expansion. The first non-zero term corresponds to single-electron tunneling and is given by

$$I = -\frac{i}{\hbar}\text{Tr}\left(\int_{-t_0}^t dt'[\hat{H}_T(t'), \rho_0]\hat{I}(t)\right) = \frac{i}{\hbar}\int_{-t_0}^t dt' \left\langle [\hat{H}_T(t'), \hat{I}(t)] \right\rangle_0, \tag{2.19}$$

where $\left\langle \hat{A} \right\rangle_0 = \text{Tr}(\rho_0 \hat{A})$ denotes a thermal average of $\hat{A}$. Equation (2.19) contains both processes, from superconductor to normal metal and vice versa. Later on, we need both these processes separately. Therefore we identify terms containing $a_{k\sigma}^\dagger a_{k\sigma}$ to correspond to tunneling from the normal metal to the superconductor since this term requires the initial state $k\sigma$ of the normal metal to be occupied in order for $a_{k\sigma}$ to yield a non-zero result. Collecting only such terms we obtain the tunneling rate from normal metal to the superconductor as

$$\Gamma_{N \to S} = \frac{I_{N \to S}}{e} = \frac{1}{\hbar^2} \int_{-t_0}^{t} dt' \sum_{kqq'\sigma} \Big\{$$
$$\left\langle t_{kq}^* a_{k\sigma}^\dagger(t) c_{q\sigma}(t)\, t_{kq'} c_{q'\sigma}^\dagger(t') a_{k\sigma}(t') \right\rangle_0$$
$$+ \left\langle t_{kq'}^* a_{k\sigma}^\dagger(t') c_{q'\sigma}(t')\, t_{kq} c_{q\sigma}^\dagger(t) a_{k\sigma}(t) \right\rangle_0 \Big\}. \tag{2.20}$$

Next we plug in Eq. (2.3) and obtain

$$\Gamma_{N \to S} = \frac{1}{\hbar^2} \int_{-t_0}^{t} dt' \sum_{kq\sigma} |t_{kq}|^2 \Big\{ |v_{q\sigma}|^2 \left\langle a_{k\sigma}^\dagger(t) \gamma_{-(q\sigma)}^\dagger(t)\, \gamma_{-(q\sigma)}(t') a_{k\sigma}(t') \right\rangle_0 +$$
$$|u_{q\sigma}|^2 \left\langle a_{k\sigma}^\dagger(t) \gamma_{q\sigma}(t)\, \gamma_{q\sigma}^\dagger(t') a_{k\sigma}(t') \right\rangle_0 +$$
$$|v_{q\sigma}|^2 \left\langle a_{k\sigma}^\dagger(t') \gamma_{-(q\sigma)}^\dagger(t')\, \gamma_{-(q\sigma)}(t) a_{k\sigma}(t) \right\rangle_0 +$$
$$|u_{q\sigma}|^2 \left\langle a_{k\sigma}^\dagger(t') \gamma_{q\sigma}(t')\, \gamma_{q\sigma}^\dagger(t) a_{k\sigma}(t) \right\rangle_0 \Big\}. \tag{2.21}$$

Next we assume $\delta \hat{V} = 0$ and use $a_{k\sigma}(t) = e^{-i\epsilon_k t/\hbar} a_{k\sigma}$ and $\gamma_{q\sigma}(t) = e^{-iE_q t/\hbar} \gamma_{q\sigma}$. Also we take the initial time $t_0 \to \infty$. By identifying Dirac delta functions $\delta(x) = \frac{1}{2\pi} \int_{-\infty}^{\infty} dt\, e^{ixt}$, we get

$$\Gamma_{N \to S} = \frac{2\pi}{\hbar} \sum_{kq\sigma} |t_{kq}|^2 \Big\{ |v_{q\sigma}|^2 \left\langle a_{k\sigma}^\dagger a_{k\sigma} \gamma_{-(q\sigma)}^\dagger \gamma_{-(q\sigma)} \right\rangle_0 \delta\left(\epsilon_k + E_q\right) +$$
$$|u_{q\sigma}|^2 \left\langle a_{k\sigma}^\dagger a_{k\sigma} \gamma_{q\sigma} \gamma_{q\sigma}^\dagger \right\rangle_0 \delta\left(\epsilon_k - E_q\right) \Big\}, \tag{2.22}$$

which is a Fermi golden rule result. Now we change the sums over k and q to integrals over energies ϵ_k and E_k which we relabeled as ϵ and E correspondingly. We also make a change of variables for the $v_{q\sigma}$ term and assume a constant normal state density of states. We obtain

$$\Gamma_{\text{N} \to \text{S}} = \frac{1}{e^2 R_T} \int_{-\infty}^{\infty} dE\, n_S(E) f_N(E - \mu_N)\left(1 - f_S(E)\right), \tag{2.23}$$

where R_T is the tunnel resistance of the junction since it determines the ohmic behaviour of the junction at high bias voltage. $n_S(E)$ is the DoS of a superconductor of Eq. (2.7) and f_N the Fermi occupation probability for the normal metal, and f_S for the superconductor. The remaining terms of Eq. (2.19) yield

$$\Gamma_{\text{S} \to \text{N}} = \frac{1}{e^2 R_T} \int_{-\infty}^{\infty} dE\, n_S(E)(1 - f_N(E - \mu_N)) f_S(E), \tag{2.24}$$
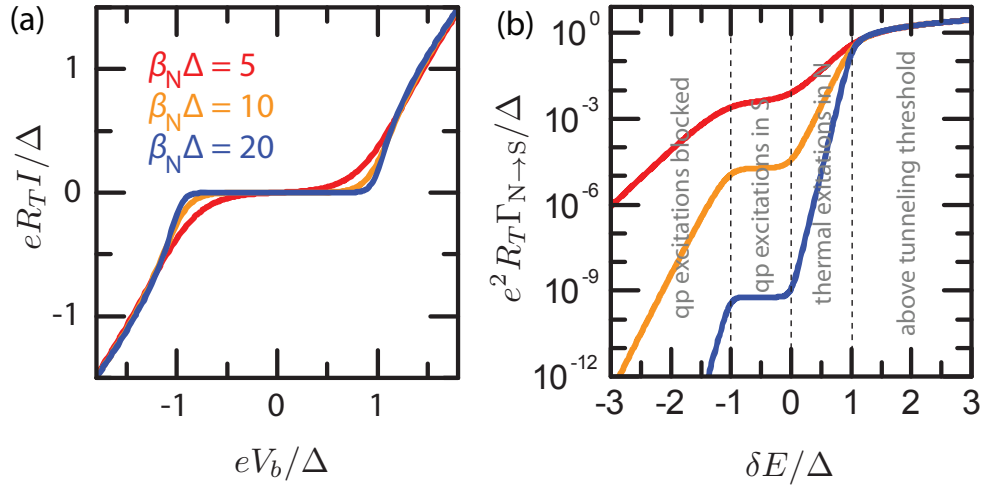
Figure 2.3. Calculated current and tunneling rates in an NIS junction. (a), Single-electron current I through a voltage biased NIS junction at various normal metal temperatures ($\beta_N = 1/k_B T_N$). (b), The corresponding tunneling rate $\Gamma_{N \to S}(\delta E)$ as a function of the energy gained δE in the tunneling process.

which is the tunneling rate from the superconductor to the normal metal. For a single NIS junction biased with voltage V_b the chemical potential shift is $\mu_N = eV_b$ and the total tunnel current is $I = e(\Gamma_{N \to S} - \Gamma_{S \to N})$, which we present for three different temperatures in Fig. 2.3 (a). The lowest temperature result catches well the features of the experimental curve of Fig. 2.2 (b). This tunneling current through an NIS junction was measured already in 1960 by I. Giaever [41] and it was one of the first experimental evidences of the existence of the superconductor energy gap Δ. The energy gap appears in the curves as suppressed current at $|eV_b| < \Delta$, since single-electron tunneling to a superconductor involves an unpaired electron with an energy cost of at least Δ. This feature is smeared as temperature increases, as shown in Fig. 2.3 (a). It demonstrates that in addition to the biasing, the energy can be provided also by the thermal bath.

The chemical potential shift μ_N appearing in Eq. (2.23) is the energy gained by the electron in the tunneling process from N to S. On the other hand, in Eq. (2.24) it is the energy cost for the opposing tunneling process. It is instructive to write both of the rates as a function of the energy gain δE which the electron obtains in a tunneling process. With this, we have

$$\Gamma_{N \to S}(\delta E) = \frac{1}{e^2 R_T} \int_{-\infty}^{\infty} dE \, n_S(E) f_N(E - \delta E) \left(1 - f_S(E)\right) \qquad (2.25)$$

and

$$\Gamma_{S \to N}(\delta E) = \frac{1}{e^2 R_T} \int_{-\infty}^{\infty} dE \, n_S(E)(1 - f_N(E + \delta E)) f_S(E). \qquad (2.26)$$
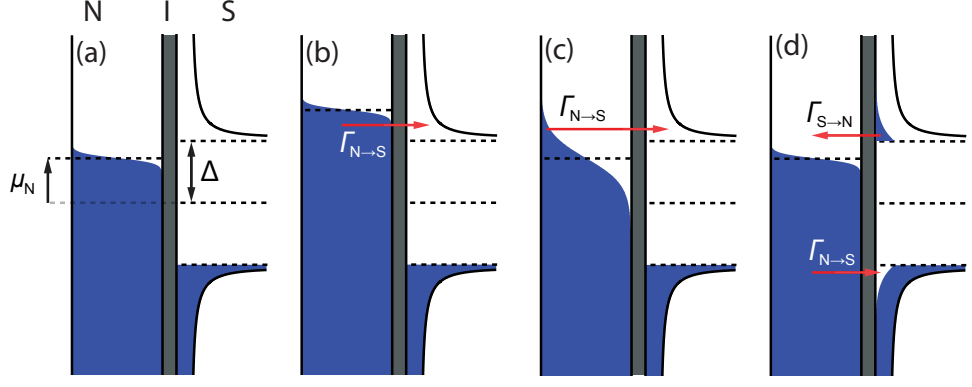
Figure 2.4. Schematic presentation of tunneling in an NIS junction. (a), Density of states of a normal metal (N) and a superconductor (S) which are shifted by the chemical potential μ_N. Blue color represents occupied states and white empty states which follow Fermi distribution. In panel (a), $\mu_N < \Delta$ and hence tunneling is suppressed. In panel (b), $\mu_N > \Delta$, and hence tunneling is taking place even at low temperatures with the rate $\Gamma_{N \to S}$. In panel (c) the temperature of the normal metal is elevated with respect to (a), which increases $\Gamma_{N \to S}$. Panel (d) shows tunneling rates for an elevated temperature of the superconductor.

It is now straightforward to show that $\Gamma_{S \to N}(\delta E) = \Gamma_{N \to S}(\delta E)$, i.e. that the tunneling rate depends on the energy gained by the electron but not whether it is coming from a normal metal or a superconductor. Hence we could drop subscripts $N \to S$ and $S \to N$ off. However, the discussion below is more apparent with the direction explicitly considered. We can for example distinguish the hole and particle like excitations on a superconductor explicitly. Therefore we still keep the subindices.

Now we are ready to consider the tunneling rates in an NIS junction in more detail with the density of states (DoS) diagrams shown in Fig. 2.4. See Sect. 2.1 for obtaining the diagrams. We assume the occupation of the states to follow Fermi distribution. In the diagram in panel (a) we take the temperature of the superconductor to be $T_S = 0$, i.e. all the states on the lower branch, $E < -\Delta$, are occupied and all at the higher one, $E > \Delta$, are vacant. The chemical potential μ_N shifts the two densities with respect to each other and electrons tunnel then horizontally. Tunneling is possible if an occupied state is found on one side and a vacant one on the other. The probability for having an occupied state in normal metal is f_N and in superconductor f_S, while the probability to have a vacant one on the other sides are $(1 - f_S)$ and $(1 - f_N)$ respectively. The tunneling rates of Eqs. (2.23) and (2.24) are then obtained by integrating over the product of the two DoSes and these probabilities.

In panel (a) the condition of having occupied state on one side and vacant on the other is not met for a considerable amount of states ($\mu_N < \Delta$) and

hence current is exponentially suppressed. In panel (b) we have $\mu_N > \Delta$. The occupied states of N are now so high that the tunneling to the upper empty branch of S becomes possible. This produces the onset of current at $eV_b = \Delta$, seen in Fig. 2.3 (a). In panel (c) of Fig. 2.4 we show elevated temperature of N in comparison to (a). High energy states are now thermally populated at N and hence current for $eV_b < \Delta$ is increased, causing the smearing. In panel (d) elevated temperature of S is shown. Some of the states at the lower branch are vacant and some at the higher branch are occupied. These quasiparticle excitations give rise to tunneling. From the higher branch of the superconductor, the electrons tunnel to the normal metal. On the other hand, the vacancies on the lower branch are filled by electrons tunneling from the normal metal leading to current in the opposite direction.

As a summary, we present Fig. 2.3 (b), where $\Gamma_{N \to S}$ is plotted as a function of the energy gain δE. We observe that there are four regimes of tunneling. For $\delta E > \Delta$, the zero temperature tunneling threshold is exceeded and the tunneling rate is insensitive to temperature. For $0 < \delta E < \Delta$, the current becomes exponentially suppressed at low temperatures as only electrons at high enough energy at the normal metal are able to tunnel. For $-\Delta < eV_b < 0$, the tunneling is dominated by quasiparticle excitations at the superconductor, see the rate $\Gamma_{N \to S}$ in panel (d) of Fig. 2.4. The quasiparticle excitations cause a bias independent rate as all the excitations are at high energies $|E| > \Delta$ in the BCS density of states. For $eV_b < -\Delta$, even the quasiparticle tunneling is suppressed as there are no occupied states available on the normal metallic leads which could tunnel and fill the vacant excitation states of the superconductor.

The rates at $\delta E < 0$ are not seen in Fig. 2.3 (a) since they are overwhelmed by the opposing rate with $\delta E > 0$. Therefore, typically a single voltage biased NIS junction cannot be used to probe the excitations in a superconductor. However, if the temperature of the superconductor T_S is higher than the temperature of the normal metal T_N, the quasiparticle excitations of the superconductor dominate the current also in a region where $\delta E > 0$. However, as the vacancies on the lower branch of the superconductor generate current with the same magnitude but opposite direction as the particle excitations on the upper branch, the resulting net current is zero. Again the NIS junction cannot be used for probing the total number of excitations on a superconductor. However, it is possible to probe whether the two branches have non-equal number of excitations.

This situation is known as branch imbalance [42]. In order to probe the total number of such excitations, we either need to observe the tunneling events individually or rectify the current to one preferred direction. These options are discussed in Sect. 6.1.

3. Charging energy - the SINIS turnstile

In Sect. 2.2 we calculated the single-electron tunneling rates for a voltage biased NIS junction. Now we extend the discussion to describe a single-electron transistor (SET) [39, 43, 44]. A typical SET studied in this thesis is shown in Fig. 3.1 (a). In this device, we have a normal metallic island (N) contacted to superconducting leads (S) by NIS junctions forming a device called SINIS turnstile. The operation of the SET is controlled by applying bias voltage (V_1 and V_2) and by polarizing the island with a gate voltage V_g. Typically, current I through the device is measured. We first consider the charging energy cost of a small metallic island in Sect. 3.1. Then we discuss in Sect. 3.2 the static operation of the SINIS turnstile and finally in Sect. 3.3 we apply a radio frequency drive to the gate and obtain the quantization of electrical current.

3.1 Energy considerations

In order to describe the transport in an SET, we need to consider the energy required for charging the island with n electrons and include it to the energy gain δE discussed in Sect. 2.2.2. Since electrons tunnel sequentially, we may consider the tunnel junctions of Fig. 3.1 as capacitive elements before and after a tunneling event. Also the gate electrodes are capacitively coupled to the island. These elements are described by capacitances C_i with voltages V_i applied to them. Now let Q_i be the charge at the capacitor i and V_I the voltage at the island. We can express V_I and the charge ne at the island as

$$\begin{cases} V_I &= V_i - \dfrac{Q_i}{C_i} \\ ne &= \displaystyle\sum_i Q_i. \end{cases} \qquad (3.1)$$
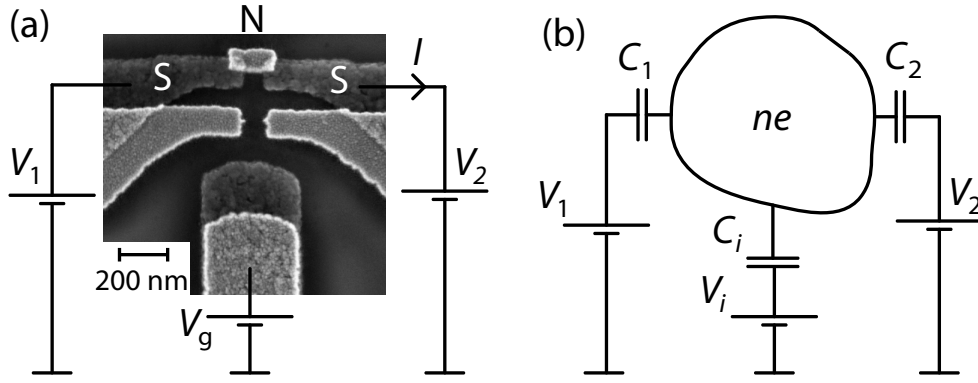
Figure 3.1. Hybrid SET. (a), A typical single electron transistor (SET) studied in this thesis. Superconducting leads (S) are contacted to a normal metallic island (N) by thin insulating barriers (I) to form a SINIS structure. (b), The circuit describing the SET from the point of view of electrostatics. The island has charge ne with n being the number of electrons. For energy considerations the tunnel junctions and the coupling between the gate and the island appear as capacitances C_i connected between voltage sources V_i and the island. We allow here the number of voltage sources to be arbitary and thus we consider a more general situation than in panel (a).

Taking the upper equation for i and j, multiplying by $C_i C_j$ and summing over j leads to

$$Q_i = C_i V_i + \frac{C_i}{C_\Sigma} e(n - n_g), \tag{3.2}$$

where $C_\Sigma = \sum_i C_i$ is the total capacitance to the island and $n_g = \sum_i C_i V_i / e$ the so-called gate offset. Now we are ready to determine the energy stored in the circuit. It is given by the Gibbs free energy where we take the energy stored in the capacitor and substract the energy provided by the voltage sources. We obtain the charging energy as

$$E_{\text{ch}} = \sum_i \left(\frac{Q_i^2}{2C_i} - Q_i V_i \right). \tag{3.3}$$

Plugging Eq. (3.2) to Eq. (3.3) leads to a simple form

$$E_{\text{ch}}(n) = E_c(n - n_g)^2, \tag{3.4}$$

where $E_c = \frac{e^2}{2C_\Sigma}$ is known as the charging energy, a characteristic energy for charging the island by one electron. To obtain Eq. (3.4), we took only the part depending on n, since only the energy differences when n changes are relevant for electron tunneling. When one electron tunnels into (+) or out from (-) the island, the energy gain of charging is

$$\delta E^\pm = -(E_{\text{ch}}(n \pm 1) - E_{\text{ch}}(n)) = \mp 2E_c(n - n_g \pm 1/2). \tag{3.5}$$

In addition we must consider the energy supplied by the voltage source. For an electron which tunnels from the voltage source V_i, the total energy gain is

$$\delta E_i^\pm = \mp 2E_c(n - n_g \pm 1/2) \mp eV_i. \tag{3.6}$$
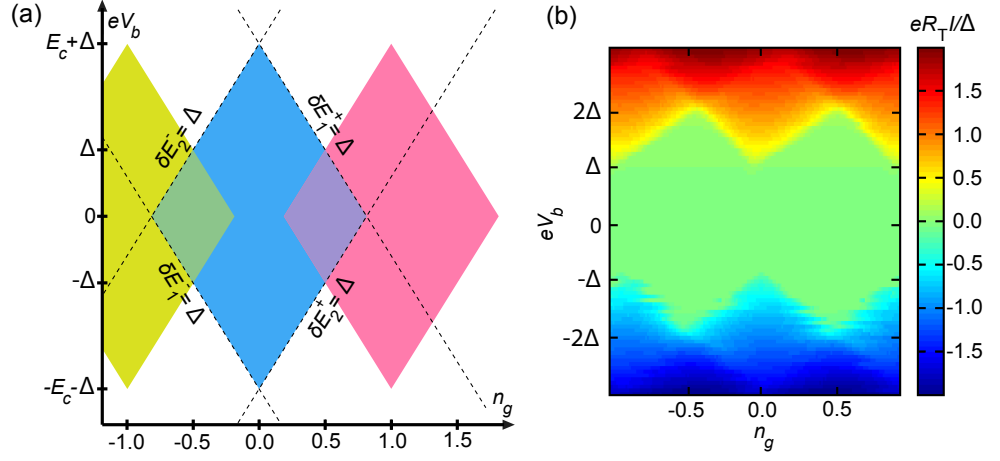
Figure 3.2. Stability diagram of a SINIS turnstile. (a), Tunneling thresholds $\delta E_i^{\pm} = \Delta$ are shown as dotted lines for $n = 0$. These lines bound a Coulomb diamond, shown as a blue region, where the single-electron tunneling is suppressed due to an energy cost. Green and red areas show similar diamonds for $n = -1$ and $n = 1$ respectively. On the white area, none of the charge states n is stable and current runs through the SET. (b), Experimental current - voltage curve of a SINIS turnstile with $E_c = 1.2\Delta$. Coulomb diamonds of panel (a) are represented by the green area with suppressed current ($I = 0$).

The tunneling rates for the corresponding processes are calculated with Eqs. (2.25) and (2.26) by substituting δE by the expression of Eq. (3.6).

Let us now consider the single-electron transistor with normal metallic island and two superconducting leads, see Fig. 3.1 (a). We take $V_b = V_1 = -V_2$ to be the bias voltage per junction. On a qualitative level, the operation of the device can be understood by simple energy considerations. Let us consider the island to have n electrons on the island. The single-electron tunneling is suppressed if none of the tunneling processes gain energy to break a Cooper pair, i.e. $\delta E_i^{\pm} < \Delta$. These conditions bound a region colored blue in Fig. 3.2 (a) for $n = 0$. It is known as a Coulomb diamond. The boundaries of the diamond, $\delta E_i^{\pm} = \Delta$, are known as tunneling thresholds, since once they are crossed, tunneling becomes energetically possible and electron number n changes. At low bias, $|eV_b| < \Delta$, crossing a tunneling threshold leads to another Coulomb diamond, either $n = -1$ or $n = 1$ shown as green and red respectively, and the current is again suppressed. At higher bias, $|eV_b| > \Delta$, there is no stable charge state after crossing the threshold. This means that electron tunneling out of and into the island are both possible and current runs through the device. In Fig. 3.2 (b) experimental data for such a device is shown. The diamonds correspond to a region where the current is suppressed. The size and the shape of the diamonds allow us to obtain a rough estimate of $\Delta = 220~\mu$eV and $E_c = 1.2\Delta$.

It is worthwhile to note that by using a normal metallic island, the supercurrent through the device is suppressed unlike in a fully superconducting SET [1]. In order to have supercurrent in a SINIS transistor, the superconducting leads should induce superconductivity to the island with so-called proximity effect [45], which, however would call for clean metal-to-metal contacts. The tunnel barriers of the turnstile suppress the proximity effect down to a level where it does not influence the turnstile operation.

3.2 Master equation

So far, we have made energy considerations of the SINIS turnstile. Now we consider how the current I through the device is calculated. This is achieved with the help of a master equation. We assign a probability $P(n)$ for having n excess electrons on the island. The time evolution of $P(n)$ with single-electron tunneling is

$$\frac{d}{dt}P(n) = -\Gamma_{n,n}P(n) + \Gamma_{n-1,n}P(n-1) + \Gamma_{n+1,n}P(n+1), \qquad (3.7)$$

where $\Gamma_{n+1,n}$ is the sum of tunneling rates decreasing the electron number from $n+1$ to n and $\Gamma_{n-1,n}$ contains the rates increasing it from $n-1$ to n. $\Gamma_{n,n} = \Gamma_{n,n-1} + \Gamma_{n,n+1}$ is the sum of all rates away from the state with n excess electrons. Once $P(n)$ is known, the current through junction i is obtained as

$$I_i = -e\sum_n P(n)\left[\Gamma_{\mathrm{S}\to\mathrm{N}}\left(\delta E_i^+(n)\right) - \Gamma_{\mathrm{N}\to\mathrm{S}}\left(\delta E_i^-(n)\right)\right]. \qquad (3.8)$$

In Fig. 3.3 (a) we plot I calculated with the master equation and compare the result to experimental data. We observe that there is a decent but not quantitative correspondence if we assume that the system is not overheated. Next we take into account the overheating of the normal metallic island as will be discussed below [16]. This assumption results in a better correspondence between the experimental data and calculations and allows one to extract the value of E_c reliably.

In addition to the electrical current, it is possible to consider heat flow with the master equation approach [46, 47]. Considering overheating is especially important at low temperatures. For example, in order to estimate the device parameters precisely for a SINIS turnstile, the heating of the normal metallic island needs to be considered: the electrons on a small island, operated at low temperatures, are poorly coupled thermally

to the substrate. The heat flow $\dot{Q}$ to the normal metallic island has an expression resembling Eq. (3.8), reading

$$\dot{Q} = \sum_{n,i} P(n) \left[\dot{Q}_{\mathrm{S}\to\mathrm{N}} \left(\delta E_i^+(n) \right) + \dot{Q}_{\mathrm{N}\to\mathrm{S}} \left(\delta E_i^-(n) \right) \right]. \qquad (3.9)$$

Here $\dot{Q}_{\mathrm{S}\to\mathrm{N}}(\delta E_i^+(n))$ and $\dot{Q}_{\mathrm{N}\to\mathrm{S}}(\delta E_i^-(n))$ are the heat fluxes to the island for electrons tunneling in and out from the island with n electrons on the island. Note that for the heat flow into the island, we sum over the two junctions i whereas the electric current through the island is calculated for one of the junctions only. The heat fluxes are calculated with the operator for power deposited to the normal metal as

$$\dot{Q} = \frac{d}{dt} \hat{H}_N = \frac{i}{\hbar} [\hat{H}_T, \hat{H}_N]. \qquad (3.10)$$

As a result of a similar analysis as in Eqs. (2.25) and (2.26), one obtains

$$\dot{Q}_{\mathrm{N}\to\mathrm{S}} = \frac{1}{e^2 R_T} \int_{-\infty}^{\infty} dE \, (-E + \delta E) n_S(E) f_N(E - \delta E) \left(1 - f_S(E)\right), \quad (3.11)$$

and

$$\dot{Q}_{\mathrm{S}\to\mathrm{N}} = \frac{1}{e^2 R_T} \int_{-\infty}^{\infty} dE \, (E + \delta E) n_S(E) (1 - f_N(E + \delta E)) f_S(E). \qquad (3.12)$$

These equations are similar to Eqs. (2.25) and (2.26) but here the integrand contains the energy $E \mp \delta E$ removed from or deposited to the normal metal. The heat flux to the superconductor can be calculated similarly. The only difference in the final result is that the energy removed or deposited is E. Summing the heat fluxes to the normal metal and the superconductor gives the total heat dissipated in the circuit as $P = IV_{\mathrm{tot}}$, where I is the current through the system biased at voltage V_{tot}.

The heat injected to the normal metallic island $\dot{Q}$ of Eq. (3.9) needs to be removed in order to avoid overheating. The bottle neck for heat removal in this case is the electron-phonon coupling [48]. The corresponding heat current is given by [48]

$$\dot{Q}_{\mathrm{e-ph}} = \Sigma V (T_N^5 - T_0^5), \qquad (3.13)$$

where Σ is a material constant, V the volume of the island, T_N the temperature of the normal metallic electrons and T_0 the temperature of the phonons. We let T_N differ from T_0, the latter being at the base temperature of the cryostat, and find its value via the heat balance $\dot{Q} = \dot{Q}_{\mathrm{e-ph}}$. This procedure is done iteratively by calculating the solution of the master equation for various values of T_N. In Fig. 3.3 (a) we show results of such calculations for one of the devices studied. We obtain parameter
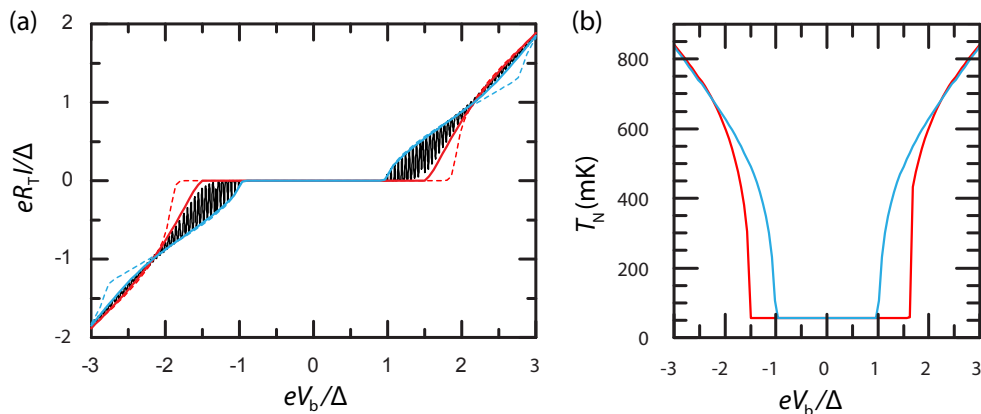
Figure 3.3. Current - voltage curves of a SINIS transistor. (a), Measured current of a SINIS transistor shown as a black line. Gate offset n_g is swept quickly and V_b slowly to obtain the so-called envelope curve where the current oscillates up and down to show the minimal and maximal values. Solid blue and red curves show simulations based on the master equation at $n_g = 0.5$ and $n_g = 0$ respectively. Here the electronic temperature of the island T_N is determined such that the energy balance $\dot{Q} = \dot{Q}_{e-ph}$ holds. Dotted lines show similar simulations but with the island assumed to be fully thermalized to bath temperature. (b), Temperature of the island extracted from simulations of panel (a). Note that T_N increases up to 800 mK already at the bias voltage of $\pm 3\Delta/e$.

values $R_T = 130$ kΩ by fitting the slope at high bias, $\Delta = 216$ μeV by fitting the size of the region with suppressed current, and $E_c/\Delta = 0.9$ by fitting the current - voltage curves at $n_g = 0$ and $n_g = 0.5$. The island volume $V = 700$ nm $\times$ 100 nm $\times$ 30 nm was estimated from a scanning electron micrograph and material constant $\Sigma = 2 \cdot 10^9$ WK^{-5}m^{-3}, consistent with other experiments [16], was used for the copper island. A value $T_0 = 50$ mK was used based on the reading of the thermometer of the cryostat.

We observe that to obtain a good fit, the heating needs to be taken into account. If the island is assumed to be at the base temperature, shown as dotted lines in Fig. 3.3 (a), the fit is not perfect as already pointed out. However, the node points which are at $eV_b \approx \pm 2\Delta$ for Fig. 3.3 (a), are not sensitive to heating but depend on E_c. This fact makes it possible to estimate E_c without performing a tedious overheating analysis. In Fig. 3.3 (b) the electronic temperature of the island is shown. It is extracted from the master equation calculation. We observe that the island heats up to 500 mK and above, which demonstrates the weakness of electron-phonon coupling at low temperatures. Based on Eq. (3.13), the temperature of the cryostat, assumed to be equal to the phonon temperature T_0, is fully irrelevant in this situation.
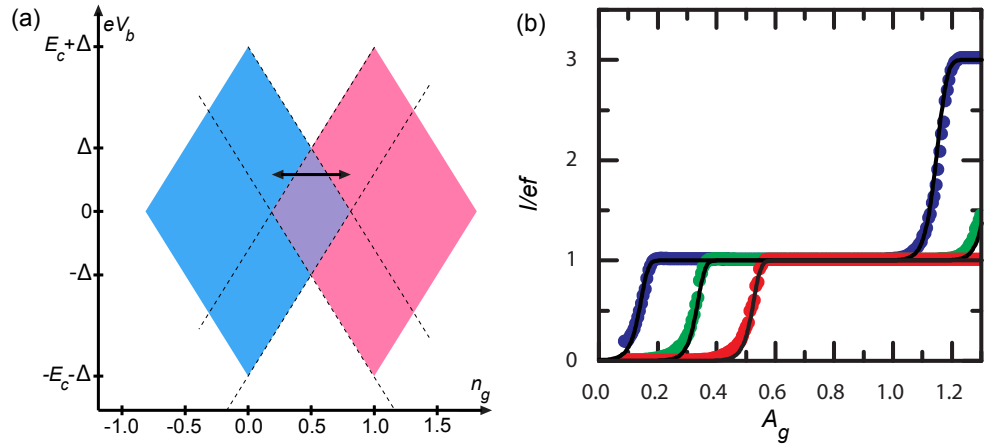
Figure 3.4. Quantized current in a SINIS transistor. (a), A stability diagram presenting the electron transfer. By moving between two Coulomb diamonds cyclically at $|eV_b| < \Delta$, one electron is taken into the island and another pushed out in each cycle. With non-zero V_b, the electrons have a preferred direction for tunneling and current $I = ef$ results. (b), Measured current plateau of a SINIS turnstile (dots) and simulations based on Eq. (3.7) shown as black lines.

3.3 Current quantization in the SINIS turnstile

In Sect. 3.2 we considered the operation of a SINIS turnstile under fixed (time-independent) conditions and saw that the current is suppressed for $|eV_b| < \Delta$. Now we apply a periodic drive to the gate offset n_g and find out that quantized electrical current is obtained [34] in similar way as in the normal metallic turnstiles [31]. When a non-zero bias voltage with $|eV_b| < \Delta$ is applied, the electron tunneling has a preferred direction. As n_g is changed such that we move between two stability diamonds as shown in Fig. 3.4 (a), one electron is pulled into the island from one junction and another one is pushed out from the opposite one. This leads to one electron being transported through the device in each cycle. In Fig. 3.4 (b) experimental data in such an operation is shown for three different bias voltages $V_b = 60, 110, 160$ μV as red, green and blue points. Note that here and throughout in this thesis we give the bias values per junction. For a SINIS turnstile, the total bias voltage is then twice this value. Device parameter values are $R_T = 155$ kΩ, $\Delta = 216$ μeV and $E_c = 0.63\,\Delta$. The drive frequency is $f = 10$ MHz. We observe that the measured current I forms a plateau at the value ef which indicates that electrons are being transported one by one. The rise to the plateau and beyond it are determined by the tunneling thresholds. The higher the bias, the earlier the current increases as a function of the gate amplitude A_g.

The shape of these current-voltage curves can be calculated by solving

Eq. (3.7) numerically and calculating the average current of one cycle with Eq. (3.8). We show the resulting current curves in Fig. 3.4 (b) as solid black lines and we see that the overall features of the pumping plateau are described well by the sequential single-electron tunneling model. In the forthcoming chapters, we consider the current at the plateau and different processes which influence the value of the current at the plateau. We will see that many of the error sources can be suppressed and hence we expect the device to reach a relative accuracy on the level of 10^{-7} or below [49]. This would be just barely sufficient for metrological applications [50–52].

It is advisable to operate the SINIS turnstile at the highest possible frequency since it results in maximal output current and minimizes possible frequency independent errors such as thermal errors [34]. High currents are preferred since they are easier to measure precisely. The current of the turnstile is limited by an average time τ_{tun} needed for an electron tunneling event to occur. In order to avoid missed tunneling events, the requirement $\tau_{\mathrm{tun}} \ll 1/\Gamma$ must be satisfied, where Γ is the tunneling rate of the process. The tunneling rate Γ scales linearly with the tunnel junction conductance $G_T = R_T^{-1}$. However, G_T must be limited to avoid errors arising from higher order tunneling processes [49]. Thus the highest output current of a single turnstile is few tens of picoamperes if the relative accuracy of 10^{-7} is required [49, 53].

One of the advantages of the SINIS turnstile is that the operation principle is simple. This allows to obtain higher output currents with parallelization. In Publication I, we have shown that ten such devices can be operated in parallel. A reason hindering a large scale parallelization of any single-electron device is the presence and the variation of the offset charges nearby the islands. These are random and they have to be compensated for each SET island separately by a gate voltage. This is the main drawback of the devices which provide today the best quantization accuracy. These devices are based on N normal metallic islands tunnel coupled in series and they reach a relative uncertainty of 10^{-8} for the current quantization [25, 28]. However, the obtainable output current of the order of $1 \ \mathrm{pA}$ is two to three orders of magnitude below the required level for quantum metrological applications, apart from the capacitance standard [32]. The SINIS turnstile has two benefits over the normal metallic arrays in terms of output current. First, the obtainable current is $(N+1)/2$ times higher since a cycle involves only two tunneling events whereas in the array $N+1$ events are present. On the other hand,

with the gate control of N islands in the array, we can control N turnstiles in parallel. With the same complexity in the experimental setup, we can thus obtain roughly a factor of $N^2/2$ higher currents with a SINIS turnstile. With the ten devices of Publication I, 100 pA output current sufficient for metrological applications [50, 51] was obtained.

4. Environmentally activated tunneling

In the considerations of Sect. 2.2.2 we assumed ideal voltage bias for the tunnel junctions. The energy conservation required then that the electrons gain or lose always a known amount of energy set by the voltage sources and charging effects. In the energy diagrams of Fig. 2.4, this was seen as electrons tunneling always horizontally. However, the experiments are typically carried out in a non-ideal configuration. Instead of an ideal voltage bias, there are voltage fluctuations present which are modelled with a photon bath [23, 54, 55]. With this relatively simple model, several experimental observations are explained, see e.g. Refs. [56, 57]. These fluctuations may arise from a dissipative circuit near the device, from thermal radiation, from the electronics used in the measurements or they can be inherent for the device, as is the case for shot-noise in electron tunneling [58, 59]. If the photons carry sufficiently large energy, $E \gtrsim \Delta$, they may provide it to the electrons so that they are able to create excitations in a superconductor and therefore single-electron tunneling becomes activated even when it would otherwise be suppressed. In this chapter, we consider this effect with the so-called $P(E)$ theory [23]. In Sect. 4.1 we first review the results of the $P(E)$ theory. Then in Sect. 4.2 we show theoretically and experimentally that a hot resistive environment is an origin of Dynes density of states in NIS junctions. Finally in Sect. 4.3, the low bias leakage of NIS junctions is considered for other environments as well.

4.1 The $P(E)$ theory

In the $P(E)$ theory the electromagnetic environment is modelled with a frequency dependent impedance $Z(\omega)$. We take it to have temperature T_{env} which may differ from the temperature where the tunnel junctions
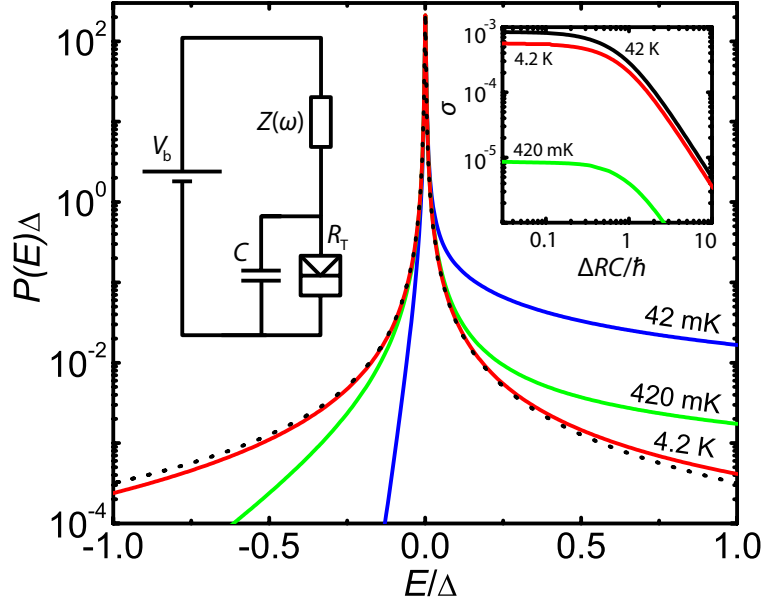
Figure 4.1. Photon assisted tunneling. The probability density $P(E)$ that the environment absorbs energy E from an electron which tunnels. The different curves correspond to different temperatures of the environment. We have taken $\sigma_0 = \frac{R}{R_Q} \frac{k_B T_{\mathrm{env}}}{\Delta} = 10^{-3}$, which determines the leakage at high temperature and low capacitance, for all the curves. Here the environmental impedance $Z(\omega)$ is taken to be resistive with resistance R. T_{env} is the temperature of the environment and $R_Q = \hbar/e^2$. Dotted line is the analytic expression of Eq. (4.21). The schematic shows a single NIS junction biases by voltage V_b. However, the environmental impedance $Z(\omega)$ makes this voltage fluctuate. These fluctuations are shunted by capacitance C. Panel on the right shows the effective leakage σ for a single junction as a function of C. Figure adapted from Publication II.

are located. In addition to $Z(\omega)$ we include also a capacitance C to shunt the junctions for demonstrating that at large enough values of C the photons are not coupled to the junction. The circuit we consider is shown in Fig. 4.1 for a single junction. The results apply directly also to multijunction circuits such as a SET with rescaled parameter values [23]. The impedance $Z(\omega)$ and the capacitance C, forming the total impedance $Z_t(\omega) = (Z(\omega)^{-1} + i\omega C)^{-1}$, are modelled by a set of harmonic oscillators, see Eqs. (2.8) and (2.10). Now we relax the assumption $\delta\hat{V} = 0$, which was done to obtain Eq. (2.22). If that assumption is not made, we have

$$
\begin{aligned}
\Gamma_{N\to S} = \quad & \frac{1}{\hbar^2} \int_{-t_0}^{t} dt' \sum_{kq\sigma} |t_{kq}|^2 \Big\{ \\
& |v_{q\sigma}|^2 \, e^{\frac{i}{\hbar}(\epsilon_k + E_{-q})(t-t')} f_k f_{-q} \langle e^{i\hat{\varphi}(t)} e^{-i\hat{\varphi}(t')} \rangle_0 \\
+ \; & |u_{q\sigma}|^2 \, e^{\frac{i}{\hbar}(\epsilon_k - E_{-q})(t-t')} f_k (1-f_q) \langle e^{i\hat{\varphi}(t)} e^{-i\hat{\varphi}(t')} \rangle_0 \\
+ \; & |v_{q\sigma}|^2 \, e^{-\frac{i}{\hbar}(\epsilon_k + E_{-q})(t-t')} f_k f_{-q} \langle e^{i\hat{\varphi}(t')} e^{-i\hat{\varphi}(t)} \rangle_0 \\
+ \; & |u_{q\sigma}|^2 \, e^{-\frac{i}{\hbar}(\epsilon_k - E_{-q})(t-t')} f_k (1-f_q) \langle e^{i\hat{\varphi}(t')} e^{-i\hat{\varphi}(t)} \rangle_0 \Big\} .
\end{aligned}
\tag{4.1}
$$

We see that the effect of the environment in described by terms $\langle e^{i\hat{\varphi}(t_1)}e^{-i\hat{\varphi}(t_2)}\rangle_0$. For the coupling of the photon bath to the tunnel junction we assume it to be linear in bosonic annihilation and creation operators [60], i.e.

$$\hat{\varphi}(t) = \sum_\lambda c_\lambda b_\lambda^\dagger(t) + h.c. = \sum_\lambda c_\lambda b_\lambda^\dagger e^{i\omega_\lambda t} + h.c., \qquad (4.2)$$

where c_λ are constants defining the environment and its coupling and $h.c.$ stands for hermitian conjugate. To proceed, we used identity $e^{\hat{A}+\hat{B}} = e^{\hat{A}}e^{\hat{B}}e^{-[\hat{A},\hat{B}]/2}$, which holds if $[\hat{A}, \hat{B}]$ commutes with $\hat{A}$ and $\hat{B}$. Since

$$[i\hat{\varphi}(t), i\hat{\varphi}(t')] = \sum_\lambda |c_\lambda|^2 \left(e^{i\omega_\lambda(t-t')} - e^{-i\omega_\lambda(t-t')}\right) = c(t-t') \qquad (4.3)$$

is a complex number, it commutes with $i\hat{\varphi}(t)$ and $i\hat{\varphi}(t')$. Therefore we obtain

$$e^{i\hat{\varphi}(t)}e^{-i\hat{\varphi}(t')} = e^{-c(t-t')/2}e^{i(\hat{\varphi}(t)-\hat{\varphi}(t'))}. \qquad (4.4)$$

Next, we use the identity $\left\langle e^{\hat{A}}\right\rangle_0 = e^{\frac{1}{2}\langle\hat{A}^2\rangle_0}$, which holds for thermal average where $\hat{A}$ is a linear combination of bosonic creation and annihiliation operators. Also, we are interested only on the steady-state case when the time difference $t - t'$ matters but not the initial time. Therefore we may set $t' = 0$ without losing generality, and remember that t is the time difference. Then we have

$$\left\langle e^{i\hat{\varphi}(t)}e^{-i\hat{\varphi}(0)}\right\rangle_0 = e^{J(t)}, \qquad (4.5)$$

where

$$J(t) = -\frac{1}{2}\left(c(t) + \left\langle (\hat{\varphi}(t) - \hat{\varphi}(0))^2\right\rangle_0\right). \qquad (4.6)$$

By using Eq. (4.2), we obtain

$$J(t) = \sum_\lambda |c_\lambda|^2 \left\{e^{i\omega_\lambda t}n(\omega_\lambda) + e^{-i\omega_\lambda t}(n(\omega_\lambda) + 1) - (2n(\omega_\lambda) + 1)\right\}, \qquad (4.7)$$

where $n(\omega_\lambda) = \left\langle b_\lambda^\dagger b_\lambda\right\rangle_0 = (e^{\beta_{\text{env}}\hbar\omega_\lambda} - 1)^{-1}$, is the Bose-Einstein distribution at thermal equilibrium with $\beta_{\text{env}} = 1/(k_B T_{\text{env}})$. Now we express $J(t)$ in frequency basis as

$$J(t) = \int d\omega e^{-i\omega t}\sum_\lambda |c_\lambda|^2\left\{\delta(\omega+\omega_\lambda)n(\omega_\lambda)+\delta(\omega-\omega_\lambda)(n(\omega_\lambda)+1)-\delta(\omega)(2n(\omega_\lambda)+1)\right\},$$
$$(4.8)$$

and use the fluctuation dissipation theorem [61] to link it to the environmental impedance $Z_t(\omega)$. For voltage fluctuations across the impedance $Z_t(\omega)$ we have

$$\left\langle \delta\hat{V}^2\right\rangle = \hbar\omega\text{Re}(Z_t(\omega))\coth(\beta_{\text{env}}\hbar\omega/2). \qquad (4.9)$$

The voltage fluctuations can be related to the phase fluctuations as

$$\hat{\phi} = \frac{e}{\hbar} \int dt \delta \hat{V} \Rightarrow \left\langle \hat{\phi}^2 \right\rangle = \frac{e^2}{(\hbar\omega)^2} \left\langle \delta \hat{V}^2 \right\rangle = \frac{e^2}{\hbar\omega} \mathrm{Re}(Z_t(\omega)) \coth(\beta_{\mathrm{env}}\hbar\omega/2).$$
(4.10)

On the other hand, from Eq. (4.2) we obtain

$$
\begin{aligned}
\left\langle \hat{\phi}^2 \right\rangle &= \frac{1}{2} \int dt e^{i\omega t} \left\langle \left\{ \hat{\varphi}(t), \hat{\varphi}(0) \right\} \right\rangle_0 \\
&= 2\pi \sum_\lambda |c_\lambda|^2 \left(n\left(\omega_\lambda\right) + 1/2 \right) \left(\delta(\omega + \omega_\lambda) + \delta(\omega - \omega_\lambda) \right).
\end{aligned}
$$
(4.11)

Combining Eqs. (4.10) and (4.11) leads to

$$
\begin{aligned}
&\sum_\lambda |c_\lambda|^2 \left(n\left(\omega_\lambda\right) + 1/2 \right) \left(\delta(\omega + \omega_\lambda) + \delta(\omega - \omega_\lambda) \right) \\
&= \frac{\mathrm{Re}(Z_t(\omega))}{\omega R_K} \coth(\beta_{\mathrm{env}}\hbar\omega/2),
\end{aligned}
$$
(4.12)

where $R_K = h/e^2$ is the resistance quantum, also known as the von Klitzing constant [62]. Next, we want to plug the result of Eq. (4.12) to Eq. (4.8). In addition, we need the zero temperature limit of Eq. (4.12). Since, $\omega_\lambda > 0$, by letting $T_{\mathrm{env}} \to 0$, we have

$$
\begin{cases}
\frac{1}{2} \sum_\lambda |c_\lambda|^2 \delta(\omega + \omega_\lambda) = -\frac{\mathrm{Re}(Z_t(\omega))}{\omega R_K}, & \omega > 0 \\
\frac{1}{2} \sum_\lambda |c_\lambda|^2 \delta(\omega - \omega_\lambda) = +\frac{\mathrm{Re}(Z_t(\omega))}{\omega R_K}, & \omega < 0.
\end{cases}
$$
(4.13)

Plugging Eqs. (4.12) and (4.13) to Eq. (4.8) leads to

$$
\begin{aligned}
J(t) = \ &2 \int_0^\infty \frac{d\omega}{\omega} \frac{\mathrm{Re}(Z_t(\omega))}{R_K} \left\{ \coth\left(\frac{\beta_{\mathrm{env}}\hbar\omega}{2} \right) \cos\omega t - i \sin\omega t \right\} \\
&- 2 \sum_\lambda |c_\lambda|^2 \left(n\left(\omega_\lambda\right) + 1/2 \right) \delta(\omega)
\end{aligned}
$$
(4.14)

From Eq. (4.7) we see that $J(0) = 0$. Requiring this for Eq. (4.14) yields, $\sum_\lambda |c_\lambda|^2 \left(n\left(\omega_\lambda\right) + 1/2 \right) \delta(\omega) = \int_0^\infty \frac{d\omega}{\omega} \frac{\mathrm{Re}(Z_t(\omega))}{R_K} \coth\left(\frac{\beta_{\mathrm{env}}\hbar\omega}{2} \right)$ and we finally obtain

$$J(t) = 2 \int_0^\infty \frac{d\omega}{\omega} \frac{\mathrm{Re}(Z_t(\omega))}{R_K} \left\{ \coth\left(\frac{\beta_{\mathrm{env}}\hbar\omega}{2} \right) (\cos\omega t - 1) - i \sin\omega t \right\},$$
(4.15)

which is the result in Ref. [23]. We continue now with Eq. (4.1). Taking $t_0 \to \infty$ we get

$$
\begin{aligned}
\Gamma_{N \to S} = \ &\frac{1}{\hbar^2} \int_{-\infty}^\infty dt \sum_{kq\sigma} |t_{kq}|^2 \left\{ |v_{q\sigma}|^2 \, e^{\frac{it}{\hbar}(\epsilon_k + E_{-q})} f_k f_{-q} e^{J(t)} \right. \\
&\left. + |u_{q\sigma}|^2 \, e^{\frac{it}{\hbar}(\epsilon_k - E_{-q})} f_k (1 - f_q) e^{J(t)} \right\}.
\end{aligned}
$$
(4.16)

Now we define a function

$$P(E) = \frac{1}{2\pi\hbar} \int dt \, e^{J(t)} e^{\frac{it}{\hbar}E},$$
(4.17)
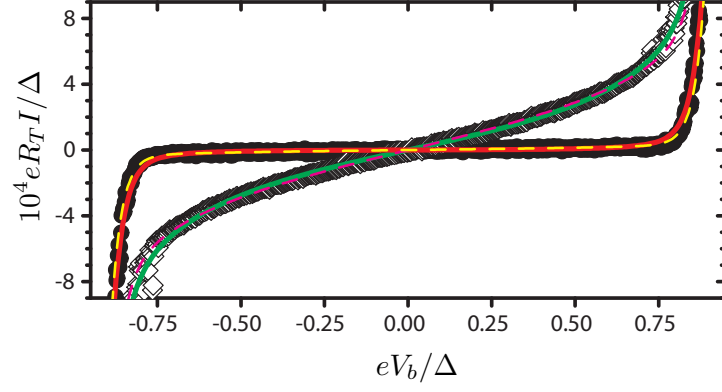
Figure 4.2. Leakage current of an NIS junction caused by electromagnetic environment. Measured IV curves of an NIS junction with $R_T = 761$ kΩ on the ground plane (solid symbols) and of a similar junction with $R_T = 627$ kΩ without the ground plane (open symbols). Solid lines present the results of the full $P(E)$ theory for capacitance $C = 10$ pF (red line) and $C = 0.3$ pF or smaller (green line). The resistance and the temperature of the environment are set to $R = 2$ Ω and $T_{\mathrm{env}} = 4.2$ K, respectively, and $\Delta = 200$ μeV. The dashed lines correspond to the Dynes model with the parameters yielding the best fit to the data. The normalized zero-bias slope is 5.3×10^{-4} for the green line and 2.6×10^{-5} for the red line.

and obtain

$$
\Gamma_{N \to S} = \frac{2\pi}{\hbar} \sum_{kq\sigma} |t_{kq}|^2 \left\{ |v_{q\sigma}|^2 P(\epsilon_k + E_{-q}) f_k f_{-q} \right.
$$
$$
\left. + |u_{q\sigma}|^2 P(\epsilon_k - E_{-q}) f_k (1 - f_q) \right\}.
$$
(4.18)

Finally, we change the summing to integration and make a change of variables to the $v_{q\sigma}$ term and obtain

$$
\Gamma_{N \to S}(\delta E) = \frac{1}{e^2 R_T} \int d\epsilon\, dE\, n_S(E) f_N(\epsilon - \delta E)(1 - f_S(E)) P(\epsilon - E). \quad (4.19)
$$

This reduces to Eq. (2.25) if $Z_t(\omega) = 0$. In that particular case $P(E) = \delta(E)$. From Eq. (4.19) the $P(E)$ function can be interpreted as a probability density that the electron which tunnels, emits energy E to the impedance $Z_t(\omega)$. Note that $P(-E)$ is then the probability density of the electron to absorb energy E. By calculating the remaining terms, we obtain the tunneling rate to the reverse direction as

$$
\Gamma_{S \to N}(\delta E) = \frac{1}{e^2 R_T} \int d\epsilon\, dE\, n_S(E)(1 - f_N(\epsilon + \delta E)) f_S(E) P(E - \epsilon). \quad (4.20)
$$

With Eqs. (4.19) and (4.20) we are now ready to consider quantitatively the effect of the environment to an NIS junction.

4.2 Electromagnetic environment as an origin of Dynes DoS

We consider now a hot resistive environment with resistance $R \ll R_K$. With this impedance, the noise spectrum is white with a thermal cutoff. In

Publication II the resistive environment was utilized to show theoretically as well as experimentally that environmentally activated tunneling gives rise to leakage at sub-gap voltages in NIS junction based devices and it accounts for the phenomenological Dynes DoS typically used for modelling the leakage [63, 64]. In Fig. 4.1 the $P(E)$ function is presented for various temperatures T_{env} and shunting capacitances C. If the temperature of the environment satisfies $T_{\text{env}} > E/k_B$ and the the capacitance is low, $C < \hbar/(\Delta R)$, the $P(E)$ function of Eq. (4.17) is approximately Lorenzian:

$$P(E) = \frac{1}{\pi\Delta} \frac{\sigma_0}{\sigma_0^2 + (E/\Delta)^2}, \qquad (4.21)$$

where $\sigma_0 = \frac{R}{R_Q} \frac{k_B T_{\text{env}}}{\Delta}$ and $R_Q = \hbar/e^2$. See supplemental material of Publication II for derivation. When this is plugged into Eqs. (4.19) and (4.20) and the current through a voltage biased NIS junction, $I = e(\Gamma_{N\to S} - \Gamma_{S\to N})$, is evaluated, we obtain the same result as if we would do the calculation in the absence of the environment (Eqs. (2.25) and (2.26)) but use for the superconductor an effective density of states

$$n_S^\sigma(E) = \left| \text{Re} \left(\frac{E/\Delta + i\sigma}{\sqrt{(E/\Delta + i\sigma)^2 - 1}} \right) \right|, \qquad (4.22)$$

which is known as the Dynes density of states [63, 64]. Here $\sigma = \sigma_0$ is taken as a lifetime broadening of a level at energy E. For the derivation, see supplemental material of Publication II. Typically $\sigma = 10^{-3} \ldots 10^{-6}$ for aluminum based devices, so that the level broadening effect is small. In addition to the small broadening around energy E, the finite lifetime in Dynes DoS results in electronic states which are distant from the non-broadened energy levels. From Eq. (4.22) we see that we obtain states into the superconductor gap $|E| < \Delta$. For small energies E, we have $n_S^\sigma(E) \approx \sigma$. These subgap states cause linear leakage at low bias $|eV_b| < \Delta$ and thus the Dynes DoS is often used to account such features in the experiment [65–70]. In view of the electro-magnetic environment as the origin of the Dynes DoS, these are not true electronic states but a result of photons providing the required energy for the unpaired electron in the superconductor. This was proven by measuring two NIS junctions, where one was on top of a ground plane and another one did not have it. The results are shown in Fig. 4.2. The device on top of the ground plane shows the anticipated linear leakage at low bias which is suppressed by an order of magnitude as compared to the junction off the ground plane. Inserting the ground plane increases the capacitance C between the junction electrodes. The voltage fluctuations are then suppressed and hence

σ is decreased, see Fig. 4.1. This experiment demostrates that one needs to shield carefully the sample against the fluctuations. The same effect was shown in Publication III in an electron counting experiment. The technique is discussed in detail in Sect. 5.3.

4.3 Subgap leakage of NIS junctions

The discussion of the leakage current of an NIS junction studied in Publication II was extended in Publication X to the case of a general $Z(\omega)$. The obtained results are limited to low bias voltages $|eV_b| < \Delta$. In other words, the emphasis is put on describing the subgap leakage and the broadening at $|eV_b| > \Delta$ is not considered. In addition, the temperatures T_N and T_S at the junction are assumed to satisfy $T_N, T_S \ll \Delta/k_B$. Under these assumptions, the subgap current arising from environmental activation reads

$$I_{sg} \approx \sigma_{env}\frac{V}{R_T},\tag{4.23}$$

where we have the leakage parameter

$$\sigma_{env} = 2\int_\Delta^\infty dE\, n_S(E)P(-E).\tag{4.24}$$

Furthermore, expanding $P(E)$ of Eq. (4.17) up to the first order of $J(t)$ yields

$$\begin{aligned}
P(E) &\approx \frac{1}{2\pi\hbar}\int dt\, e^{iEt/\hbar}[1 + J(t)]\\
&\approx \delta(E) + \frac{1}{\hbar}\int_0^\infty \frac{d\omega}{\omega}\frac{\mathrm{Re}(Z_t(\omega))}{R_K}\left\{\left[\coth(\beta_{env}\hbar\omega/2) - 1\right]\delta(E/\hbar + \omega)\right.\\
&\left.+\left[\coth(\beta_{env}\hbar\omega/2) + 1\right]\delta(E/\hbar - \omega) - 2\hbar\coth(\beta_{env}\hbar\omega/2)\delta(E)\right\}.
\end{aligned}\tag{4.25}$$

In this form, the $P(E)$ function consists of both elastic and inelastic contributions. The inelastic one involves an exchange of exactly one photon between the junction and environment. In such one photon regime, the environment is weakly coupled to the junction. Evaluating the integral over ω and plugging the result into Eq. (4.24) yields

$$\sigma_{env} = 4\int_\Delta^\infty dE\, n_S(E)\frac{\mathrm{Re}(Z_t(\omega))}{R_K}\frac{n(E)}{E},\tag{4.26}$$

where $n(E) = (e^{\beta_{env}E} - 1)^{-1}$ is the Bose-Einstein distribution of the photons. Equation (4.26) allows one to evaluate the low bias leakage for any environment weakly coupled to the junction. For the validity of the

weak coupling, see details in Publication X. With a resistive environment, Eq. (4.26) reduces to the result obtained in Sect. 4.2. An effective approach to suppress the leakage current is to place a resistive transmission line between the hot environment and the junction. A relevant parameter for the leakage suppression is the transmission coefficient $\mathcal{T}_C(\omega)$, which defines the damping of voltage fluctuations at frequency ω when passing the transmission line. In Publication X it was shown that with the transmission line $|\mathcal{T}_C(E/\hbar)|^2$ appears in the integrand of Eq. (4.26). The transmission coefficient $\mathcal{T}_C$ decreases exponentially as the length l or the resistivity per unit length R_0 of the line increases. Thus the subgap leakage was shown to scale as $\sigma_{\mathrm{env}} \propto e^{-l\sqrt{2\Delta R_0 C_0/\hbar}}$, where C_0 is the capacitance per unit length of the line. Utilizing the exponential suppression, it is possible to reach $\sigma_{\mathrm{env}} \lesssim 10^{-7}$, as shown experimentally in Publication VI.

Suppressing the environmentally activated tunneling and obtaining a small value for σ_{env} has a direct influence on the current quantization accuracy of a SINIS turnstile. The influence of environmentally activated tunneling on the turnstile was experimentally demonstrated in Publication II by comparing a turnstile with and without the ground plane. Protection against environmentally activated tunneling is of paramount importance also for the experiments on Andreev tunneling of Chapter 5 and on quasiparticle excitations of Chapter 6. In these experiments, a ground plane, a better shielded sample holder or both were utilized for the protection. As a final remark of this chapter, we note that the electromagnetic environment not only causes spurious effects. By engineering it, the tunneling rates can be influenced in a way which improves the performance of the turnstile or other SET devices [71–73].

5. Higher order processes - Andreev tunneling

In Chapter 2 sequential single-electron tunneling in NIS junctions was discussed. This is often the dominant mechanism of charge transport. Multi-electron processes are especially important in the subgap regime where the bias voltage per junction satisfies $|V_b| < \Delta/e$ and single-electron processes are suppressed, see Figs. 2.2 (b) and 2.3. In this case, multi-electron processes which avoid Cooper pair breaking are energetically favorable. One such process is elastic cotunneling, where an electron first tunnels from normal metal to a superconductor and then coherently to another normal metal [49, 74]. For the NISIN transistor of Sect. 6.4 this process is possible but the rates are lower than what we can detect with direct current measurements [74, 75]. For the other structures of this thesis cotunneling without breaking Cooper pairs is not allowed ideally since the second normal metallic part is missing. Therefore we neglect it in this thesis.

The other two-electron process avoiding the pair breaking energy cost involves a Cooper pair tunneling into a normal metal as two unbound electrons or reversely two electrons from the normal metal tunnel into the superconductor and form a Cooper pair. Processes, where normal metallic electrons are converted to Cooper pairs or vice versa are known as Andreev processes [2]. In the case of tunnel junctions we use the term "Andreev tunneling" since it corresponds to a two-electron tunneling process. Being the simplest process which avoids Cooper pair breaking, Andreev tunneling is also the one which produces typically the largest current. As more and more electrons are involved in a multi-electron process, the magnitude of the resulting current decreases. This is because the probability for N electrons to tunnel in the process is proportional to $\mathcal{T}^N$, where $\mathcal{T} \ll 1$ is an average transmission probability for a single-electron [76]. The process being energetically possible and involving the smallest num-

ber of electrons is hence dominant. This is reflected in the resulting tunneling rate of an N electron process which scales as R_T^{-N}.

In this chapter, we consider Andreev tunneling in NIS junctions [3–6, 8, 70, 77]. We first determine the tunneling rates and then discuss how to observe them experimentally. We also demonstrate experimentally that the Andreev tunneling can be suppressed with charging energy costs. This makes three-electron processes dominant [49]. We will also see that the Andreev tunneling imposes constraints to the design of a SINIS turnstile when maximal accuracy is pursued.

5.1 Determination of Andreev tunneling rates

The tunneling rates for Andreev tunneling are obtained similarly as the single-electron rates. In this case, we take the second non-zero term in the series expansion of Eq. (2.18). Plugging this into $I = \mathrm{Tr}(\rho_I \hat{I}_I)$ yields

$$I_{\mathrm{AR}} = -\frac{i}{\hbar^3} \int_{t_0}^{t} dt_1 \int_{t_0}^{t_1} dt_2 \int_{t_0}^{t_2} dt_3 \left\langle \left[\hat{H}_T(t_3), \left[\hat{H}_T(t_2), \left[\hat{H}_T(t_1), \hat{I}(t) \right] \right] \right] \right\rangle_0 \quad (5.1)$$

Following the same steps as for the first order, collecting only terms not containing energy cost of Δ and taking terms corresponding to tunneling from normal metal to superconductor, one arrives at the Andreev tunneling rate

$$\Gamma_{\mathrm{N \to S}}^{\mathrm{AR}}(\delta E) = \frac{\hbar \Delta^2}{16 \pi e^4 R_T^2 \mathcal{N}} \int d\epsilon \, f_N(\epsilon - \delta E/2) f_N(-\epsilon - \delta E/2) \times$$
$$\left| a(\epsilon + E_C - i\delta\epsilon/2) + a(-\epsilon + E_C - i\delta\epsilon/2) \right|^2, \quad (5.2)$$

where

$$a(\epsilon) = \frac{1}{\sqrt{\epsilon^2 - \Delta^2}} \ln \left(\frac{\Delta - \epsilon + \sqrt{\epsilon^2 - \Delta^2}}{\Delta - \epsilon - \sqrt{\epsilon^2 - \Delta^2}} \right), \quad (5.3)$$

and δE is the electrostatic energy gained for the two electrons which tunnel [49, 78]. By considering n changing by two in Eq. (3.4) and taking into account that two electrons are provided by the voltage supply V_i, we obtain the energy gain for adding $(++)$ or removing $(--)$ two electrons from the SET island as

$$\delta E_i^{\pm\pm} = E_c(n - n_g)^2 - E_c(n \pm 2 - n_g)^2 \mp 2eV_i = \mp 4E_c(n - n_g \pm 1) \mp 2eV_i. \quad (5.4)$$

Similarly as for the single-electron tunneling rates of Eqs. (2.25) and (2.26), for Andreev tunneling we also have $\Gamma_{\mathrm{N \to S}}^{\mathrm{AR}}(\delta E) = \Gamma_{\mathrm{S \to N}}^{\mathrm{AR}}(\delta E)$, i.e. the tunneling direction does not matter for a given energy gain δE.

For obtaining Eq. (5.2) a few remarks need to be made. First of all, it was taken into account that the junction consists of several conduction
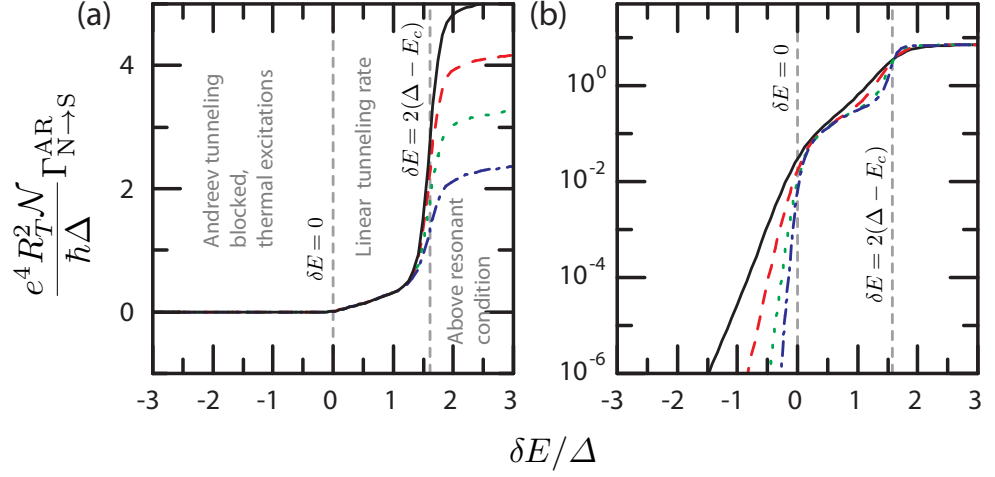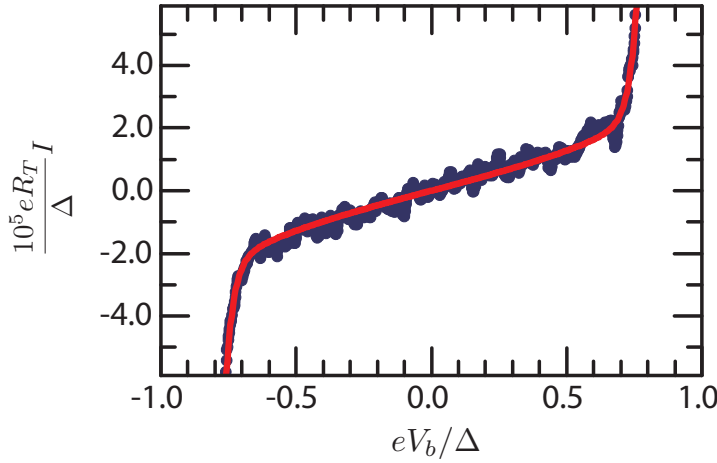
Figure 5.1. Andreev tunneling rates. (a), Andreev tunneling rate $\Gamma^{\mathrm{AR}}_{\mathrm{N}\to\mathrm{S}}$ as a function of the energy gain δE. The curves from top to bottom are calculated with $\hbar\sum_{\pm}\Gamma_{\mathrm{N}\to\mathrm{S}}(\delta E^{\pm})/\Delta = 10^{-5}, 10^{-4}, 10^{-3}$ and 10^{-2} respectively. The tunneling threshold $\delta E = 0$ and the resonant condition $\delta E = 2(\Delta - E_c)$ are shown as dotted grey lines. Curves are calculated with $\Delta/k_B T_N = 40$. (b), Similar curves but for different temperatures $\Delta/k_B T_N = 10, 15, 25$ and 40. Here we use $\hbar\sum_{\pm}\Gamma_{\mathrm{N}\to\mathrm{S}}(\delta E^{\pm})/\Delta = 10^{-5}$.

channels; $\mathcal{N}$ is the effective number of them. This scales the tunneling rate as $1/\mathcal{N}$ compared to the result obtained with a single channel. We can express the number of conduction channels as $\mathcal{N} = A/A_{\mathrm{ch}}$, where A_{ch} is the area of one channel and A the total area of the junction. For aluminum oxide tunnel barriers, we expect $A_{\mathrm{ch}} = 2$ nm^2 based on the estimate given in Publication IV. Experimental findings in Publication IV, Publication V and Refs. [5, 70] suggest, however, that the actual value for A_{ch} is roughly an order of magnitude higher resulting in an order of magnitude higher tunneling rate than expected.

Secondly, we have introduced a lifetime broadening with a term $i\delta\epsilon = i\hbar\sum_{\pm}\Gamma_{\mathrm{N}\to\mathrm{S}}(\delta E^{\pm})$ to Eq. (5.2). Otherwise the Andreev tunneling rate would diverge. The broadening is determined by the first order tunneling rates $\sum_{\pm}\Gamma_{\mathrm{N}\to\mathrm{S}}(\delta E^{\pm})$, which according to the uncertainty relation make the energy states uncertain as the lifetime of the state is finite. In Fig. 5.1 (a) we have plotted $\Gamma^{\mathrm{AR}}_{\mathrm{N}\to\mathrm{S}}$ for different values of $\delta\epsilon$. The rate depends only logarithmically on $\delta\epsilon$ and only if the energy gain in Andreev process satisfies $\delta E_i^{\pm\pm} > 2(\Delta - E_c)$, which corresponds to the competing single-electron tunneling threshold condition $\delta E_i^{\pm} > \Delta$. In this thesis we focus mainly on Andreev tunneling rates at $\delta E_i^{\pm\pm} < 2(\Delta - E_c)$, where they are not sensitive to the broadening. Because of these two reasons, the actual value for the broadening does not play a major role for the results obtained.

From the rates of Fig. 5.1 we also see that Andreev tunneling is acti-

Figure 5.2. Andreev tunneling in a NIS junction. The black dots show measured subgap current of an NIS junction. The data is taken from Fig. 4.2. The solid red line is a calculated curve with Andreev tunneling producing the linear slope as in environmental activation.

vated as soon as $\delta E_i^{\pm\pm} > 0$. The superconductor gap Δ does not appear in this condition at all reflecting the fact that no pair breaking is involved in the process. Once the threshold condition is satisfied, the tunneling rate grows linearly in $\delta E_i^{\pm\pm}$ giving rise to linear current - voltage relation. With $\delta E_i^{\pm\pm} < 0$, tunneling is exponentially suppressed and the rates are set by thermal activation. All these features are similar to single-electron tunneling in a fully normal metallic tunnel junction, i.e. Eq. (2.23) with $\Delta = 0$. Such a linear leakage current can be present also in an NIS junction ($\Delta \neq 0$) because of environmentally activated tunneling as in Sect. 4 ($\sigma \neq 0$ in Eq. (4.22)). Therefore one needs to pay special attention to distinguish different tunneling processes producing similar features. This will be the topic of the next section. First we demonstrate that indeed, Andreev tunneling leads to similar features for voltage biased NIS junctions as the environmentally assisted tunneling. Then we show that by utilizing charging energy costs, one can clearly distinguish these two effects.

5.2 Measuring Andreev tunneling: subgap current

The most obvious way to probe experimentally the Andreev tunneling in NIS junctions is to investigate the tunneling current in the subgap region, $|eV_b| < \Delta$. The simplest experiment is to measure a single voltage biased junction [5, 70] as was described in Sections. 2.2.2 and 4. We actually take the data of Fig. 4.2 which was interpreted there as envi-

ronmentally activated single-electron tunneling and show that, with free parameters, it can be fitted as well with the expressions governing Andreev tunneling. Thus the interpretation of the subgap currents of a NIS junction is not necessarily unambiguous. In Fig. 5.2 we replicate the experimental data obtained with the junction on top of the ground plane as dark blue dots. In addition, we show simulations where Andreev and single-electron tunneling without environmental activation is considered as red line. The current is obtained as $I = e(\Gamma_{\mathrm{N \to S}}(eV_b) + 2\Gamma_{\mathrm{N \to S}}^{\mathrm{AR}}(2eV_b) - \Gamma_{\mathrm{S \to N}}(-eV_b) - 2\Gamma_{\mathrm{S \to N}}^{\mathrm{AR}}(-2eV_b))$. The linear part of the calculated current at $-0.7\,\Delta < eV_b < 0.7\,\Delta$ is caused solely by Andreev tunneling. The steep increase at $eV_b \approx \Delta$ is because of thermally activated single-electron tunneling.

One approach to resolve the origin of the observed current is to consider the magnitude of the slope and find out whether it is consistent with Andreev tunneling. At low energies ϵ, we obtain $a(\epsilon) = \pi/2$ from Eq. (5.3). In addition, taking $E_c = 0$ and $T_N = 0$, we obtain from Eq. (5.2) for small bias voltages

$$\Gamma_{\mathrm{N \to S}}^{\mathrm{AR}} = \frac{1}{8\mathcal{N}} \frac{R_K}{eR_T^2} V_b, \tag{5.5}$$

which is consistent with the BTK calculations [3]. Equation (5.5) yields the ratio of the conductances in the subgap and asymptotic bias regimes as

$$\sigma^{\mathrm{AR}} = \frac{2e\Gamma_{\mathrm{N \to S}}^{\mathrm{AR}}}{V_b} R_T = \frac{1}{4\mathcal{N}} \frac{R_K}{R_T}, \tag{5.6}$$

which shows that the ratio is set by $R_K A_{\mathrm{ch}}/(R_T A)$. The area of the junction used in the measurement of Fig. 5.2 is $A = 80\,\mathrm{nm} \times 110\,\mathrm{nm}$ based on a scanning electron micrograph, and the tunnel resistance $R_T = 760\,\mathrm{k\Omega}$ is obtained from the asymptotic slope of the current-voltage graph. For getting the subgap slope of Fig. 5.2 correct, we need to take $A_{\mathrm{ch}} = 30\,\mathrm{nm}^2$. This value is the same as the values obtained in the experiments below indicating that Andreev tunneling causes the leakage in this case. The junctions considered in this thesis are relatively small, $A \lesssim (100\,\mathrm{nm})^2$, and opaque, $R_T \gtrsim 100\,\mathrm{k\Omega}$. For such junctions the Andreev tunneling is ballistic and given by Eq. (5.2). For larger, more transparent junctions the Andreev tunneling becomes diffusive producing a zero-bias anomaly in the measurement which helps to identify Andreev tunneling [5, 6, 70]. Still the measured current typically has an extra linear subgap part.

The considerations above apply to a voltage biased NIS junction. In Publication IV the influence of the charging energy to Andreev tunneling was considered. From Eq. (5.4) we see that the Andreev threshold $\delta E_i^{\pm\pm} = 0$
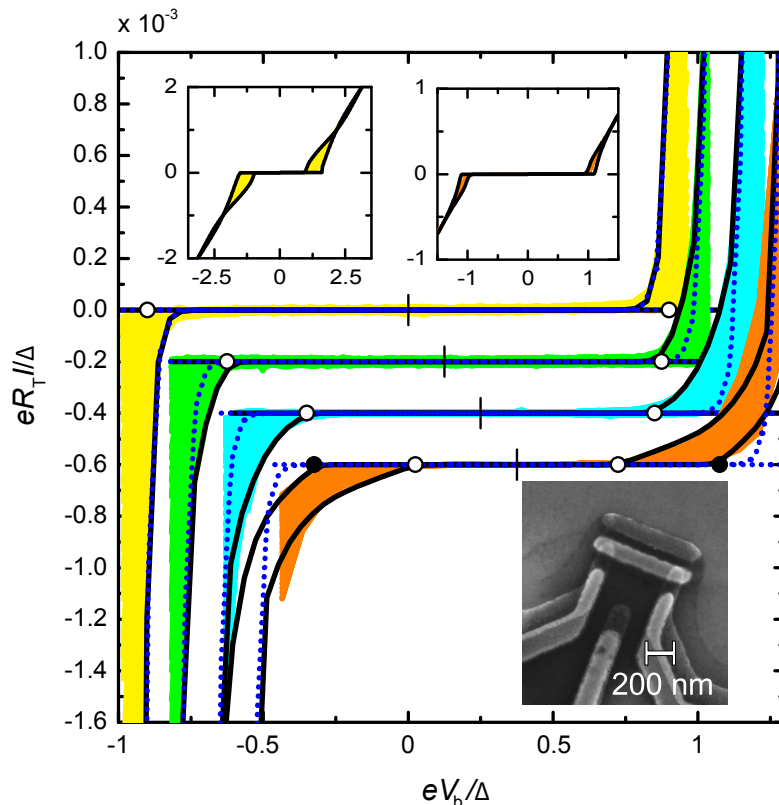
Figure 5.3. Andreev tunneling in SINIS transistors. Colored regions show measured subgap current for devices with charging energies $E_c/k_B = 2.3, 1.9, 1.5$, and 0.86 K from top (yellow) to bottom (orange) at all gate offset values (the "colored" areas). The insets depict the larger scale measurements for samples with the highest and lowest charging energies and a scanning electron micrograph of one of the measured SETs. Solid black lines are theoretical curves at degeneracy (maximal current) and in Coulomb blockade (minimal current) with Andreev tunneling taken into account. Dotted blue lines present fits excluding Andreev processes. Tunneling resistances of the samples were $R_T = 129, 78, 55$, and 31 kΩ in order of decreasing E_c, and superconducting gap $\Delta = 216$ μeV for all of them. Open (solid) circles present the expected thresholds $|eV_b| = E_c$ and $2E_c$ for Andreev tunneling at degeneracy and in Coulomb blockade, respectively. This figure is adapted from Publication IV.

is exceeded if the bias per junction satisfies $|eV_b| > E_c$ for degeneracy, $n_g = 1/2$, and $|eV_b| > 2E_c$ for Coulomb blockade, $n_g = 0$. Here we have again taken $V_b = V_1 = -V_2$ for the SET. The degeneracy case minimizes the required bias voltage. Therefore we expect that no Andreev current will flow below this voltage and above it Andreev tunneling is activated for a certain gate offset range around $n_g = 1/2$. Likewise, Coulomb blockade maximizes the required bias and hence we expect Andreev current to flow at all values of n_g starting from $|eV_b| = 2E_c$. These voltage thresholds are indeed the features that are observed in SINIS single-electron transistors. In Fig. 5.3 we present data for four devices. The charging energy is ranging from $E_c = 70$ μeV to $E_c = 200$ μeV. There is indeed no subgap current at $|eV_b| < E_c$, whereas at higher voltage values the current is non-

vanishing. The maximum value of the current is obtained with $n_g = 1/2$ and it increases linearly for higher biases V_b. The onsets at $eV_b = \pm E_c$ are clear fingerprints of two electrons being involved in the transport. Furthermore, the linear increase after the threshold is in agreement with the Andreev tunneling rates discussed in Sect. 5.1.

The Andreev tunneling rates can be incorporated in the master equation (3.7) by adding terms $\Gamma_{n-2,n}P(n-2)$ and $\Gamma_{n+2,n}P(n+2)$ which correspond to tunneling of two electrons into or out from the island. The rates $\Gamma_{n\pm2,n}$ are set by $\Gamma_{\mathrm{N\to S}}^{\mathrm{AR}}$ and $\Gamma_{\mathrm{S\to N}}^{\mathrm{AR}}$. For calculating the current with Eq. (3.8), we add these rates multiplied by a factor two since two electrons tunnel in each event. The full equations are given in Publication V. We show in Fig. 5.3 calculations including Andreev tunneling at $n_g = 1/2$ and $n_g = 0$ as black lines. For reference, simulations but excluding Andreev tunneling are given as dotted blue lines. For low charging energy devices, the features of the excess current are captured well by including Andreev tunneling rates. At higher E_c, the leakage in the gap vanishes gradually and only thermally activated single-electron tunneling persists. The slope at which the current rises above the threshold bias $|eV_b| = E_c$ is set by the magnitude of Andreev tunneling. It allows us to determine the size of a single conduction channel as $A_{\mathrm{ch}} = 30 \ \mathrm{nm}^2$.

5.3 Real-time detection of Andreev tunneling events

An alternative approach for the detection of Andreev tunneling is to utilize electron counting techniques which was done in Publication IV. In such a setup, a charge sensitive electrometer is used for monitoring the number of electrons on a metallic island. As the number changes because of tunneling, we see a jump in the detector signal thus allowing one to detect the tunneling event. A typical device used as an electrometer is a single-electron transistor, but also quantum point contacts can be utilized for charge detection [79–81]. In our case we can use a SINIS transistor since that can be fabricated in the same process as the studied systems. For a detailed discussion about the operation, sensitivity and bandwidth of such electrometers, see Publication VIII and Ref. [82].

The electron counting provides us a major advantage as compared to the direct current measurement. With it, we are able to determine directly the number of electrons passed in each tunneling event. This is based on the fact that the change in detector signal is ideally proportional to
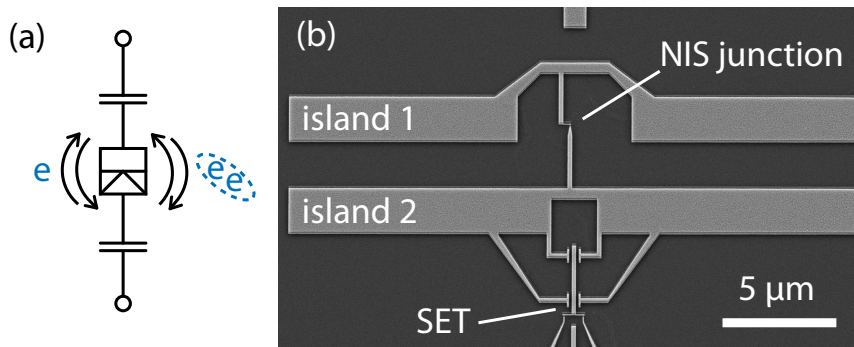
Figure 5.4. Andreev tunneling in a single electron box. (a), An isolated single-electron box (SEB) consists of two islands. One is superconducting and the other normal metallic. Single-electron and Andreev tunneling is possible in the NIS tunnel junction connecting the two islands. An SET electrometer and a gate offset voltage can be coupled to either of the islands capacitively. (b), Scanning electron micrograph of an isolated SEB. The two islands are 25 μm long horizontal bars shaped in the middle to accomodate the connecting NIS junction and coupling to the electrometer shown at the bottom.

the number of electrons leaving or entering the island. This advantage is obtained by utilizing the charging effect of a small island: what we detect is a change in the electrostatic potential of the island as electrons tunnel.

In Fig. 5.4 (a) we show schematically the system we study. It is an isolated single electron box (SEB) consisting of a normal metallic and superconducting island. They are connected by an NIS junction allowing single-electron and two-electron Andreev tunneling to take place. To detect the tunneling events, the two islands are capacitively coupled to other parts. Typically one of the islands is coupled to the electrometer, allowing one to monitor the number of electrons on that island, and the other one to a gate electrode, which allows one to tune the offset charge n_g of the SEB. An actual device is shown in panel (b).

The SINIS SET which is used as the electrometer is biased slightly above the threshold condition, $eV_b \gtrsim \Delta$, where the current depends strongly on its offset charge $n_{g,\text{det}}$. It is tuned such that the current is half way between its maximum and minimum values. This way the dynamical range for the detection is optimized but typically the sensitivity set by $dI/dn_{g,\text{det}}$ is also close to its maximum value around this point. With SET electrometers, subelectron sensitivity of the order of 10^{-5} e/Hz$^{1/2}$ is obtainable [83–86]. Once the detector is tuned to the operation point, time traces of the detector current are recorded under different biasing conditions of the SEB. When the SEB offset charge n_g is changed, the offset charge $n_{g,\text{det}}$ of the detector must be compensated to keep it at the operation point. This is due to unavoidable cross-couplings. The compensation
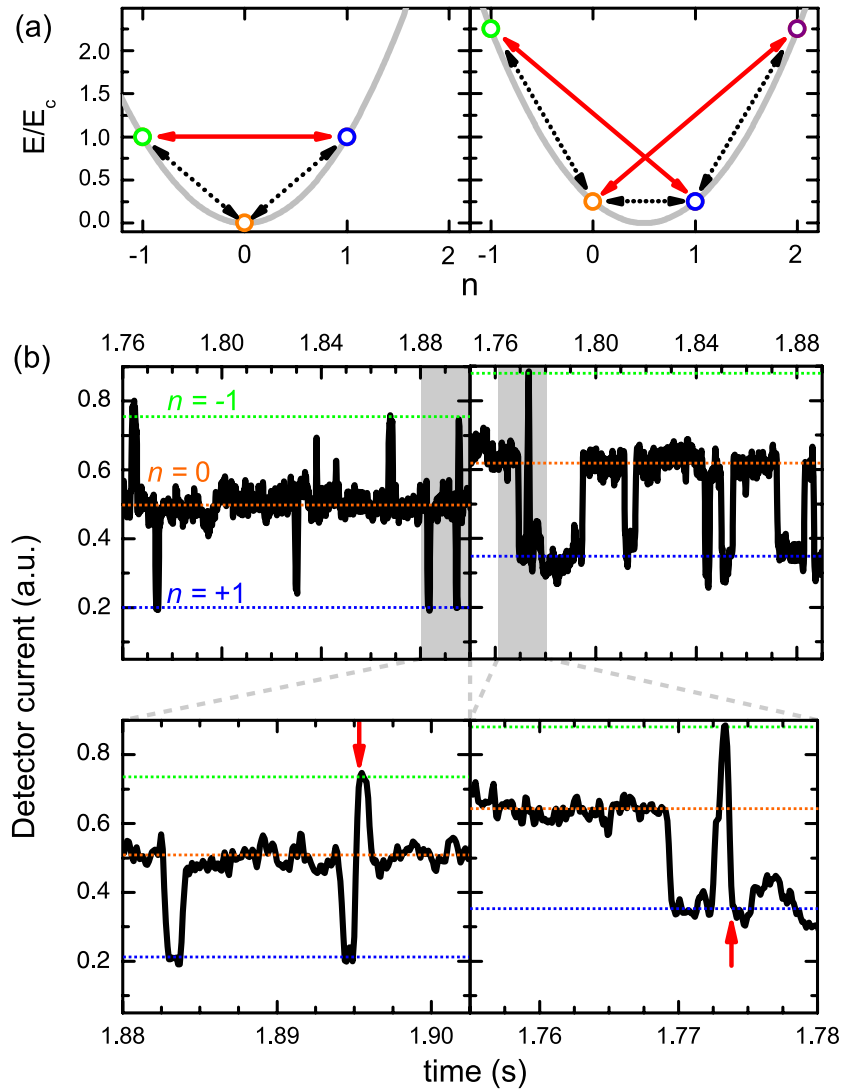
Figure 5.5. SEB time traces. Charging energy E for n excess electrons on the island. The left panel is for Coulomb blockade, $n_g = 0$, and the right one for degeneracy, $n_g = 1/2$. (b), Time traces at Coulomb blockade (left panels) and at degeneracy (right panel). Short time intervals are zoomed in the panels at the bottom and they show possible two-electron tunneling events. Figure adapted from Publication IV.

is however straightforward to do: Only a linear component needs to be substracted from the detector gate offset. The compensation coefficient is found by trial and error.

When the offset of the SEB is tuned, two extreme cases are found: Coulomb blockade and degeneracy. The energy E for n excess electrons on one of the islands as well as typical timetraces recorded at these extreme cases are shown in Fig. 5.5. In Coulomb blockade, one of the charge states has the lowest energy and the states around it are equally high in energy. In the time traces, we see that the box stays most of the time at the lowest energy state $n = 0$ and equally likely switches to either $n = +1$ or $n = -1$. When the system enters one of the higher states we see that
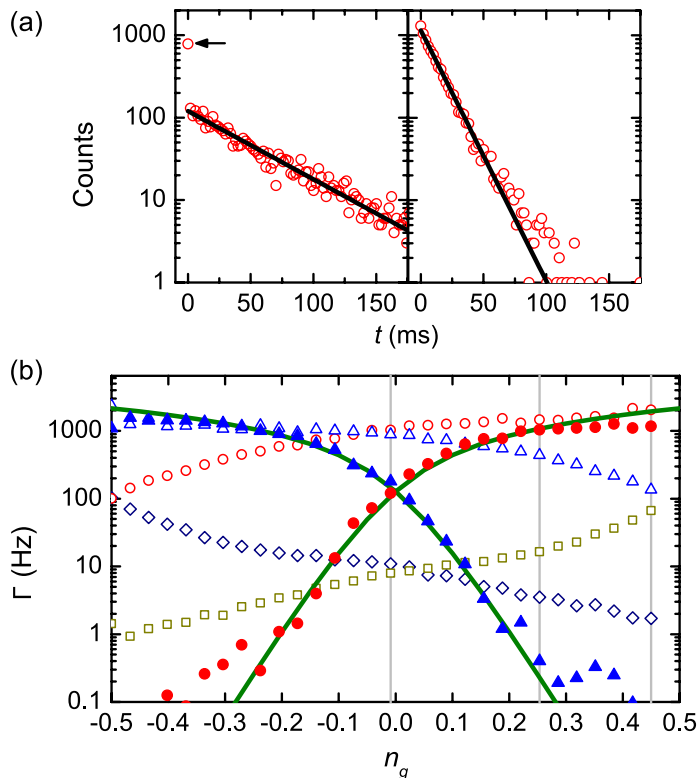
Figure 5.6. Waiting time histograms and tunneling rates in the SEB of Fig. 5.4.
(a), Waiting time of the charge state n with the lowest energy E in Coulomb blockade (left) and at degeneracy (right). (b), Tunneling rates for single-electron processes (open symbols) and Andreev tunneling (filled symbols) for the two directions. The two single-electron processes with lower rates are tunneling from lower energy state to higher ones and the two processes with higher rates are for the reverse processes. The results are obtained at the base temperature of $60\,\mathrm{mK}$ of our cryostat. Figure adapted from Publication IV

Andreev tunneling events shown as red arrows in panel (a) do not involve energy cost and become therefore probable. We indeed see on the blow up that there are fast transitions between $n = \pm 1$ without intermediate halt at $n = 0$.

At degeneracy, which is the other extreme, two charge states represent the degenerate minimum energy states. The time spent in these two states is equal. Entering other states requires in this case at least twice as much energy as in Coulomb blockade and therefore it is more unlikely. Since Andreev tunneling from the lower lying states involves also a large energy cost, it is not as probable as in Coulomb blockade.

Because the SET electrometer has a finite bandwidth, there is one issue which needs to be analysed in order to confirm the detection of two-electron events. The possible two-electron tunneling events pointed by red arrows in Fig. 5.5 could in principle be just two single-electron events occuring subsequently so quickly that the detector cannot resolve them

separately. This possibility is ruled out by assuming only single-electron events to occur. By considering the waiting time spent in the state $n = 0$ before a tunneling event occurs, we get the distributions shown in Fig. 5.6 (a). The fast transients indicated by the red arrows in Fig. 5.5 contribute to short waiting times t. If those would be originating fully from single-electron tunneling, the waiting time distribution would be exponential (Poisson process). However, we see that this is not the case in Coulomb blockade, where the data point at the smallest t is almost an order of magnitude higher than the exponential distribution at larger values. Therefore these events are dominantly of other origin suggesting that they are true two-electron events.

For consolidating that the two-electron processes are indeed Andreev tunneling, we next consider the tunneling rates for all processes. For obtaining the rates, firstly, we need to distinguish between one- and two-electron processes. We interpret transitions with charge number changing by $\Delta n = \pm 2$ and occuring within 0.4 ms as two-electron tunneling and all other events as one-electron tunneling. The time window here was chosen to be approximately equal to the risetime of the detector so that essentially all excess events in the histograms of Fig. 5.6 (a) were captured. In order to calculate the tunneling rates, we use the following arguments: The average waiting time for a given charge number n is $\langle t \rangle = 1/\Gamma_\Sigma$, where $\Gamma_\Sigma = \sum_j \Gamma_j$ is the sum of all tunneling rates Γ_j out from this state. The probability that the tunneling event that took place corresponds to a process with rate Γ_j is $P(\Gamma_j) = \Gamma_j/\Gamma_\Sigma$. Hence we may write the number of events corresponding to this process as $N_j = N_\Sigma P(\Gamma_j) = N_\Sigma \langle t \rangle \Gamma_j$, where $N_\Sigma = \sum_j N_j$ is the sum of all events out from this particular state. We find that

$$\Gamma_j = \frac{N_j}{N_\Sigma \langle t \rangle},\tag{5.7}$$

where the denominator, $N_\Sigma \langle t \rangle$, is the total time spent in the initial charge state. Therefore counting the number of occurred events for a given process and dividing by the time spent in the inital state yields the tunneling rate for that process. In Fig. 5.6 (b) the tunneling rates for all processes in our system are plotted as a function of the gate offset charge n_g of the SEB. The solid green lines are theoretical calculations of Eq. (5.2) for Andreev tunneling, where a value $A_{\mathrm{ch}} = 30$ nm^2 was used. This value defining the magnitude of Andreev tunneling is in agreement with the one obtained in Sect. 5.2 from direct current measurements. Furthermore, we observe that the Andreev tunneling rates obtained experimentally have the cor-

rect functional dependency on n_g as indicated by the solid green lines.

In this section, we have seen that the Andreev tunneling is activated in Coulomb blockade and suppressed at degeneracy. In Sect. 5.2, see Fig. 5.3, we however saw that Andreev tunneling is stronger at degeneracy than in Coulomb blockade when an SET is biased. At first these observations seem contradictory. The results of the present section assumed that single-electron processes excite the system to states $n = \pm 1$ in Coulomb blockade allowing for the Andreev process. If this is not present, the Andreev tunneling would have to start from state $n = 0$ and the energy cost for tunneling would be higher than at degeneracy. This is the case presented in Sect. 5.2 leading to larger Andreev current at degeneracy thus resolving the contradiction. Having just two coexisting different kinds of tunneling processes leads to relatively rich characteristics and the manifestation of various features depends on the relative rates of the two tunneling processes.

5.4   Influence of Andreev tunneling on SINIS turnstile

Above we discussed Andreev tunneling under static biases V_b and n_g. Now we consider the case studied in Publication V where n_g is periodically driven and quantized current plateaus form in the SINIS turnstile. Andreev tunneling leads to pumping errors [49]. Occasionally, an Andreev tunneling event happens instead of single-electron tunneling. Two electrons are transported in this case and the current is enhanced.

An illustrative way to consider the competition between single-electron and Andreev tunneling is to draw stability diagrams shown in Fig. 5.7 (a) and (b) for both of the processes. The thresholds are obtained by requiring $\delta E^{\pm} = \Delta$ in Eq. (3.6) for single-electron processes and $\delta E^{\pm\pm} = 0$ in Eq. (5.4) for Andreev processes. We observe that the thresholds run in parallel and form diamonds of similar shape. If $E_c < \Delta$, the diamond set by Andreev tunneling is smaller than the single-electron one and Andreev tunneling becomes activated first. For $E_c > \Delta$, the situation is reversed and single-electron tunneling is activated first. This is reflected in the current quantization of the devices. In panels (c) and (d) we show the first pumping plateau for the low and high charging energy device. We see that the current for the low E_c device is higher than ef whereas for the high E_c device the current at the plateau is significantly closer to ef. The measured data points and the calculated curves match well together. The
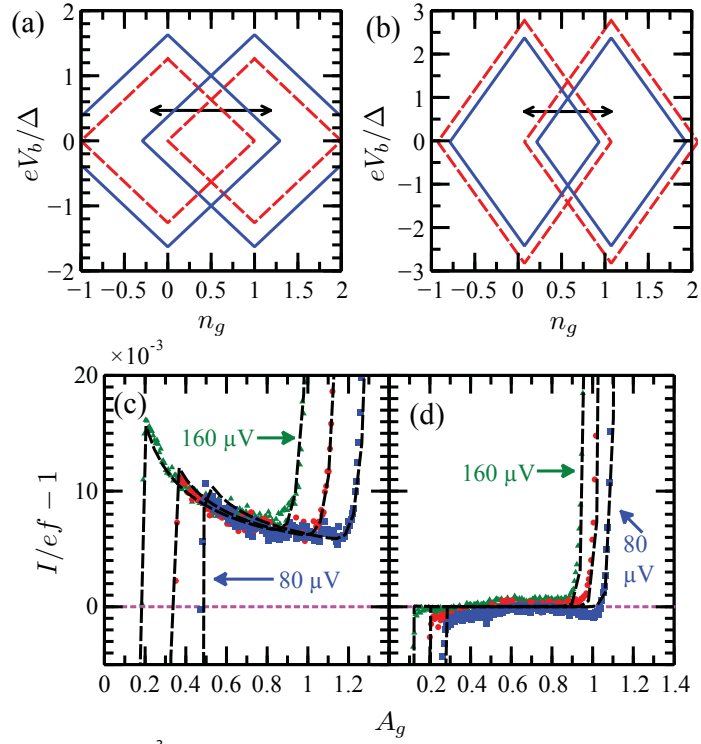
Figure 5.7. Andreev tunneling in SINIS turnstiles. Stability diamonds for single-electron tunneling (solid blue lines) and Andreev tunneling (dotted red lines) for $E_c = 0.63\Delta$ in panel (a) and $E_c = 1.4\Delta$ in panel (b). The first quantized current plateau at $f = 10$ MHz for $E_c = 0.63\Delta$ in panel (c) and $E_c = 1.4\Delta$ in panel (d). The points are experimental data with the bias voltage per junction of $V_b = 80, 120$ and 160 μV and dashed black lines are numerically calculated curves where Andreev tunneling is taken into account. A_g is the amplitude of the gate offset drive. The error of the current measurement is smaller than 1 % and limited by the uncertainty of the gain of the current preamplifier. A 10^{-3} level correction is made to the gain in order to match the absolute values of the current for the simulated and measured currents. Figure adapted from Publication V.

fast increase of current is caused by exceeding the single-electron tunneling thresholds. Ideally the current should take the value ef between the rising intervals. However, because of Andreev tunneling this does not happen for the low E_c device. The deviation of the value of the current on the plateau from ef is proportional to the magnitude of Andreev tunneling and hence to A_{ch}. For the simulations we have used $A_{\mathrm{ch}} = 30$ nm^2, again in quantitative agreement with findings in previous chapters.

For the high E_c device, the numerical calculations are insensitive to Andreev tunneling. This is because for $E_c > \Delta$, Andreev tunneling is energetically unfavored as compared to the single-electron process: it costs more energy to charge the island with two electrons than to break a Cooper pair. Hence, utilizing a high E_c device leads to better current quantization free of Andreev tunneling. In practice, it is considered to be sufficient to have $E_c \gtrsim 2\Delta$. In this case, the Andreev tunneling thresh-

olds at thermally optimal bias, $eV_b \approx \Delta/2$, are at larger n_g than the back-tunneling thresholds and do not anymore limit the device performance [49, 53].

5.5 Full Counting Statistics (FCS) of Andreev Events

In Sects. 3.2 and 5.2, a master equation was utilized to calculate single-electron and two-electron Andreev tunneling on a small metallic island. As a result, we were able to describe how average current depends on various quantities such as externally controllable bias and gate voltages. Although the average quantities reveal many features of the studied system, they typically cannot provide direct information about fluctuations and noise [87] which have non trivial features in superconducting systems. For example the shot-noise is doubled in Andreev processes compared to single-electron transport [88–90] and it results in positive cross-correlations in Cooper pair splitters [77, 91]. In this section we discuss how quantities beyond the average values can be treated for the tunnel junctions with the so-called full counting statistics (FCS) techniques and how the FCS can be straigthforwardly accessed experimentally with the electron counting techniques [92–96]. We first review the essential parts of FCS based on a master equation approach [97–100] and then consider the experiment of Publication XI where Andreev tunneling occurs in avalanches and results in super-poissonian statistics.

5.5.1 Master equation approach to FCS

We consider probability $p_m(n,t)$ of having m excess electrons on the island while n electrons have been transported in total at time t. Taking into account single-electron and two-electron tunneling the master equation reads

$$
\begin{aligned}
\tfrac{d}{dt} p_m(n) &= -\Gamma_{\Sigma,m} p_m(n) + \Gamma_{m-2}^{++} p_{m-2}(n-2) + \Gamma_{m-1}^{+} p_{m-1}(n-1) \\
&\quad + \Gamma_{m+1}^{-} p_{m+1}(n \pm 1) + \Gamma_{m+2}^{--} p_{m+2}(n \pm 2),
\end{aligned}
\tag{5.8}
$$

where we dropped the time variable, which is the same for all terms and $\Gamma_m^{\pm}$ is single-electron tunneling rate into $(+)$ or out from $(-)$ the island with initially m electrons and $\Gamma_m^{\pm\pm}$ the two-electron rate into $(++)$ or out from $(--)$ the island with initially m electrons [97, 100]. $\Gamma_{\Sigma,m} = \Gamma_m^{+} + \Gamma_m^{-} + \Gamma_m^{++} + \Gamma_m^{--}$. The choice of $+$ and $-$ in the last two terms of the first row determines whether we consider the total number of tunnel-

ing events irrespective of the direction $(-)$ or the net number of electrons tunneling in one direction, substracting the tunneling to the opposing direction. Also counting the tunneling events for example on only one of the SET junctions is straighforward to do by using terms where n remains unchanged for the other junction. This is important for example when the current noise of a SET is considered.

To get the statistics of n, we are interested in the moment generating function

$$M(\chi) = <e^{\chi n}> = \sum_n e^{\chi n} P(n,t), \tag{5.9}$$

where $P(n,t) = \sum_m p_m(n,t)$ is the probability of having n events at time t. Once $M(\chi)$ is known, the moments are obtained simply by differentiation with respect to χ. Also the distribution of the events $P(n,t)$ is obtained by a Fourier transformation as we can see from the right hand side of Eq. (5.9). Now we write $z = e^{\chi}$ and

$$M(z) = \sum_m g_m(z,t), \tag{5.10}$$

where $g_m(z,t) = \sum_n z^n p_m(n,t)$. With Eq. (5.8) we obtain a master equation for g_m:

$$\begin{aligned}\frac{d}{dt}g_m &= -\Gamma_{\Sigma,m}g_m + \Gamma_{m-2}^{++}z^2 g_{m-2} + \Gamma_{m-1}^{+}z g_{m-1} \\ &\quad + \Gamma_{m+1}^{-}z g_{m+1} + \Gamma_{m+2}^{--}z^2 g_{m+2}.\end{aligned} \tag{5.11}$$

Here we again dropped arguments z and t which are the same for all terms and we count the number of all events. We now consider vector $\bar{g}$ whose elements are g_m. Equation (5.11) can be then written as

$$\frac{d}{dt}\bar{g}(z,t) = \bar{M}(z)\bar{g}(z,t), \tag{5.12}$$

where

$$\bar{M}(z) = \begin{bmatrix} \ddots & & & & & \\ z^2\Gamma_{m-2}^{++} & z\Gamma_{m-1}^{+} & -\Gamma_{\Sigma,m} & z\Gamma_{m+1}^{-} & z^2\Gamma_{m+2}^{--} & \\ & z^2\Gamma_{m-1}^{++} & z\Gamma_{m}^{+} & -\Gamma_{\Sigma,m+1} & z\Gamma_{m+2}^{-} & z^2\Gamma_{m+3}^{--} \\ & & & \ddots & & \end{bmatrix}. \tag{5.13}$$

Equation (5.12) can be solved formally to get $\bar{g}(z,t) = e^{\bar{M}(z)t}\bar{g}(z,0)$, where $\bar{g}(z,0)$ is the configuration at the beginning of the counting. The quantity $\bar{g}(z,0)$ is taken such that only the states with $n = 0$ have non-zero probability and their population is given by solving the steady state $\frac{d}{dt}\bar{g}(z = 1,t) = 0$.[1] Having $g_m(z,t)$, we obtain the moment generating function with

---

[1] By taking $z = 1$ in Eq. (5.12), it reduces to the standard master equation (3.7).
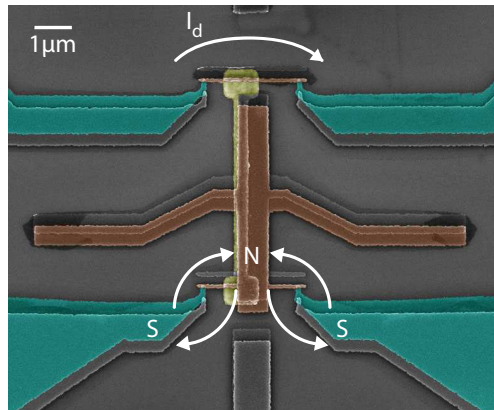
Figure 5.8. The structure for detecting Andreev avalanches. Two SINIS transistors with the islands coupled capacitively to each other with a metallic strip (yellow). The transistor on top with higher E_c is used as an electrometer. The number of excess electrons N on the other transistor island is read via the current I_d flowing through it. Figure adapted from Publication XI.

Eq. (5.12) and we can readily use it to obtain any statistics we are interested in.

5.5.2 FCS of Andreev tunneling

The electron counting techniques discussed in Sect. 5.3 allow one readily to perform FCS experiments. The structure which was used in Publication XI is shown in Fig. 5.8. Instead of measuring the number of excess electrons N in a isolated box, we measure them in an island of a SINIS turnstile. These two setups behave identically when the transistor is kept at zero bias as we did in the experiments below. However the transistor structure allows us to measure transport characteristics and extract parameter values $R_T = 490$ kΩ, $\Delta = 210$ μeV and $E_c = 40$ μeV, as described in Sect. 3.2. The drawback is that the rates will be twice as high as compared to the isolated box, trivially because there are two junctions contributing to tunneling.

First we tune the offset charge to degeneracy $n_g = 1/2$. The charge states $N = 0$ and $N = 1$ are the lowest lying ones with equal energy as shown in Fig. 5.9 (a), and results in a time trace where single-electron tunneling takes place between the two states as shown in panel (b). Now we can obtain experimentally the FCS distribution. We recorded 3 s time traces and chopped them in bins of length t. By counting the number of events in each time bin, we build the probability histogram $p(n, t)$ for observing n tunneling events in time t shown in Fig. 5.9 (c).

For predicting the experimental distribution, we take Eq. (5.12) with the
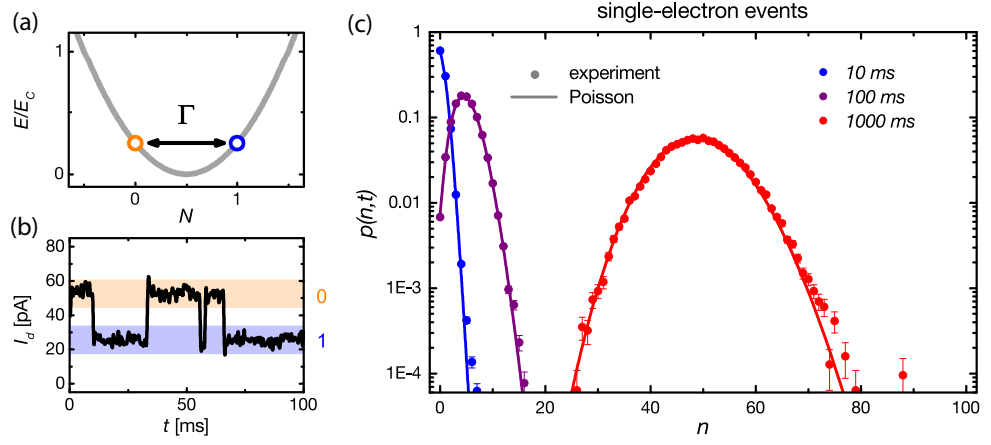
Figure 5.9. Statistics of single-electron tunneling. (a), Charge degeneracy ($n_g = 0.5$) where only single-electron tunneling is active as shown by the time trace of the detector current in panel (b). The energy parabola is obtained from Eq. (3.4). (c), Probability $p(n, t)$ for observing n single-electron events in time window $t = 10, 100$ and 1000 ms. Solid lines are Poisson distributions. Figure adapted from Publication XI.

two states $N = 0, 1$ as

$$\frac{d}{dt}\begin{bmatrix} g_0(z,t) \\ g_1(z,t) \end{bmatrix} = \begin{bmatrix} -\Gamma & z\Gamma \\ z\Gamma & -\Gamma \end{bmatrix}\begin{bmatrix} g_0(z,t) \\ g_1(z,t) \end{bmatrix}, \qquad (5.14)$$

where $\Gamma = 49$ Hz is the degeneracy tunneling rate, determined from the time traces by evaluating the average waiting time before a tunneling event occurs. Equation (5.14) can be straightforwardly solved to yield $M(z) = g_0 + g_1 = e^{(z-1)\Gamma t}$, which is the moment generating function of a Poisson distribution with mean $< n >= \Gamma t$. Therefore $p(n, t) = \frac{1}{2\pi}\int_0^{2\pi} d\chi\ e^{-in\chi}M(e^{i\chi}) = \frac{(\Gamma t)^n}{n!}e^{-\Gamma t}$, which is presented as solid lines in Fig. 5.9 (c). We observe that the experimental statistics follow the Poisson distribution as expected.

In Fig. 5.10 the same experiment is repeated in Coulomb blockade, $n_g = 0$. In this case the energy diagram of panel (a) has $N = 0$ as the most probable state and the tunneling to $N = \pm 1$ involves an energy cost. A typical time trace is shown in panel (b). Most of the time the box is in the charge state $N = 0$. Then a single-electron event moves the system to either of the states $N = \pm 1$. In these states two-electron Andreev tunneling with rate Γ_A is energetically neutral as shown by the red horizontal line of panel (a). Because of the pair breaking energy cost Δ, the single-electron rate Γ_d down to $N = 0$ is exponentially suppressed in temperature as discussed in Sect. 2.2.2. Therefore it is possible to have $\Gamma_A > \Gamma_d$. In this case, multiple Andreev tunneling events take place before the system relaxes back to $N = 0$. Such a set of parameters results in bunching of the tunneling events with a typical avalanche shown in panel (b).
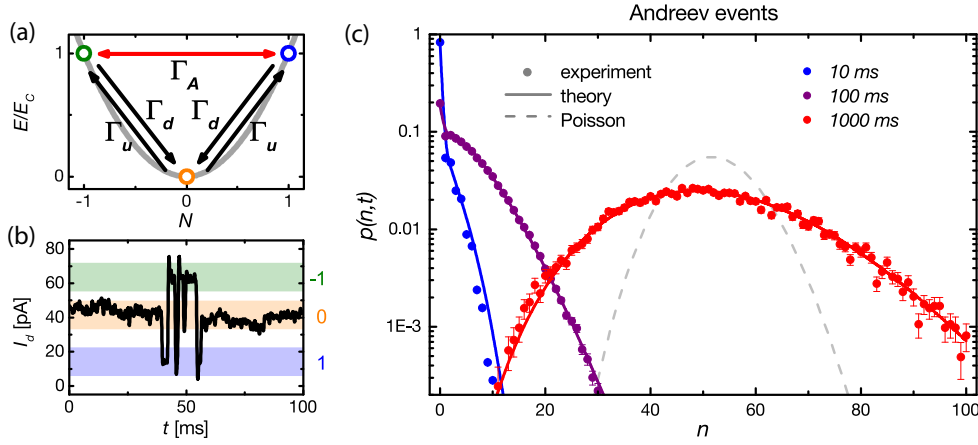
Figure 5.10. Statistics of two-electron Andreev tunneling. (a), A schematic on charging energy costs and tunneling processes in Coulomb blockade ($n_g = 0$). Charge state $N = 0$ is preferred as shown by the measured time trace in panel (b). (c), Probability $p(n, t)$ for observing n single-electron events in time window $t = 10, 100$ and 1000 ms. Solid lines are theoretical predictions based on Eq. (5.15). Figure adapted from Publication XI.

The statistics of Andreev tunneling shown in Fig. 5.10 (c), demonstrate that the distributions are broader than the Poisson distribution, reflecting the fact that the bunching makes the signal more noisy. To corroborate this, we again take Eq. (5.12) but now counting only the number of Andreev events. Since the states $N = \pm 1$ are identical, we simplify the problem by summing them to $g_A = g_1 + g_{-1}$. We then obtain

$$\frac{d}{dt} \begin{bmatrix} g_A(z,t) \\ g_0(z,t) \end{bmatrix} = \begin{bmatrix} \Gamma_A(z-1) - \Gamma_d & 2\Gamma_u \\ \Gamma_d & -2\Gamma_u \end{bmatrix} \begin{bmatrix} g_A(z,t) \\ g_0(z,t) \end{bmatrix}. \tag{5.15}$$

Solving Eq. (5.15) and taking the Fourier transform, leads to the theoretical lines of Fig. 5.10 (c). The tunneling rates $\Gamma_u = 12$ Hz, $\Gamma_d = 250$ Hz and $\Gamma_A = 610$ Hz were estimated by counting the number of occured events and dividing by the time spent in the initial state as in Sect. 5.3. Note that the broader distribution obtained here is not because of the Andreev process carrying two electrons unlike in Ref. [90]. Since we count the number of *pairs* this effect does not show up in the statistics. The distribution is broader solely because of the bunching of the tunneling events. If one would count the number of electrons instead, it would lead to an additional factor of two in the variance as in Ref. [90].

In Publication XI it was furthermore shown by expanding the cumulant generating function in by the lowest order in Γ_u that the FCS in this case can be approximated as a sum of independent Poisson processes that generate avalances of m Andreev events with a probability

$$q(m) = \frac{\Gamma_d}{\Gamma_A + \Gamma_d} \left(\frac{\Gamma_A}{\Gamma_A + \Gamma_d} \right)^m, \tag{5.16}$$

where $\Gamma_A/(\Gamma_A + \Gamma_d)$ is the probability of having one more Andreev event in state $N = \pm 1$ and $\Gamma_d/(\Gamma_A + \Gamma_d)$ is the probability of having a tunneling event down to $N = 0$ at the end. The distribution $q(m)$ was determined experimentally and good agreement with Eq. (5.16) was found.

6. Quasiparticle excitations in a superconductor

As the temperature T_S of a superconductor is lowered, the thermal excitations in form of unpaired electrons diminish exponentially. This happens since according to Eq. (2.5), all excitations carry energy which is at least Δ. Because of the exponentially small number of carriers, many quantities such as electrical heat conduction and recombination of broken Cooper pairs in a superconductor become also exponentially weak. Having such a strong dependency makes the temperature an inconvenient parameter for quantifying the excitations: a $10\,\%$ change in it may lead to an order of magnitude change in the number of excitations. Therefore one needs to know the ratio $\Delta/k_B T$ very well in order to know even roughly the number of excitations and quantities depending on it.

A more natural parameter for describing excitations in a superconductor at low temperatures is the number of excitations in unit volume, the quasiparticle density n_{qp}. It is a convenient quantity for analysing the properties of a superconductor in the sense that the quantities depending on the excitations follow a power law. For example heat conduction is approximately linear in n_{qp} and electron-phonon recombination rate scales as n_{qp}^2. In Sect. 6.1 we will first formulate the relation between T_S and n_{qp} and consider experimental ways to probe the excitations with NIS junctions. Then we consider the heat conduction along a superconducting line and obtain a diffusion equation for n_{qp}. By injecting quasiparticles with a SINIS turnstile allows us to probe the diffusion and relaxation of the quasiparticles to a normal metallic trap. We also learn that evacuation of the quasiparticle excitations is of paramount importance in order to obtain good current quantization in the turnstile.

Then in Sect. 6.4 we consider electron-phonon interaction in superconducting state. That provides an inherent mechanism for the excitations to relax. We use a small superconducting island connected with NIS junc-

tions to normal metallic leads to probe the relaxation rates. We are able to show that the island is free of quasiparticle excitations for most of the time. Hence we can probe the recombination of quasiparticles down to a single quasiparticle pair. We also see that the island cannot be considered to have a certain temperature T_S but the dynamics of quasiparticles needs to be accounted explicitly. An extended master equation is needed which describes simultaneously the charge and energy flow on the superconducting island.

In Sect. 2.1 we presented the density of states of a superconductor with two branches, one with energy $E < -\Delta$ and one with $E > \Delta$. The excitations of a superconductor consist of either occupied states at $E > \Delta$ (particle like excitations) or vacant states at $E < -\Delta$ (hole excitations). If the excitations are thermal, the number of excitations on the branches are equal. However, if electrons are predominantly injected to $E > \Delta$, the number of excitations in this branch is expected to be higher. Similarly, if electrons are removed from $E < -\Delta$, the hole excitations are more abundant. While the increased number of excitations leads to increased temperature T_S, the difference of excitations in the two branches induces a shift in the chemical potential [1]. In the SINIS turnstile such branch imbalance is likely to occur since electrons are removed from one superconducting lead and injected to another. The possibility for the branch imbalance is discussed in Sect. 6.3. Yet we find that the branch imbalance is negliglible in the turnstile suggesting that the branch relaxation is faster than the quasiparticle injection.

6.1 Probing quasiparticles with NIS junctions

In Sect. 2.2.2 we saw that the temperature of the superconductor, in form of quasiparticle excitations, cannot be probed with a single NIS junction since the rates in the forward and backward direction compensate each other or the rates caused by the excitations are overwhelmed by rates from other mechanisms. In this section we discuss two ways of probing the excitations. The probing can be done either by making an electron counting experiment or by measuring the current - voltage characteristics of a SET structure. These both approches utilize Coulomb charging energy in the same way as was done in Chap. 5 for observing Andreev tunneling. In the first one, it is used for obtaining a measurable signal and in the latter one to rectify the current caused by the quasiparticles.

In the experiments of this thesis, quasiparticle excitations are injected to energies close to the gap edges, $E \approx \Delta$ since we consider the low bias conditions. In this case the excitations can be described in terms of chemical potential shift $\delta\mu$ and elevated temperature T_S [1]. The chemical potential shifts if there is an imbalance in the populations of quasiparticles in the two brances, $E \leq -\Delta$ and $E \geq \Delta$, respectively. Such charge imbalance was observed for the first time in the classic experiment by J. Clarke [42]. There the imbalance was obtained by connecting an NIS and an SIS junction in series. In the SIS junction the current is carried by Cooper pairs which do not influence the quasiparticle excitations whereas electron tunneling in the NIS junction creates excitations only on one of the branches.

The other parameter T_S characterizing the excitations describes the overall number of them. Let us now find the relation between T_S and the quasiparticle density. We assume vanishing charge imbalance. Then the quasiparticle density on one of the branches is

$$n_{\mathrm{qp,b}} = D(E_F) \int_{\Delta}^{\infty} dE n_S(E) f_S(E), \qquad (6.1)$$

where $D(E_F)$ is the normal state density of states at the Fermi level. For aluminum, we have $D(E_F) = 1.45 \times 10^{47}$ J^{-1}m^3, see Ref. [101]. To get the total density of all quasiparticles we have to multiply $n_{\mathrm{qp,b}}$ by two due to the two branches: $n_{\mathrm{qp}} = 2n_{\mathrm{qp,b}}$. On the other hand, if we take Eq. (2.26) with energy gain $-\Delta < \delta E < \Delta$, the tunneling of quasiparticle excitations is the dominant process provided that T_N is low. We then have $1 - f_N(E + \delta E) \approx 1$ for $E > \Delta$. Hence

$$\Gamma_{\mathrm{S}\to\mathrm{N}} = \frac{1}{e^2 R_T} \int_{\Delta}^{\infty} dE n_S(E) f_S(E) = \frac{n_{\mathrm{qp}}}{2e^2 R_T D(E_F)}, \qquad (6.2)$$

which is the value for the tunneling rate at $-\Delta < \delta E < 0$ in Fig. 2.3 (b). Equation (6.2) yields a direct relation between the quasiparticle density and tunneling rate and it can be used to estimate the quasiparticle density as was done in Publications VI, VII and IX. A specific feature of the quasiparticle excitations is that the tunneling rate does not depend on the energy gain δE since the excitations are at high energies. This feature is useful for arguing that the tunneling is originating from quasiparticle excitations.

Now we assume in addition that there are not many excitations present. This low temperature limit, $k_B T \ll \Delta$, is relevant for results presented in this thesis. In this case we have $f_S(E) \approx e^{-E/k_B T_S}$ for $E \geq \Delta$ and Eq. (6.1)
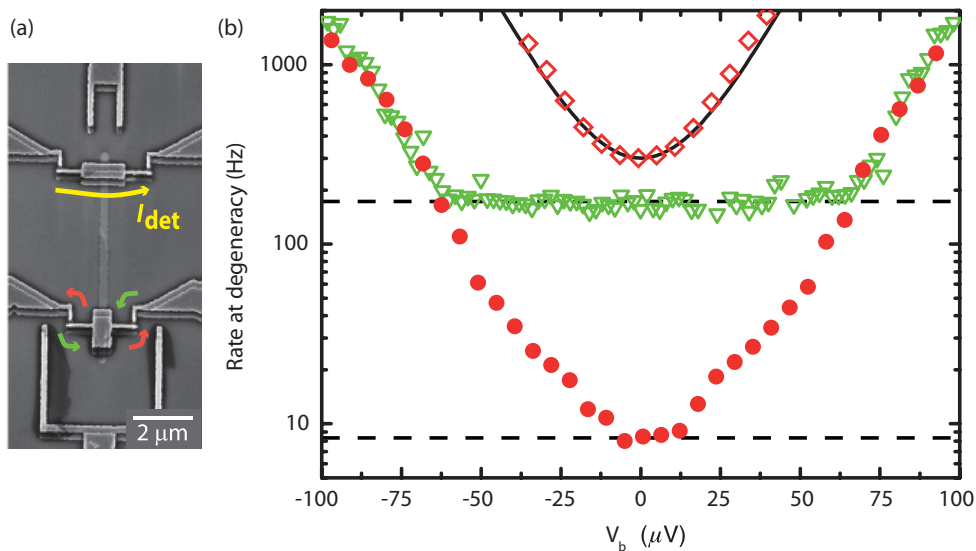
Figure 6.1. Probing quasiparticle excitations by electron counting. (a), Two SETs capacitively coupled as in Fig. 5.8. The upper one monitors the charge state of the lower one. (b), The tunneling rate at degeneracy as a function of bias voltage V_b per junction. Solid red dots are measured at the base temperature of 50 mK. Open diamonds have been measured at 158 mK temperature. Solid black line shows the rates calculated with Eqs. (2.25) and (2.26). Open green triangles are results at the base temperature for a reference sample without normal metallic traps. Quasiparticle relaxation is weaker compared to the case of solid red dots and the tunneling rate is higher at low V_b. For ease of comparison, the tunneling rates are scaled for the latter structure by the ratio of junction conductances $\frac{1/R_{T1,t}+1/R_{T2,t}}{1/R_{T1}+1/R_{T2}}$, where $R_{T1,t} = R_{T2,t} = 1.1$ MΩ are the resistances of the device with direct trap and $R_{T1} = 2.0$ MΩ, $R_{T2} = 25$ MΩ are those for the device without the traps. Figure adapted from Publication VI.

simplifies to

$$n_{\mathrm{qp}} \approx D(E_F)\sqrt{2\pi}\sqrt{k_B T_S \Delta}\, e^{-\frac{\Delta}{k_B T_S}}. \tag{6.3}$$

Equation (6.3) shows that n_{qp} and hence also the tunneling rates caused by quasiparticle excitations are exponentially dependent on temperature as we expected.

Let us now consider the counting experiment of Publication VI for determining the quasiparticle density. In Fig. 6.1 we show the experimental structure. It consists of two SINIS type SETs where the islands are capacitively coupled. One of the SETs is used as an electrometer to read the number of electrons on the other SET island similarly as in Sect. 5.3. The SET, from which the tunneling events are counted, is tuned to charge degeneracy and the tunneling rate shown in Fig. 6.1 (b) is obtained at different bias voltages V_b (per junction). The open green triangles present the tunneling rates at base temperature for a sample without a quasiparticle trap with direct N-S contact. In this case we observe a bias independent rate at small V_b, as we would expect for tunneling by quasiparticle excita-

tions. The measured values $\Gamma_{S1\to N} + \Gamma_{S2\to N} = 50$ Hz, $R_{T1} = 2.0$ MΩ and $R_{T2} = 25$ MΩ, yield $n_S = 0.3$ μm^{-3} (Eq. (6.2)). In Ref. [82] it was estimated that such a density is obtained with pair breaking rate of $2.2 \cdot 10^5$ Hz/μm^3 for the 30 nm thick aluminum film. This value is well inline with the upper limit of $f_{\text{cpb}} = 2$ kHz for the Cooper pair breaking in an island with volume $V = 1.06$ μm $\times$ 145 nm $\times$ 25 nm, discussed in Sect. 6.4.3. These numbers yield an upper limit for the pair breaking rate $f_{\text{cpb}}/V = 5 \cdot 10^5$ Hz/μm^3.

The red dots of Fig. 6.1 (b) show the tunneling rate for a sample having a direct metal-to-metal quasiparticle trap at 10 μm distance from the junction. Now the current caused by quasiparticles is absent as we observe a bias dependent rate. We can however obtain an upper limit for the quasiparticle density by taking the lowest rate $\Gamma_{S1\to N} + \Gamma_{S2\to N} = 8$ Hz and use the tunneling resistances $R_{T1} = R_{T2} = 1.1$ MΩ. With these we obtain $n_{\text{qp}} = 0.03$ μm^{-3}, presenting the lowest reported quasiparticle density observed so far. It is significantly lower than typical values for fully superconducting systems [10–13]. See, however, Ref. [102] where a similar value as ours was subsequently obtained. Efficient trapping of the quasiparticles with normal metallic structures as well as admitting only low frequency signals in the experiment allows us to reach the small quasiparticle densities in the NIS junction based devices.

In addition to the counting techniques, direct current measurents of a SINIS SET allow one to probe the quasiparticles as was done in Publication VII. In order to detect the quasiparticle excitations, the superconducting leads were intentionally designed so that the quasiparticles do not relax to a trap efficiently. A scanning electron micrograph of the device designed for such an experiment is shown in Fig. 6.2 (a). The superconducting leads are 120 nm wide and 20 μm long; beyond the end of the line, a wider section with quasiparticle trapping is reached. Since quasiparticles need to diffuse through the long and narrow line before relaxation, they are easily accumulated close to the junctions. Figure 6.2 (b) presents the measured subgap current of the device. The dark blue and red parts are caused by thermal excitations on the normal island and allows us to determine the degeneracy points for the graph. When the bias is lowered, we notice that the current at degeneracy vanishes whereas in Coulomb blockade a finite current persists.

In Fig. 6.2 (c) we show a numerical calculation with the parameter values $R_T = 90$ kΩ, $E_c = 0.74$ Δ and $\Delta = 216$ μeV of the experiment of panel (b). We have taken an elevated temperature $T_S = 205$ mK for the super-
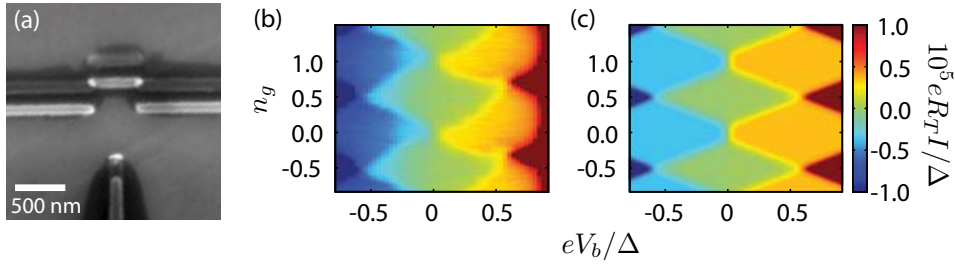
Figure 6.2. Probing quasiparticle excitations with a SINIS SET. (a), Scanning electron micrograph of a SINIS transistor designed for weak quasiparticle relaxation. (b), measured subgap current I as a function of the gate offset charge n_g and bias voltage V_b. (c), Simulated subgap current by elevated superconductor temperature. Figure adapted from Publication VII.

conductor, corresponding to $n_{qp} = 20\ \mu\mathrm{m}^{-3}$. We observe that the features of panel (b) are reproduced with good quantitative correspondence suggesting that the origin of the observed current is the presence of excess quasiparticle excitations. The current at degeneracy vanishes for small V_b. In this case, the SINIS transistor operates essentially as a single NIS junction which is insensitive to quasiparticle excitations as discussed in Sect. 2.2.2.

The current in Coulomb blockade is constant against V_b and n_g reflecting the bias independent tunneling rates of the quasiparticle excitations. The untrivial feature of the current being maximal in Coulomb blockade and not at degeneracy is understood with the following reasoning: when the excitations tunnel to the normal metallic island, the charge of the island moves away from the lowest energy state. Hence another tunneling event occurs soon after the first one to return the island charge to the preferred value. This tunneling occurs dominantly in the forward bias direction rectifying the quasiparticle excitation current and yielding a non-zero current. At degeneracy, the quasiparticle excitations cause tunneling between the two lowest charge states. The electrons tunnel equally to the forward and backward directions. Since these two charge states are equal in energy, no additional tunneling occurs for restoring the island charge back to the initial value.

The current at the light blue and orange terraces of Fig. 6.2 (b) and (c) is limited by the tunneling rate due to quasiparticle excitations of Eq. (6.2). The current through the device is given there as

$$I = \frac{n_{qp}}{e R_T D(E_F)}. \tag{6.4}$$

Since I is directly proportional to n_{qp}, measuring the current at the terrace probes direcly the quasiparticle density as soon as we know R_T and
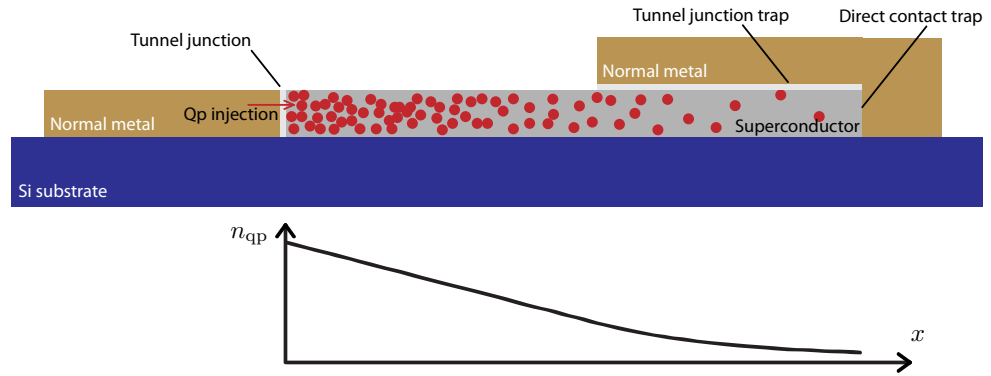
Figure 6.3. Diffusion of quasiparticles in a superconducting lead. Quasiparticles are injected from the normal metal to the superconductor via a tunnel junction. In order not to tunnel back to the normal metal, the quasiparticles need to diffuse through the bare superconducting section before reaching a trap which is either another (large) tunnel junction to a normal metal or a direct metal-to-metal contact on the right. Below, n_{qp} is sketched at different positions. In the bare diffusion part, n_{qp} is linear in distance and with the tunnel junction trap, it decays exponentially. For a direct contact trap we may generally assume n_{qp} to take the equilibrium value since there the quasiparticle relaxation is strong compared to the tunnel junctions.

$D(E_F)$. Having shown the sensitivity to quasiparticle excitations, the device was placed in a sample holder which protects better against stray infra-red radiation coming from the high temperature parts of the cryostat. Unlike in the first setup, in this case the experiment of Fig. 6.2 (b) showed no current around Coulomb blockade, see Publication VII, suggesting that n_{qp} is much lower now. The quasiparticle excitations are not anymore generated by Cooper-pair breaking due to stray radiation.

6.2 Diffusion equation for quasiparticles

We consider diffusion and relaxation of the quasiparticles in a superconducting lead. A typical situation is sketched in Fig. 6.3. Quasiparticle excitations are generated by electrons tunneling from normal metal to a superconductor. The excitations may tunnel back to the normal metal which is usually an unwanted process. To avoid this to happen, they need to diffuse through the superconducting line and relax. The inherent relaxation mechanism in the superconducting material, the electron-phonon interaction [12, 103, 104], is so weak that the dominant relaxation is provided in the devices studied in this section by diffusion into a normal metallic trap which either has a direct metal-to-metal contact to the superconductor or is separated by a tunnel barrier [105–107]. After reaching the normal metal, the quasiparticles relax there efficiently since the electron-phonon

relaxation rate is several orders of magnitude stronger in a normal metal than in a superconductor, see e.g. Publication IX and Ref. [108].

To obtain a diffusion equation for the quasiparticles we consider electrical heat conduction in a superconductor. The heat flow of the quasiparticles $\vec{J}$ follows the equation $\nabla \cdot \vec{J} = -p_{\text{trap}}$, where p_{trap} is the power removed from the quasiparticle population per unit volume. We use Fourier's law $\vec{J} = -\kappa_S \nabla T_S$, where

$$\kappa_S = \frac{6}{\pi^2} \frac{L_0 T_S}{\rho_n} (\beta_S \Delta)^2 e^{-\beta_S \Delta}, \tag{6.5}$$

is the heat conductivity of a superconductor at low temperatures $k_B T_S \ll \Delta$, see Ref. [109]. L_0 is the Lorenz number and ρ_n the normal state resistivity. Working out the derivates leads to

$$D \left(\nabla^2 n_{\text{qp}} + \frac{k_B T_S}{2\Delta \cdot n_{\text{qp}}} |\nabla n_{\text{qp}}|^2 \right) = p_{\text{trap}}, \tag{6.6}$$

where $D = \sqrt{2k_B T_S \Delta}/(\sqrt{\pi} e^2 D(E_F) \rho_n)$. This diffusion model has been used successfully in several experiments, see Refs. [106, 107, 110–112] and Publication VII. In the absence of a quasiparticle trap, we take $p_{\text{trap}} = 0$. For a tunnel junction trap we consider the heat extracted from the superconductor as in Eqs. (3.11) and (3.13) for the normal metal. The results are the same in this case except that in the integrand the energy $E \pm \delta E$ deposited to the normal metal is substituted with the energy E extracted from the superconductor. For the traps we have no bias voltage or charging effects so that $\delta E = 0$. We obtain then

$$p_{\text{trap}} = \frac{P_{\text{trap}}}{Ad} = \frac{\Delta}{e^2 R_T A d D(E_F)} (n_{\text{qp}} - n_{\text{qp0}}), \tag{6.7}$$

where n_{qp0} is the quasiparticle density in the absence of injection, A is the trap area yielding resistance R_T and d is the thickness of the film. We have assumed here that there is no gradient perpendicular to the film, i. e., we consider the diffusion equation only in two dimensions. This is a good approximation for the thin films used as at least one of the dimensions parallel to the film is much larger than the film thickness d. One obtains Eq. (6.7) also by multiplying Eq. (6.2) by Δ and 2, which are the energy carried by a single quasiparticle and the number of branches respectively, and normalizing by the junction area and film thickness. At low temperatures, $k_B T_S/\Delta \ll 1$, we may in addition neglect the second term in Eq. (6.6) and obtain a simple diffusion equation

$$D \nabla^2 n_{\text{qp}} = p_{\text{trap}}. \tag{6.8}$$
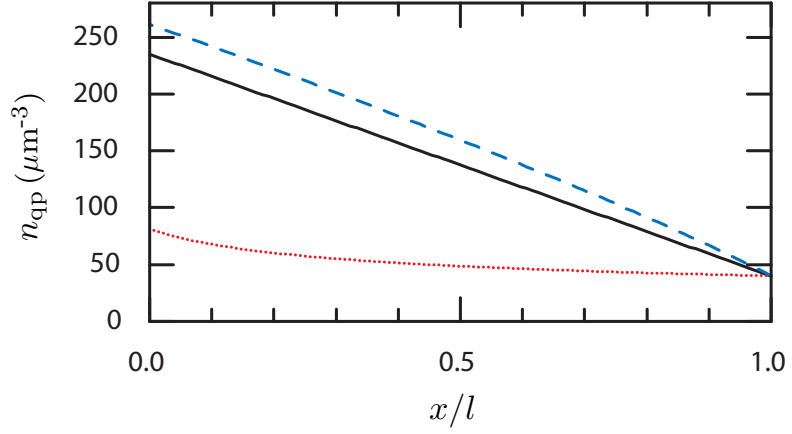
Figure 6.4. Approximation in quasiparticle diffusion calculations. Quasiparticle diffusion calculations for a superconducting line of $l = 20$ μm length. The cross-sectional area is 120 nm $\times$ 25 nm and the quasiparticle injection rate at $x = 0$ is 50 MHz corresponding to the structure representing weakest relaxation and employing maximal quasiparticle injection in Publication VII. The solid black line is calculated with Eq. (6.8) and the dashed blue line with Eq. (6.6). For the dotted red line, a constant heat conduction is assumed.

The approximation to obtain Eq. (6.8) is essentially the following. We consider the derivates of strong exponential dependencies only. The exponential dependence of κ_S on T_S in Eq. (6.5) is also included. Therefore this approximation is not as restrictive as a typical one in heat conduction calculations where the conductivity is assumed to be constant. In Publication VII the heat diffusion in superconducting leads was experimentally studied. The quasiparticles were injected by a SINIS turnstile operated at the first current plateau. The quasiparticle injection rate is then equal to the pumping frequency f. Measuring the dependence of the current on the pumping plateau against bias voltage allows one to determine n_{qp}. These measurements were repeated for several geometries and frequencies. Equation (6.8) was successfully used to predict the findings with the normal state resistivity $\rho_n = 30$ nΩm and the residual quasiparticle density of the aluminum film being the only fitting parameters. The same value of ρ_n was used for all different geometries and injection rates. The residual quasiparticle density n_{qp0} depends, however, on the particular geometry as expected.

To elaborate on the difference between Eqs. (6.6), (6.8) and the more limiting assumption of constant heat conduction, let us consider as an example the case of the 20 μm long aluminum line of Fig. 6.2 which had the weakest quasiparticle relaxation in Publication VII. In Fig. 6.4 we present the calculations based on Eqs. (6.6), (6.8) and the constant heat conduction. We observe that using Eq. (6.8) makes only an approximately
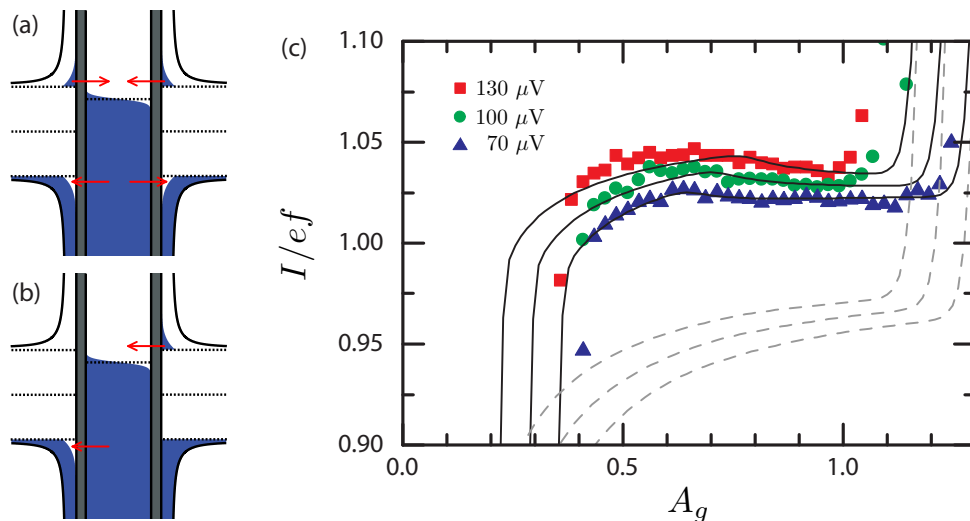
Figure 6.5. Branch imbalance in SINIS turnstile. (a), The DoS of a SINIS turnstile with quasiparticle excitations but no branch imbalance. The upper branch, $E > \Delta$, has the same number of excitations as the lower one, $E < -\Delta$. (b), The DoS with branch imbalance. Electrons are removed from the left superconductor resulting in hole excitations and deposited to the right superconductor resulting in particle excitations. Red arrows show the processes causing error to the operation. (c), Measured current I of the SINIS turnstile as a function of the gate amplitude A_g with $f = 5$ MHz and bias voltages $V_b = 70, \ 100$ and $130 \ \mu$V. The geometry of the device is similar to the one in Fig. 6.2 (a). Solid black lines are numerical calculations of Eq. (3.7) assuming no branch imbalance corresponding to panel (a) and dashed gray lines are with no branch-to-branch relaxation corresponding to panel (b).

10 % error compared to the accurate result of Eq. (6.6). However, if we would assume the heat conduction to be constant in the lead and taking the value at $x = 0$, the quasiparticle number would be underestimated by a factor of 3. This shows that Eq. (6.8) is sufficient for obtaining a quantitative understanding about quasiparticle relaxation in superconducting leads even for weak relaxation. In this example the quasiparticle density exceeds the thermal population by an order of magnitude. The more crude approximation of constant heat conduction is, however, not applicable here.

6.3   Branch imbalance in SINIS turnstile

For analysing the quasiparticle excitations under turnstile operation, we assumed no branch imbalance. The density of states (DoS) and the quasiparticle excitations of a SINIS turnstile without the branch imbalance are shown in Fig. 6.5 (a). Each of the superconductor branches have the same number of excitations. The excitations contribute to errors in turnstile operation with the processes indicated by the red arrows. In Fig. 6.5 (b)

we present a similar sketch but in presence of full branch imbalance. In this case, the excitations produce error processes to the backward direction only. If the relaxation between the branches is weak compared to the quasiparticle injection rate, the excitations of a SINIS turnstile would have the distribution of panel (b). The operation tends to form branch imbalance: on one of the superconducting leads quasiparticles are removed from the lower branch and they are deposited to the upper branch on the other superconductor leading to the situation of Fig. 6.5 (b).

In Fig. 6.5 (c) we present experimental data for a turnstile which has similar geometry as the one in Fig. 6.2 (a). The superconducting leads are 200 nm wide, 20 μm long and 25 nm thick. The geometry is chosen for having weak relaxation for the quasiparticles so that they dwell nearby the device and produce an observable signal on the pumping plateau. The device parameter values are $R_T = 700$ kΩ, $\Delta = 236$ μeV and $E_c/\Delta = 1.0$. The drive frequency is $f = 5$ MHz. Solid black curves show numerical calculations of Eq. (3.7) assuming no branch imbalance and taking $n_{\mathrm{qp}} = 1\,000$ μm^{-3}. Dashed gray line shows similar calculations but with the quasiparticles lying on one of the superconductor branches only, see panel (b). Based on the numerical calculations, we conclude that there is no significant charge imbalance in the SINIS turnstile: a 10 % difference in the population of the two branches would already lead to discrepancy between the experimental data and the numerical calculation. The position and the shape of the plateau fits the calculation without branch imbalance. If the branch imbalance is taken into accout, the plateau shape is different and it lies below $I = ef$. In this case the quasiparticle excitations generate error in the backward direction only. In order to match the experimental and the modeled curves, a 7 % correction would be required for the current amplifier gain. This is not feasible since the accuracy of the gain is typically better than 1 %. For the calculation without branch imbalance such correction is not needed. A quantitative analysis of the relaxation rates of the two branches is outside of the scope of this thesis.

6.4   Electron-phonon interaction in the superconducting state

In Sect. 6.2 we considered the relaxation of quasiparticles in superconducting leads. There, we neglected the relaxation mechanisms in the superconductor itself since in that case normal metallic parts of the structures were providing the dominant relaxation route. In order to observe
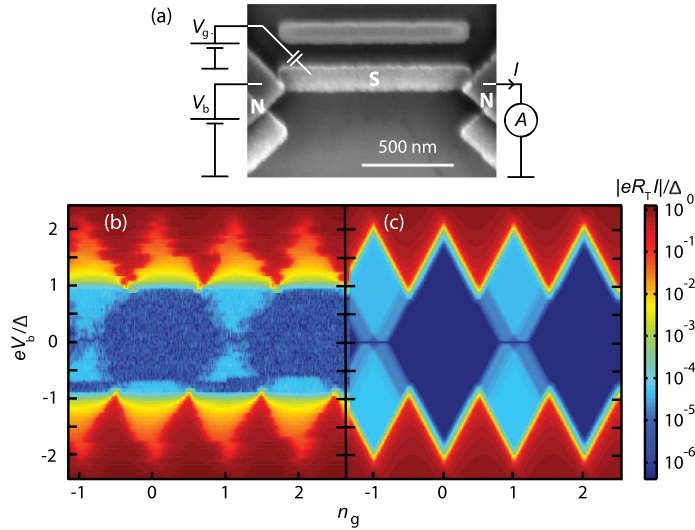
Figure 6.6. Probing quasiparticles on a small superconducting island. (a), A superconducting island (S) coupled to normal metallic leads (N) via two tunnel junctions. (b), The measured current I as a function of the bias voltage V_b and gate offset charge n_g. (c), Result of a numerical calculation based on Eq. (6.14) with the parameter values corresponding to the measurement in panel (b). Figure adapted from Publication IX.

the relaxation in the superconductor one can use fully superconducting systems [11, 12, 102, 108, 113, 114]. Another approach, involving normal metals, is shown in Fig. 6.6, see also Ref. [115]. It is based on having a small superconducting island weakly coupled to normal metallic leads and was utilized in Publication IX to study excitation and relaxation dynamics on the superconducting island down to a single excitation. Minimizing the relaxation to normal metallic parts allows us to probe the inherent relaxation mechanism of a superconductor, the electron-phonon interaction [103], as well as relaxation of single excitations via tunneling. First, in Sect. 6.4.1 we discuss the electron-phonon interaction and derive recombination rates essential for this system and then in Sect. 6.4.2 we present the experiments allowing one to study the relaxation dynamics quantitatively.

6.4.1 Derivation of heat flux and related quantities

For studying the electron-phonon interaction in the superconducting state we utilize the same perturbative formalism as in Sect. 2.2. In this case the Hamiltonian reads

$$\hat{H} = \hat{H}_S + \hat{H}_p + \hat{H}_{e-\mathrm{ph}}, \qquad (6.9)$$

where $\hat{H}_S$ is given by Eq. (2.4) and

$$\hat{H}_p = \sum_q \hbar \omega_q b_q^\dagger b_q, \tag{6.10}$$

is the Hamiltonian for phonons. $b_q^\dagger$ is the creation operator of a phonon with energy $\hbar \omega_q$ and wavevector q. The coupling of the electron and phonon systems is assumed to have the form

$$\hat{H}_{e-\mathrm{ph}} = \nu \sum_{k,q} \omega_q^{1/2} (c_k^\dagger c_{k-q} b_q + c_k^\dagger c_{k+q} b_q^\dagger). \tag{6.11}$$

as in Ref. [116]. The operator of heat flux to the phonons is

$$\dot{\hat{H}}_p = \frac{i}{\hbar}[\hat{H}, \hat{H}_p] = \frac{i}{\hbar}[\hat{H}_{e-\mathrm{ph}}, \hat{H}_p] = i\nu \sum_{k,q} \omega_q^{3/2}(c_k^\dagger c_{k-q} b_q - c_k^\dagger c_{k+q} b_q^\dagger). \tag{6.12}$$

By evaluating the expectation value of $\dot{\hat{H}}_p$ with the technique of Sect. 2.2 we obtain the heat flux due to electron-phonon interaction as

$$
\begin{aligned}
\dot{Q}_{e-\mathrm{ph}} &= \frac{\Sigma V}{24\zeta(5)k_B^5} \int_0^\infty d\epsilon\, \epsilon^3 \left(n(\epsilon, T_S) - n(\epsilon, T_P)\right) \int_{-\infty}^\infty dE \times \\
&\quad n_S(E)n_S(E+\epsilon)\left(1 - \frac{\Delta^2}{E(E+\epsilon)}\right)(f(E) - f(E+\epsilon)),
\end{aligned}
\tag{6.13}
$$

where Σ is the electron-phonon coupling constant, V the volume of the superconductor, $\zeta(5) = 1.037$ a value of the Riemann zeta function, $n(\epsilon, T) = (e^{\epsilon/k_B T} - 1)^{-1}$ the Bose-Einstein distribution at temperature T, T_P is the temperature of the phonons, T_S the electron temperature of the superconductor and ϵ is the phonon energy. See the supplemental material of Publication IX for intermediate steps. Equation (6.13) is also found in Ref. [108], where the heat flux was measured by using superconducting tunnel junctions, and it was derived there by kinetic Boltzmann equation calculations [117].

The heat flux of Eq. (6.13) consists of scattering and recombination. In the recombination process two electrons form a Cooper pair thus changing the number of excitations. Scattering on the other hand does not change the number of quasiparticle excitations but it leads to heat flux as it changes the energy which a quasiparticle carries. Equation (6.13) can be split into recombination and scattering terms which at low temperature, $T_P \ll T_S \ll \Delta/k_B$ read

$$
\begin{aligned}
\dot{Q}_{\mathrm{rec}}(T_S) &\approx \frac{\pi V \Sigma}{3\zeta(5)k_B^5}(k_B T_S \Delta^4 + \frac{7}{4}(k_B T_S)^2 \Delta^3)e^{-2\Delta/k_B T_S}, \\
\dot{Q}_{\mathrm{sc}}(T_S) &\approx V \Sigma T_S^5 e^{-\Delta/k_B T_S}.
\end{aligned}
$$

Since recombination involves two quasiparticles, each carrying an energy of at least Δ, the exponential suppression involves energy 2Δ. Similarly,
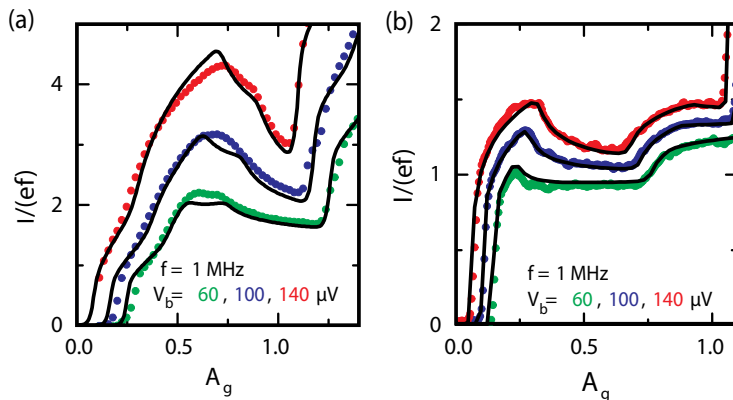
Figure 6.7. Current of a NISIN transistor under turnstile operation. The current I through the transistor is shown for various bias voltages V_b as a function of the gate offset amplitude A_g in the range where the first quantized plateau $I = ef$ should form for $E_c = 240~\mu\text{eV}$ in panel (a) and $E_c = 620~\mu\text{eV}$ in panel (b). Dots present measured values and solid black lines numerical calculations based on Eq. (3.7). Figure adapted from Publication IX.

scattering involves energy Δ in the exponential suppression. The scattering involves a single quasiparticle and it takes place within one of the branches only. The heat flux scales thus as $\dot{Q}_{\text{sc}} \propto n_{\text{qp}} \propto e^{-\Delta/k_B T_S}$.

### 6.4.2 Recombination rates on a small superconducting island

Let us now turn back to consider the device presented in Fig. 6.6. The single-electron tunneling processes for this device are identical to the SINIS turnstile, see discussion under Eq. (2.26) and Ref. [49]. Therefore we may drive it by a gate voltage as was done for the SINIS turnstile and ideally quantized current plateaus would form. However, the single-electron tunneling creates quasiparticle excitations on the superconducting island. The excitations cannot relax to normal metallic traps as easily as in the "large" and "trapped" superconducting leads of Sect. 6.2. The weak thermal coupling provides an efficient way of probing the electron-phonon relaxation. In Fig. 6.7 we show the region where the first pumping plateau should form for the two different devices presented. We observe that the current plateaus are practically absent. The experimental curves have nontrivial features which are sensitive to the charging energy of the device and they are reproduced accurately by the numerical results based on the master equation approach of Eq. (3.7). In the simulations, the temperature of the superconductor T_S is allowed to differ from the phonon temperature T_0. For each point of Fig. 6.7, T_S is found by balancing the heat injection via tunneling with the electron-phonon heat flux of Eq. (6.13). The experiment and the heat balance calculations were repeated at vari-

ous pumping frequencies f in Publication IX and a good agreement with Eq. (6.13) was found over a wide range of heat fluxes.

6.4.3 Single quasiparticle effects

In the experiments of Fig. 6.7, the average number of excitations was of the order $N_{\mathrm{qp}} \sim 10$. When an electron tunneling event takes place, this number is changed by one and in a recombination process it changes by two. Such processes cause fluctuations to N_{qp} within the turnstile cycle [75]. Since the average number of excitations is an order of magnitude larger than the fluctuations, it is an adequate approximation to model the system by using a time-independent temperature for the superconducting island. However, if the frequency is lowered, or ultimately in a static situation, the number of quasiparticles decreases close to $N_{\mathrm{qp}} = 0$ at low temperatures [4, 7, 74, 118, 119]. This is obviously a situation where such a thermal description is not valid. Looking back to Fig. 6.6 (b) we notice that for $|eV_b| < \Delta$, the periodicity in n_g is doubled as compared to that at $|eV_b| > \Delta$. For the high bias, the operation is equivalent to that of a SINIS device with 1e-periodicity and no significant sensitivity to the single-quasiparticle excitations. At low bias values the situation is opposite. If n_g is set close to an even integer, the island holds an even number of electrons which are all paired [118]. Hence the current vanishes. If n_g is close to an odd integer, there is an odd number of electrons on the island and one of them is naturally unpaired. It remains as a quasiparticle excitation carrying an energy of at least Δ. With the given energy, it can readily escape from the island by tunneling to a normal metal lead. Due to charging energy costs, proportional to E_c, another electron tunnels, however, into the superconducting island to recover the preferred number of electrons. For $E_c \sim \Delta$, both of these processes are active. Such a situation was realized in the experiment. The cycle then repeats and causes an experimentally observable current "terrace" similar in shape to those in Figs. 6.2 (b) and (c).

If the superconducting island is assumed to have an average temperature T_S, we can utilize the master equation (3.7) with elevated T_S for the calculations. This would result in a graph similar to that in Fig. 6.2 (c). The result is correct apart from the current terrace around even n_g values. Therefore the change in the parity in Fig. 6.6 is a clear sign of at most a single quasiparticle present. To model this situation correctly, we
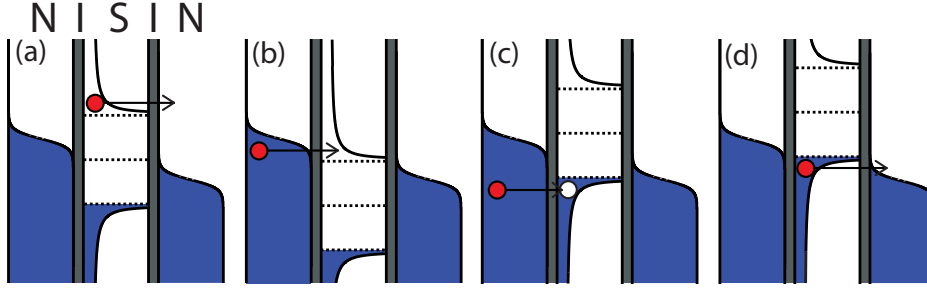
N I S I N

Figure 6.8.   Tunneling in a NISIN transistor.   (a), The tunneling rate $\Gamma_{N \to N-1, N_S \to N_S -1}$ is generated by quasiparticle excitations in the superconductor with energy $E > \Delta$ tunneling out of the island. The opposing process, tunneling into $E > \Delta$, contributes to $\Gamma_{N \to N+1, N_S \to N_S+1}$ shown in panel (b). Similarly, tunneling with energies $E < -\Delta$ contributes to $\Gamma_{N \to N+1, N_S \to N_S -1}$, shown in panel (c), and $\Gamma_{N \to N-1, N_S \to N_S+1}$, shown in panel (d).   Figure adapted from Publication IX.

extend the master equation (3.7) to

$$\frac{d}{dt}P(N, N_S) = \sum_{N', N_S'} \Gamma_{N' \to N, N_S' \to N_S} P(N', N_S'), \qquad (6.14)$$

where $P(N, N_S)$ is the probability of having N excess electrons and N_S quasiparticle excitations on the island, and $\Gamma_{N' \to N, N_S' \to N_S}$ is the transition rate from N', N_S' to N, N_S. The rates are set by electron tunneling and recombination. Tunneling is calculated using Eqs. (2.25) and (2.26) by treating separately processes where energy is removed and deposited to the superconductor as shown in Fig. 6.8. For explicit formulas of the tunneling rates, see the supplemental material of Publication IX.

At low temperatures, we may assume each quasiparticle excitation to carry energy $E = \Delta$. Then we obtain the recombination rate from Eq. (6.14) by dividing $\dot{Q}_{\rm rec}$ by 2Δ, the latter being the energy carried by the two recombining quasiparticles. Rewriting the result in terms of N_S leads to

$$\Gamma_{N \to N, N_S \to N_S -2} \approx \frac{\Sigma \Delta^2}{12\zeta(5)D(E_F)^2 k_B^5 V} N_S^2, \qquad (6.15)$$

for $N_S \geq 2$. For $N_S = 0, 1$ we have $\Gamma_{N \to N, N_S \to N_S -2} = 0$ since a single excitation cannot pair.

With Eq. (6.14), the experiment of Fig. 6.6 (b) is reproduced up to a high degree as shown in Fig. 6.6 (c). The current terrace around odd values of n_g with $|eV_b| < \Delta$ is caused by the single quasiparticle excitation. The current at the terrace is set by Eq. (6.4) with $n_{\rm qp} = 1/V$ which is the quasiparticle density due to a single excitation. Hence the current at the terrace allows one to determine the single quasiparticle relaxation rate via tunneling. In addition, in pumping experiments at lower frequencies than that in Fig. 6.7, recombination rates of Eq. (6.15) are probed down to

a single quasiparticle pair as reported in Publication IX. In the modeling based on Eq. (6.14), the energy relaxation of the quasiparticle due to scattering was neglected as all the quasiparticles were assumed to be injected near the gap edges. In Ref. [75] an alternative formalism is used, which allows one to consider the scattering relaxation as well. It is shown there that for the transport and quasiparticle relaxation in a NISIN transistor, it is not important to take into account the scattering explicitly. However, if the quasiparticles are injected to energies $E \gg \Delta$, and the device operation is sensitive to the exact distribution, this would be an issue [120].

In addition to the probing of electron-phonon interaction, the NISIN transistor can be utilized to probe the Cooper pair breaking in a superconductor. The vanishing current at even values of n_g in Fig. 6.6 (b) allows one to estimate an upper limit for the spontaneous Cooper pair breaking rate on the island which depends presumably on the microwave background in the setup. The broken Cooper pairs would result in a terrace around even values of n_g. Therefore the measurement resolution allows us to determine an upper limit for the number of broken Cooper pairs on the superconducting island. With the relaxation dynamics described above, we evaluate the pair breaking rate to be less than $2 \, \mathrm{kHz}$ which in turn corresponds to less than $0.1 \, \mathrm{aW}$ power on the superconducting island.

7. Summary

This thesis focused on studying electrical transport in nanoscaled tunnel junctions between a normal metal and a superconductor. The main emphasis was put on understanding the two-electron Andreev tunneling and quasiparticle excitations in the superconductor. We demonstrated various experimental methods for detecting these phenomena and utilized them to study what kind of influences these two phenomena impose on the devices based on tunnel junctions and superconductors in general. Further on, we analyzed which quantities influence on the two phenomena and how.

For the two-electron Andreev tunneling we showed that charging effects give rise to such features in the current-voltage curves which distinguish this process from other leakage sources. This distinction is not possible for voltage biased NIS junctions. We saw that Andreev tunneling becomes suppressed if the charging energy is made sufficiently large, an essential feature for improved accuracy of the SINIS turnstile. In addition, we utilized counting techniques for demonstrating in real time the presence of two electrons carrying the current in the Andreev process. The electron counting allowed us to consider the statistics as well.

For investigating the quasiparticle excitations we also used the electron counting techniques. We demonstrated that the excitations give rise to a tunneling rate which is independent of the energy cost and that with sufficient shielding the excitations become largely suppressed. With the help of charging effects we were able to probe the excitations by a simpler direct current measurement where the quasiparticles generate a bias independent current. By driving a SINIS turnstile, a controlled injection and detection of quasiparticles was obtained. The diffusion and relaxation of the excitations in superconducting leads was studied. The inverse NISIN structure, on the other hand, was utilized to study the recombina-

tion mechanism of the superconductors by phonon emission, down to the level of a few excitations only.

The suppressed Andreev tunneling in a SINIS turnstile, which we demonstrated experimentally, is an important step towards optimizing the accuracy of the turnstile. With the Andreev tunneling being suppressed, the fundamental multi-electron process limiting the accuracy is the cotunneling of a Cooper pair and an electron [49]. Based on the present knowledge, a relative accuracy on the 10^{-7} level is obtainable with an output current on the level of 10 pA. This would call for ten parallel devices, also demonstrated in this thesis, in order to obtain sufficiently large current for metrological applications [50, 51]. On the other hand the studies on quasiparticle excitations showed us that providing sufficient relaxation for them is a crucial issue for the accuracy of the SINIS turnstile and requires a careful optimization for reaching the highest accuracy for the current quantization. With the best devices used in this thesis, the relative accuracy of the SINIS turnstile was shown to be on the low 10^{-4} level but still limited by the quasiparticle excitations. For reaching 10^{-7} relative accuracy, the evacuation and relaxation of the excitations need to be increased by a factor of 1000. In order to fulfill this requirement, the most apparent approach would be to decrease the normal state resistivity ρ_n, which in principle should be feasible with ultra pure aluminum [121]. However, obtaining single crystalline structure and small number of impurities yielding low ρ_n will be troublesome for thin films. Increasing the film thickness might help for this goal as the surface scattering will be then weaker. The thicker film would also help the evacuation of the excitations since then they would spread to a larger volume. In addition, creating vortices by applying a magnetic field, the relaxation on the superconducting leads might be increased [104]. If all these approaches turn out to be futile, increasing the tunnel resistances of the device will increase the relative accuracy: the obtainable output current is proportional to the drive frequency being inversely proportional to resistance: $f \propto 1/R_T$. The error in the current on the other hand is proportional to $f/R_T \propto 1/R_T^2$, since f is the injection frequency of the quasiparticles and $1/R_T$ their tunneling rate causing the errors. Hence the relative accuracy limited by the quasiparticles scales as $1/R_T$. Increasing the resistance is however not a tempting option since it would call for more devices in parallel.

Instead of improving the accuracy of a device itself, there is an alterna-
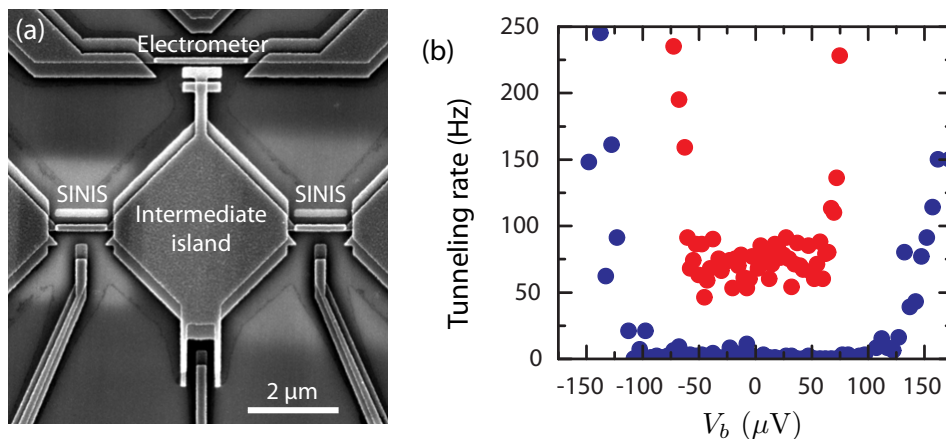
Figure 7.1. Error counting in SINIS turnstiles. (a), Two SINIS turnstiles connected in series with an intermediate island in between. An electrometer reads the number of excess electrons on the intermediate island. (b), Tunneling rate to the intermediate island as a function of the bias voltage V_b per junction. For red points, the SINIS turnstiles are kept at degeneracy and for the blue points they are in Coulomb blockade. The bias independent tunneling rate at degeneracy suggests that there are excess quasiparticles present.

tive approach to satisfy the stringent accuracy requirement. In this approach errors are detected by electron counting techniques and the error is taken into account when determining the obtained current [122, 123]. A possible device for error counting of a SINIS turnstile is shown in Fig. 7.1 (a). It consists of two SINIS turnstiles which have an intermediate island in between. The number of electrons on the intermediate island is monitored by an electrometer. Both of the turnstiles are operated at the same frequency. If either of the turnstiles fails to transport an electron in a cycle, it is detected by the electrometer. If the errors occur at a low frequency $f_{\mathrm{err}} \ll f_{\mathrm{det}}$, the electrometer is able to resolve them reliably and thus they can be taken into account. Here f_{det} is the bandwidth of the detector. For this setup, we need to know which direction the errors occur in order to compensate them. Since the operation of the turnstile can be described with a high precision as shown in this thesis, it provides a solid basis for arguments about the direction. Alternative approach would be to add one more turnstile in series and detect electrons on two intermediate islands allowing to resolve the direction of tunneling [81]. In Fig. 7.1 (b) we present the measured tunneling rate to the intermediate island under static conditions when the turnstiles are either at degeneracy or in Coulomb blockade. We observe that at degeneracy, we have a bias independent tunneling rate suggesting that there are excess quasiparticles present. We expect the relaxation of the quasiparticles to be weak on the superconducting intermediate island. Hence, finding excess quasiparti-

cles on it is not surprising. In order to accomplish the error counting in the turnstiles, a stronger quasiparticle relaxation is needed especially for the intermediate island. With the direct metal-to-metal traps, more efficient trapping should be feasible [112]. This, however, remains to be tested. Hopefully in the future we will also see whether either the SINIS turnstile or the competing semiconductor pumps [30, 124–126] reach the demanding accuracy requirements and fulfill all the requirements for the redefinition of the SI unit system.

Bibliography

[1] M. Tinkham, *Introduction to superconductivity*, 2nd ed. (McGraw-Hill, New York, 1996).

[2] A. F. Andreev, Sov. Phys. JETP **19**, 1228 (1964).

[3] G. E. Blonder, M. Tinkham, and T. M. Klapwijk, Phys. Rev. B **25**, 4515 (1982).

[4] T. M. Eiles, J. M. Martinis, and M. H. Devoret, Phys. Rev. Lett. **70**, 1862 (1993).

[5] H. Pothier, S. Guéron, D. Esteve, and M. H. Devoret, Phys. Rev. Lett. **73**, 2488 (1994).

[6] F. W. J. Hekking and Y. V. Nazarov, Phys. Rev. B **49**, 6847 (1994).

[7] J. M. Hergenrother, M. T. Tuominen, and M. Tinkham, Phys. Rev. Lett. **72**, 1742 (1994).

[8] S. Rajauria, P. Gandit, T. Fournier, F. W. J. Hekking, B. Pannetier, and H. Courtois, Phys. Rev. Lett. **100**, 207002 (2008).

[9] A. S. Vasenko, E. V. Bezuglyi, H. Courtois, and F. W. J. Hekking, Phys. Rev. B **81**, 094513 (2010).

[10] M. D. Shaw, R. M. Lutchyn, P. Delsing, and P. M. Echternach, Phys. Rev. B **78**, 024503 (2008).

[11] R. Barends, J. J. A. Baselmans, S. J. C. Yates, J. R. Gao, J. N. Hovenier, and T. M. Klapwijk, Phys. Rev. Lett. **100**, 257002 (2008).

[12] J. M. Martinis, M. Ansmann, and J. Aumentado, Phys. Rev. Lett. **103**, 097002 (2009).

[13] P. de Visser, J. Baselmans, P. Diener, S. Yates, A. Endo, and T. Klapwijk, Phys. Rev. Lett. **106**, 167004 (2011).

[14] H. Paik, D. I. Schuster, L. S. Bishop, G. Kirchmair, G. Catelani, A. P. Sears, B. R. Johnson, M. J. Reagor, L. Frunzio, L. I. Glazman, S. M. Girvin, M. H. Devoret, and R. J. Schoelkopf, Phys. Rev. Lett. **107**, 240501 (2011).

[15] Y. Makhlin, G. Schön, and A. Shnirman, Rev. Mod. Phys. **73**, 357 (2001).

[16] F. Giazotto, T. T. Heikkilä, A. Luukanen, A. M. Savin, and J. P. Pekola, Rev. Mod. Phys. **78**, 217 (2006).

[17] L. Sun, L. DiCarlo, M. D. Reed, G. Catelani, L. S. Bishop, D. I. Schuster, B. R. Johnson, G. A. Yang, L. Frunzio, L. Glazman, M. H. Devoret, and R. J. Schoelkopf, Phys. Rev. Lett. **108**, 230509 (2012).

[18] M. Lenander, H. Wang, R. C. Bialczak, E. Lucero, M. Mariantoni, M. Neeley, A. D. O'Connell, D. Sank, M. Weides, J. Wenner, T. Yamamoto, Y. Yin, J. Zhao, A. N. Cleland, and J. M. Martinis, Phys. Rev. B **84**, 024501 (2011).

[19] A. J. Ferguson, N. A. Court, F. E. Hudson, and R. G. Clark, Phys. Rev. Lett. **97**, 106603 (2006).

[20] R. A. Millikan, Phys. Rev. (Ser. I) **32**, 349 (1911).

[21] R. A. Millikan., Phys. Rev. **2**, 109 (1913).

[22] D. V. Averin and K. K. Likharev, "Mesoscopic phenomena in solids," (Nature Publishing Group, Amsterdam, 1991) p. 173.

[23] G. L. Ingold and Y. V. Nazarov, "Single charge tunneling, coulombblockade phenomena in nanostructures, ch 2," (Plenum Press, New York, 1992) p. 21.

[24] D. Esteve, "Single charge tunneling, coulomb blockade phenomena in nanostructures, ch 3," (Plenum Press, New York, 1992).

[25] H. Pothier, P. Lafarge, C. Urbina, D. Esteve, and M. H. Devoret, Europhys. Lett. **17**, 249 (1992).

[26] D. V. Averin and Y. V. Nazarov, "Single charge tunneling, coulomb blockade phenomena in nanostructures, ch 9," (Plenum Press, New York, 1992).

[27] M. H. Devoret, D. Esteve, and C. Urbina, Nature **360**, 547 (1992).

[28] M. W. Keller, J. M. Martinis, N. M. Zimmerman, and A. H. Steinbach, Appl. Phys. Lett. **69**, 1804 (1996).

[29] A. Fujiwara and Y. Takahashi, Nature **410**, 560 (2001).

[30] S. P. Giblin, M. Kataoka, J. D. Fletcher, P. See, T. J. B. M. Janssen, J. P. Griffiths, G. A. C. Jones, I. Farrer, and D. A. Ritchie, Nature Comm. **3**, 930 (2012).

[31] L. J. Geerligs, V. F. Anderegg, P. A. M. Holweg, J. E. Mooij, H. Pothier, D. Esteve, C. Urbina, and M. H. Devoret, Phys. Rev. Lett. **64**, 2691 (1990).

[32] M. W. Keller, A. L. Eichenberger, J. M. Martinis, and N. M. Zimmerman, Science **285**, 1706 (1999).

[33] L. P. Kouwenhoven, A. T. Johnson, N. C. van der Vaart, C. J. P. M. Harmans, and C. T. Foxon, Phys. Rev. Lett. **67**, 1626 (1991).

[34] J. P. Pekola, J. J. Vartiainen, M. Möttönen, O.-P. Saira, M. Meschke, and D. V. Averin, Nature Phys. **4**, 120 (2008).

[35] J. Bardeen, L. N. Cooper, and J. R. Schrieffer, Phys. Rev. **108**, 1175 (1957).

[36] N. N. Bogoliubov, Zh. Eksperim. Teor. Fiz. **34**, 58 (1958).

[37] J. G. Valatin, Nuovo Cimento **7**, 843 (1958).

[38] G. J. Dolan, Appl. Phys. Lett. **31**, 337 (1977).

[39] T. A. Fulton and G. Dolan, Physical Review Letters **59**, 109 (1987).

[40] F. Schwabl, *Quantum Mechanics*, 3rd ed. (Springer, Berlin, 2002).

[41] I. Giaever, Phys. Rev. Lett. **5**, 147 (1960).

[42] J. Clarke, Phys. Rev. Lett. **28**, 1363 (1972).

[43] D. V. Averin and K. K. Likharev, J. Low Temp. Phys. **62**, 345 (1986).

[44] K. K. Likharev, IEEE Trans. Magn. **23**, 1142 (1987).

[45] P. G. De Gennes, *Superconductivity of Metals and Alloys* (Advanced Book Program, Perseus Books, New York, 1999).

[46] O.-P. Saira, M. Meschke, F. Giazotto, A. M. Savin, M. Möttönen, and J. P. Pekola, Phys. Rev. Lett. **99**, 027203 (2007).

[47] S. Kafanov, A. Kemppinen, Y. A. Pashkin, M. Meschke, J. S. Tsai, and J. P. Pekola, Phys. Rev. Lett. **103**, 120801 (2009).

[48] F. C. Wellstood, C. Urbina, and J. Clarke, Phys. Rev. B **49**, 5942 (1994).

[49] D. V. Averin and J. P. Pekola, Phys. Rev. Lett. **101**, 066801 (2008).

[50] K. K. Likharev and A. B. Zorin, J. Low Temp. Phys. **59**, 347 (1985).

[51] F. Piquemal, C.R. Physique **5**, 857 (2004).

[52] J. Flowers, Science **306**, 1324 (2004).

[53] A. Kemppinen, S. Kafanov, Y. A. Pashkin, J. S. Tsai, D. V. Averin, and J. P. Pekola, Appl. Phys. Lett. **94**, 172108 (2009).

[54] M. H. Devoret, D. Esteve, H. Grabert, G.-L. Ingold, H. Pothier, and C. Urbina, Phys. Rev. Lett. **64**, 1824 (1990).

[55] S. M. Girvin, L. I. Glazman, M. Jonson, D. R. Penn, and M. D. Stiles, Phys. Rev. Lett. **64**, 3183 (1990).

[56] J. M. Martinis and M. Nahum, Phys. Rev. B **48**, 18316 (1993).

[57] J. M. Hergenrother, J. G. Lu, M. T. Tuominen, D. C. Ralph, and M. Tinkham, Phys. Rev. B **51**, 9407 (1995).

[58] W. Schottky, Ann. Phys. **57**, 541 (1918).

[59] A. N. Korotkov, Phys. Rev. B **49**, 10381 (1994).

[60] A. O. Caldeira and A. J. Leggett, Phys. Rev. Lett. **46**, 211 (1981).

[61] H. B. Callen and T. A. Welton, Phys. Rev. **83**, 34 (1951).

[62] K. von Klitzing, G. Dorda, and M. Pepper, Phys. Rev. Lett. **45**, 494 (1980).

[63] R. C. Dynes, V. Narayanamurti, and J. P. Garno, Phys. Rev. Lett. **41**, 1509 (1978).

[64] R. C. Dynes, J. P. Garno, G. B. Hertel, and T. P. Orlando, Phys. Rev. Lett. **53**, 2437 (1984).

[65] G. O'Neil, D. Schmidt, N. Miller, J. Ullom, K. Iwrin, A. Williams, G. Arnold, and S. Ruggiero, Journal of Low Temperature Physics **151**, 70 (2008).

[66] H. Courtois, S. Rajauria, P. Gandit, F. Hekking, and B. Pannetier, Journal of Low Temperature Physics **153**, 325 (2008).

[67] P. Koppinen, T. Kühn, and I. Maasilta, J. Low Temp. Phys. **154**, 179 (2009).

[68] H. Jung, Y. Kim, K. Jung, H. Im, Y. A. Pashkin, O. Astafiev, Y. Nakamura, H. Lee, Y. Miyamoto, and J. S. Tsai, Phys. Rev. B **80**, 125413 (2009).

[69] D. C. Ralph, C. T. Black, and M. Tinkham, Phys. Rev. Lett. **74**, 3241 (1995).

[70] T. Greibe, M. P. V. Stenberg, C. M. Wilson, T. Bauch, V. S. Shumeiko, and P. Delsing, Phys. Rev. Lett. **106**, 097001 (2011).

[71] A. B. Zorin, S. V. Lotkhov, H. Zangerle, and J. Niemeyer, J. Appl. Phys. **88**, 2665 (2000).

[72] S. V. Lotkhov, S. A. Bogoslovsky, A. B. Zorin, and J. Niemeyer, Appl. Phys. Lett. **78**, 946 (2001).

[73] V. Bubanja, Phys. Rev. B **83**, 195312 (2011).

[74] D. V. Averin and Y. V. Nazarov, Phys. Rev. Lett. **69**, 1993 (1992).

[75] A. Heimes, V. F. Maisi, D. S. Golubev, M. Marthaler, G. Shcön, and J. P. Pekola, arXiv:1310.6508 (2013).

[76] L. Landau and E. Lifshitz, "Quantum mechanics," (Pergamon, 1980) p. Sec. 43.

[77] J. Wei and V. Chandrasekhar, Nature Phys. **6**, 494 (2010).

[78] F. W. J. Hekking, L. I. Glazman, K. A. Matveev, and R. I. Shekhter, Phys. Rev. Lett. **70**, 4138 (1993).

[79] M. Field, C. Smith, M. Pepper, D. Ritchie, J. Frost, G. Jones, and D. Hasko, Phys. Rev. Lett. **70**, 1311 (1993).

[80] M. C. Cassidy, A. S. Dzurak, R. G. Clark, K. D. Petersson, I. Farrer, D. A. Ritchie, and C. G. Smith, Appl. Phys. Lett. **91**, 222104 (2007).

[81] B. Küng, C. Rössler, M. Beck, M. Marthaler, D. S. Golubev, Y. Utsumi, T. Ihn, and K. Ensslin, Phys. Rev. X **2**, 011001 (2012).

[82] O.-P. Saira, *Electrostatic control of quasipartice transport in superconducting hybrid nanostructures* (PhD Thesis, O. V. Lounasmaa Laboratory, Aalto University, 2013).

[83] G. Zimmerli, T. M. Eiles, R. L. Kautz, and J. M. Martinis, Applied Physics Letters **61**, 237 (1992).

[84] V. A. Krupenin, J. Appl. Phys. **84**, 3212 (1998).

[85] L. Roschier, R. Tarkiainen, M. Ahlskog, M. Paalanen, and P. Hakonen, Appl. Phys. Lett. **78**, 3295 (2001).

[86] W. Lu, Z. Ji, L. Pfeiffer, K. W. West, and A. J. Rimberg, Nature **423**, 422 (2003).

[87] R. Landauer, Nature **392**, 1998 (1998).

[88] V. A. Khlus, Sov. Phys. JETP **66**, 1243 (1987).

[89] M. J. M. de Jong and C. W. J. Beenakker, Phys. Rev. B **49**, 16070 (1994).

[90] X. Jehl, M. Sanquer, R. Calemczuk, and D. Mailly, Nature **405**, 50 (2000).

[91] A. Das, Y. Ronen, M. Heiblum, D. Mahalu, A. V. Kretinin, and H. Shtrikman, Nat. Commun. **3**, 1165 (2012).

[92] S. Gustavsson, R. Leturcq, B. Simovič, R. Schleser, T. Ihn, P. Studerus, K. Ensslin, D. C. Driscoll, and A. C. Gossard, Phys. Rev. Lett. **96**, 076605 (2006).

[93] C. Fricke, F. Hohls, W. Wegscheider, and R. J. Haug, Phys. Rev. B **76**, 155307 (2007).

[94] E. Sukhorukov, A. N. Jordan, S. Gustavsson, R. Leturq, T. Ihn, and K. Ensslin, Nature Phys. **3**, 243 (2007).

[95] N. Ubbelohde, C. Fricke, C. Flindt, F. Hohls, and R. J. Haug, Nature Comm. **3**, 612 (2012).

[96] T. Fujisawa, T. Hayashi, T. Ritsuya, and Y. Hirayama, Science **312**, 1634 (2006).

[97] D. A. Bagrets and Y. V. Nazarov, Phys. Rev. B **67**, 085316 (2003).

[98] C. Emary, D. Marcos, R. Aguado, and T. Brandes, Phys. Rev. B **76**, 161404 (2007).

[99] C. Flindt, T. c. v. Novotný, A. Braggio, M. Sassetti, and A.-P. Jauho, Phys. Rev. Lett. **100**, 150601 (2008).

[100] C. Flindt, T. c. v. Novotný, A. Braggio, and A.-P. Jauho, Phys. Rev. B **82**, 155407 (2010).

[101] N. Ashcroft and N. Mermin, *Solid State Physics* (Saunders College, Philadelphia, 1976).

[102] D. Riste, C. C. Bultink, M. J. Tiggelman, R. N. Schouten, K. W. Lehnert, and L. DiCarlo, Nature Comm. **4**, 1913 (2013).

[103] A. Rothwarf and B. N. Taylor, Phys. Rev. Lett. **19**, 27 (1967).

[104] J. T. Peltonen, J. T. Muhonen, M. Meschke, N. B. Kopnin, and J. P. Pekola, Phys. Rev. B **84**, 220502 (2011).

[105] J. P. Pekola, D. V. Anghel, T. I. Suppula, J. K. Suoknuuti, A. J. Manninen, and M. Manninen, Appl. Phys. Lett. **76**, 2782 (2000).

[106] S. Rajauria, H. Courtois, and B. Pannetier, Phys. Rev. B **80**, 214521 (2009).

[107] G. C. O'Neil, P. J. Lowell, J. M. Underwood, and J. N. Ullom, Phys. Rev. B **85**, 134504 (2012).

[108] A. V. Timofeev, C. P. Garcia, N. B. Kopnin, A. M. Savin, M. Meschke, F. Giazotto, and J. P. Pekola, Phys. Rev. Lett. **102**, 017003 (2009).

[109] J. Bardeen, G. Rickayzen, and L. Tewordt, Phys. Rev. **113**, 982 (1959).

[110] J. N. Ullom, P. A. Fisher, and M. Nahum, Phys. Rev. B **58**, 8225 (1998).

[111] A. V. Timofeev, M. Helle, M. Meschke, M. Möttönen, and J. P. Pekola, Phys. Rev. Lett. **102**, 200801 (2009).

[112] J. T. Peltonen, P. Virtanen, M. Meschke, J. V. Koski, T. T. Heikkilä, and J. P. Pekola, Phys. Rev. Lett. **105**, 097004 (2010).

[113] B. I. Miller and A. H. Dayem, Phys. Rev. Lett. **18**, 1000 (1967).

[114] G. Catelani, J. Koch, L. Frunzio, R. J. Schoelkopf, M. H. Devoret, and L. I. Glazman, Phys. Rev. Lett. **106**, 077002 (2011).

[115] D. M. Ginsberg, Phys. Rev. Lett. **8**, 204 (1962).

[116] A. L. Fetter and J. D. Walecka, *Quantum Theory of Many-Particle Systems* (McGraw-Hill).

[117] D. V. Averin and A. N. Korotkov, Sov. Phys. JETP **70**, 937 (1990).

[118] P. Lafarge, P. Joyez, D. Esteve, U. C., and D. M. H., Nature **365**, 422 (1993).

[119] G. Schön and A. Zaikin, Europhys. Lett. **26**, 695 (1994).

[120] J. Wenner, Y. Yin, E. Lucero, R. Barends, Y. Chen, B. Chiaro, J. Kelly, M. Lenander, M. Mariantoni, A. Megrant, C. Neill, P. J. J. O'Malley, D. Sank, A. Vainsencher, H. Wang, T. C. White, A. N. Cleland, and J. M. Martinis, Phys. Rev. Lett. **110**, 150502 (2013).

[121] E. Hashimoto, Y. Ueda, and T. Kino, J. Phys. IV France **5**, C7 (1995).

[122] M. Wulf, Phys. Rev. B **87**, 035312 (2013).

[123] J. Bylander, T. Duty, and P. Delsing, Nature **434**, 361 (2005).

[124] S. P. Giblin, S. J. Wright, J. D. Fletcher, M. Kataoka, M. Pepper, T. J. B. M. Janssen, D. A. Ritchie, C. A. Nicoll, D. Anderson, and G. A. C. Jones, New J. Phys. **12**, 073013 (2010).

[125] S. J. Wright, M. D. Blumenthal, G. Gumbs, A. L. Thorn, M. Pepper, T. J. B. M. Janssen, S. N. Holmes, D. Anderson, G. A. C. Jones, C. A. Nicoll, and D. A. Ritchie, Phys. Rev. B **78**, 233311 (2008).

[126] S. J. Wright, M. D. Blumenthal, M. Pepper, D. Anderson, G. A. C. Jones, C. A. Nicoll, and D. A. Ritchie, Phys. Rev. B **80**, 113303 (2009).